Summer 8-10-2021

A SINGLE CELL PAIR MECHANICAL INTERROGATION PLATFORM TO STUDY CELL-CELL ADHESION MECHANICS

Amir Monemianesfahani
University of Nebraska- Lincoln, amir.monemian@gmail.com

A SINGLE CELL PAIR MECHANICAL INTERROGATION PLATFORM TO STUDY CELL-CELL ADHESION MECHANICS

by

Amir Monemian Esfahani

A DISSERTATION

Presented to the Faculty of

The Graduate College at the University of Nebraska

In Partial Fulfillment of Requirements

For the Degree of Doctor of Philosophy

Major: Engineering

(Biomedical Engineering)

Under the Supervision of Professor Ruiguo Yang

Lincoln, Nebraska

April 2021

A SINGLE CELL PAIR MECHANICAL INTERROGATION PLATFORM TO STUDY CELL-CELL ADHESION MECHANICS

Amir Monemian Esfahani, Ph.D.

University of Nebraska, 2021

Advisor: Ruiguo Yang

Cell-cell adhesion complexes are macromolecular adhesive organelles that integrate cells into tissues. Perturbations of the cell-cell adhesion structure or related mechanotransduction pathways lead to pathological conditions such as skin and heart diseases, arthritis, and cancer. Mechanical stretching has been used to stimulate the mechanotransduction process originating from the cell-cell adhesion and cell-extracellular matrix (ECM) complexes. The current techniques, however, have limitations on their ability to measure the cell-cell adhesion force directly and quantitatively. These methods use a monolayer of cells, which makes it impossible to quantify the forces within a single cell-cell adhesion complex. Other methods using single cells or cell pairs rely on cell-ECM adhesion to find the cell-cell adhesion forces and consequently, they indirectly measure the junctional forces.

In the current study, we designed and developed a single cell-cell adhesion interrogation and stimulation platform based on nanofabricated polymeric structures. The platform employs microstructures fabricated from biocompatible materials using two

photon polymerization (TPP), a process that enables direct 3D structure writing with nanometer precision. The microdevice allows a pair of epithelial cells to form a mature cell junction. The single matured cell junction is stretched with controlled strain until cell-cell junction ruptures while the forces within the cell-junction-cell system are recorded. Using this platform, we have conducted mechanical characterization of a single cell junction with strain-stress analysis. The strain dependency of the junction has been investigated through the stretch test with four different strain rates. The results showed that the junction behaves in a strain-rate dependent manner, where high strain-rates lead to decreased viscosity property, a characteristic for a shear-thinning viscoelastic material. This also confirms our hypothesis that strain-rate plays an important role in the cell mechanical behavior, particularly the cytoskeleton dominant cell mechanics. The maturation of this technology can pave the way for the *in situ* investigation of mechano-chemical signaling pathways mediated by cell-cell junctions and potentially reveal novel disease mechanisms in which defects in cell-cell adhesion play a significant role in the disease pathology.

Acknowledgments

I would like to thank Dr. Yang who trusted in me and for his inexhaustible support and help during my research. His advice was always helpful and pushed me forward. All of the awards I got couldn't be achieved without his support. I would thank the committee members Dr. Tamayol, Dr. Lim, and Dr. Lei for their insightful comments during my Ph.D. candidacy exam. And also, I thank Dr. Lavrik from ORNL who helped us in fabricating the microstructures.

I would thank Dr. Karla Perez who trained me in most of the biology aspects of my research. I would thank my lab mates Bahareh Tajvidi Safa, Jordan Rosenbohm, and Grayson Minnick for their help in the completion of my research.

I would like to express my sincerest gratitude to my wife, Leila, and my children, Baran and Benita, for their patient and supports.

Table of Contents

List of figures

CHAPTER 1

INTRODUCTION TO CELL-CELL ADHESION BIOPHYSICS

Portions of this material have previously appeared in the following publication: Amir Monemian Esfahani, Jordan Rosenbohm, Keerthana Reddy, Xiaowei Jin, Tasneem Bouzid, Brandon Riehl, Eunju Kim, Jung Yul Lim, Ruiguo Yang, Tissue Engineering Part C: Methods, (2019) 25 (11), 631-640. Used with permission.

1.1. Introduction

Tissues in the human body are formed by the physical linkage among individual cells through cell-cell and cell-ECM connections. These physical structures provide mechanical integrity by transmitting physical forces across cytoskeletal networks within individual cells. In the same capacity, they also possess mechanosensory that can feel physical forces and orchestrate a proper biochemical response of different types and timescales. This process, transducing mechanical forces into biochemical signals, has been known as mechanotransduction, a phenomenon that was discovered first in ion channels and later expanded to include mechanochemical processes from many other cells and tissue types (1). Exploration of mechanotransduction has uncovered many molecules with mechanosensing capabilities at the cell-ECM and cell-cell connections, most noteworthy of which are at the focal adhesion in cell-ECM connection sites and cadherin-based cell-cell adhesion sites (2).

Studies in cellular level mechanotransduction use many physical methods to apply a force or strain to cell adhesions, the only physical structures of a cell that can take

mechanical input as a stimulus. Mechanical stretching in a two-dimensional (2D) cell culture model represents the most convenient way of applying this mechanical input (3), among others such as fluid shear. Mechanical stretching normally employs a flexible substrate where cells can grow and form a monolayer. An actuation mechanism induces an in-plane deformation of the flexible substrate and thus causes a strain on the cell monolayer as a whole and, at the molecular level, a strain on the mechanosensing molecules. Different regimens of strains, including static, cyclic, uniaxial, and biaxial, have been proposed to elicit a variety of biochemical responses (4). Through this simple mechanism, researchers have witnessed a host of discoveries that provide an understanding of how cells in different tissues connect and interact with one another in tissue morphogenesis (5), grow and proliferate (6), and, most importantly, probe the microenvironment through mechanosensing to direct their fate (7).

Linker molecules between cadherin molecules and the cytoskeleton at the cell-cell contact, such as α-catenin, generally serve as the mechanosensing elements at cell-cell adhesion sites (8), similarly to focal adhesion kinases (FAKs) at the cell-ECM adhesion sites. They experience straining from external stimuli in the form of a conformational change, which exposes binding sites for molecules in downstream pathways. This series of events subsequently leads to the strengthening of the cell-cell adhesion or dissipation of tissue-level stresses within cytoskeleton elements (9). These responses normally are achieved by forming adhesion bond clusters, or by enhancing existing cell-cell adhesion connections (10). Following mechanotransduction, cells will exhibit various physiological behaviors, and the majority of cell stretching studies are aimed at cellular proliferation and tissue regeneration.

In this chapter, we will provide a focused overview of the cell stretching practices on different cells with an emphasis on the molecular pathways in mechanotransduction which leads to cell proliferation, tissue regeneration, and wound healing. We will review cell-cell adhesive junctions and the biophysical processes in their adaptation to external strain. We will subsequently discuss different modes and regimes of cell stretching, which is followed by an overview of mechanotransduction responses to these different types of stretching. The effect of mechanical stretch on the crosstalk between the cell-cell and cell-ECM adhesion complexes is also discussed, in addition to physiological effects that arise from the responses, such as tissue regeneration and wound healing.

1.2. Cell-cell adhesion

1.2.1. Cell-cell adhesion junctions

There are four types of cellular junctions at the cell-cell contact: tight junctions, gap junctions, adherens junctions (AJs), and desmosomes. Tight junctions seal the paracellular space, limiting the passage of molecules and ions through intercellular spaces of the adjacent cells and preventing the movement of membrane proteins between the upper and lower portions of the cell. Therefore, the apical and basolateral parts of the cell membrane with different functions can be preserved (11). Gap junctions function as pores between adherent cells, allowing small molecules, ions, and electrical current to pass directly between cells (12). This facilitates the passage of potential through a tissue. For example, moving action potential in heart muscles flows across cells, causing the heart to pulse rhythmically (13).

AJs and desmosomes, on the other hand, have a key role in maintaining tissue mechanical integrity. AJs are composed of classical cadherins at the extracellular domain

as adhesion molecules, and armadillo family proteins at the intracellular region as linker molecules (14). At the extracellular domain, E-cadherin molecules from neighboring cells form catch bonds, resisting tension, and maintaining tissue integrity. E-cadherin continues through the cell membrane to the cytoplasmic domain. At this point, E-cadherin is linked to linker molecules, p120- and β-catenin, which are further connected to actin filaments (AFs) through another linker molecule, α-catenin (**Figure 1.1A**). It has been shown that both E-cadherin and α-catenin at AJs serve as mechanosensors in different types of cells in the skin and cardiovascular tissues (15). Desmosomes are cadherin-based adhesive junctions and have a molecular organization similar to AJs (16). Desmosomes are composed of desmosomal cadherin, desmogleins (Dsg), and desmocollins (Dsc), as well as linker proteins from the armadillo family and the plakin family of cytolinkers (17). The cytoplasmic tails of the cadherins connect to the intermediate filament (IF) network through the linker molecules (**Figure 1.1B**). Molecules in the desmosome junction have yet to be revealed as mechanosensors, although some studies have suggested that plakophilin serves as binding scaffolds for RhoA, which potentially regulates cell contractility (18).

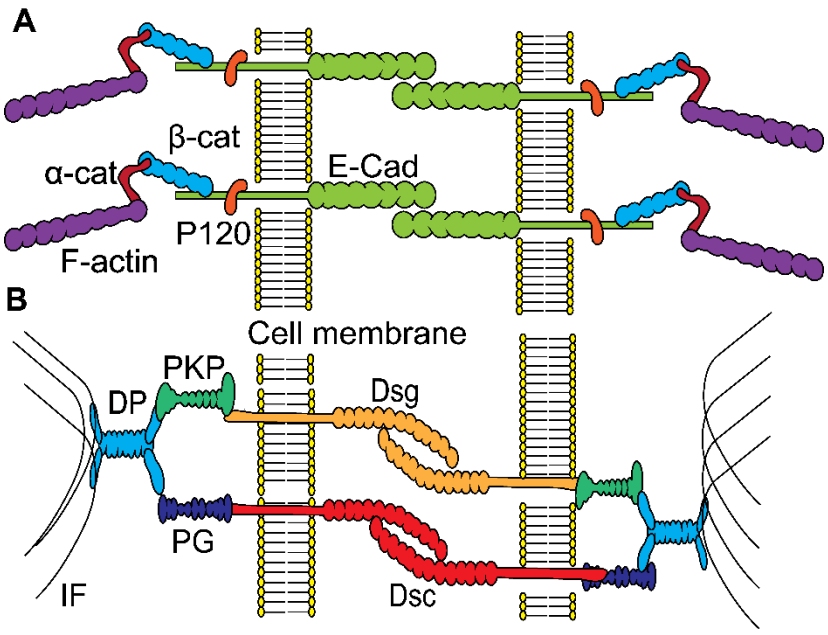

Figure 1.1. The molecular complex of the adherens junction (AJ) and desmosome. A) AJ complex includes a chain of E-Cadherin (E-Cad) at the extracellular domain and α- and β-catenin (α-cat, β-cat) and P120 at the intracellular domain. β-catenin links the cadherin to F-actin through α-catenin. **B)** Desmosome is a combination of three protein families. Desmocollin (Dsc) and desmoglein (Dsg) are the molecules at the extracellular domain. Plakophilin (PKP) and Plakoglobin (PG) are connected to desmoglein and desmocollin, respectively. These two molecules are then connected to intermediate filament through desmoplakin (DP) (19).

1.2.2 Biophysics of cadherin-based AJ and desmosome cell-cell adhesions

Cells adhere to their neighboring cells physically through cellular junctions with cadherin adhesion molecules, transmembrane molecules that have a key role in cell-cell adhesion. They function as a cell-cell adhesion regulator and mechanotransducer during tissue morphogenesis. Cadherin regulates cell-cell adhesion with three mechanisms: 1) varying the interfacial tension between cell surfaces through adhesion tension, 2) providing catch bonds that strengthen when pulled, and 3) initiating mechanosensing to regulate the cytoskeletal network (20). Adhesion tension, like surface tension in liquids, gives rise to

the circular shape of cells; at the cell-cell contact, cadherin causes a reduction in adhesion tension and, as a result, increases the surface contact area (21). In addition to reducing adhesion tension to decrease the interfacial tension between cells, cadherin signaling also helps increase the cell contact area, which is achieved by reorganizing the actomyosin cytoskeleton in the contact area (21).

Studies show that contractile actomyosin exerts pulling forces on the cadherin bonds, which resist the pulling by forming catch bonds to prevent bond rupture (22). Forces are subsequently transmitted through cadherin bonds to the entire cytoskeletal network. The anchor points of cadherin to the cytoskeleton are mediated by α- and β- catenin, and if forces increase, vinculin, and other molecules are recruited to this complex in parallel (23, 24). Researchers determined that the weakest component resides in the cytoplasmic domain rather than the extracellular domain (25-27).

1.2.3. Diseases related to AJs and desmosomes

In normal tissues, cells tightly attach and maintain tissue integrity. In the diseased state, on the other hand, tissues frequently have cells with detachment or abnormal integrity in cell-cell adhesion. In atherosclerosis, when plaque builds up inside blood vessels, the reduction of cell adhesion strength results in the detachment of the plaque, which can lead to a stroke or heart attack (28). In malignant tumors, a significant decrease in cell-cell adhesion is often exhibited (29, 30). Immunostainings of various tumor types with antibodies targeting specific proteins in the AJs have shown a correlation between the changes in the proteins' expressions and pathological conditions (31). In breast cancer, for instance, cadherin expressions are often downregulated and the overall loss of heterozygosity of cadherin is common (31). Loss-of-function mutations in α- and β-catenin

proteins have also been reported in cell lines derived from human epithelial tumors (32). However, the prevalence of these mutations in primary tumors remains to be fully understood.

Desmosomes have the primary role in resisting external strain. They are prominent in the epidermis and heart, tissues often subjected to considerable mechanical stresses in the human body. Mutations in, or autoantibodies directed at, desmosomal proteins lead to compromised cardiac or cutaneous function, and sometimes both. An autoimmune attack on Dsg causes pemphigus and staphylococcus (33). The ablation of the plakoglobin gene results in mouse embryonic lethality owing to the mechanical fragility of the myocardium (34). Desmoplakin mutations can cause an array of diseases in the heart and skin with varying severity (35).

1.3. Mechano-sensation of cell-cell stretching

Mechanical stretching induces an external strain to a layer of cells in the 2D substrate deformation scheme. At the tissue level, cells within the layer reorganize their cytoskeleton structures to dissipate the additional stress. At the cellular level, contractile forces generated from the actin filament network will be balanced at the cell-cell adhesion sites with the external force from the stretch. Mechanosensory processes respond to external stress by strengthening the cellular junctions via the recruitment of adhesion molecules to the cell-cell contact (10).

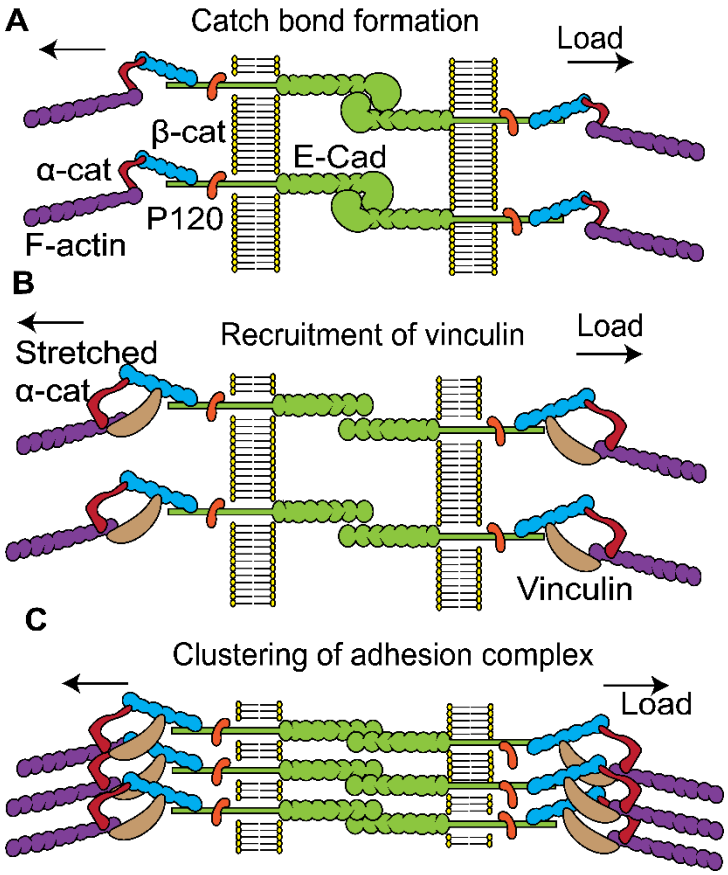

Figure 1.2. Strengthening the adhesion bonds occurs when cells are subjected to an external force. A) Catch bond formation of the cadherin bonds enables them to live longer and strengthen. **B)** Recruitment of vinculin and other molecules to the junction complex parallel to α-catenin can reduce the force on the junction. **C)** Clustering the adhesion bonds at the concentrated stress region can decrease the amount of force on each cell (19).

1.3.1. Strengthening of the junction

Cells can strengthen cell-cell adhesion with different mechanisms. When subjected to an external load, cadherin bonds can switch to long-lived, force-induced bonds with a tighter contact (36), commonly referred to as catch bonds (**Figure 1.2A**) (22, 37, 38). Catch bonds play important roles in cell migration and wound healing as they allow cells to grasp each other strongly when pulled and to release in the absence of external stimuli (39).

Besides, mechanosensors at the AJ and the desmosome initiate a cascade of signaling processes, which results in the strengthening of the linker molecules (40). For instance, α- and β- catenin at the cytoplasmic tail of the junction can recruit vinculin to the complex (41). As a result, the force is divided between the two chains, and the junction can strengthen (**Figure 1.2B**) (42). Further, when mechanosensors at the junction detect stress increase at a specific location, the signaling pathway leads to an increase in the number of bonds (43), and therefore the average force within each bond drops (**Figure 1.2C**) (44-46). In epithelia, E-cadherin is concentrated at regions of greatest tension within the AJ (47), suggesting the presence of several mechanisms that couple the spreading of cadherins to cortical actomyosin. These may include moving cadherins linked to the cytoskeleton towards sites of higher contractile stress (48), clustering of cadherin by F-actin (49) and myosin (50), and regulating cortical actin (51).

1.3.2. Stress dissipation within the cell layer

The molecular complex at the cell-cell junction behaves like a spring. The force stretches the bond and can rupture it at the yield point. To mitigate the effect of applied stress, cells can divide along the direction of the load (52), align their orientation along the principle direction of the load (53), or reorganize the cytoskeleton (54) (**Figure 1.3**). When cells are subjected to force, they can divide and proliferate in the direction of the applied force to alleviate stress within each cell (**Figure 1.3A**).

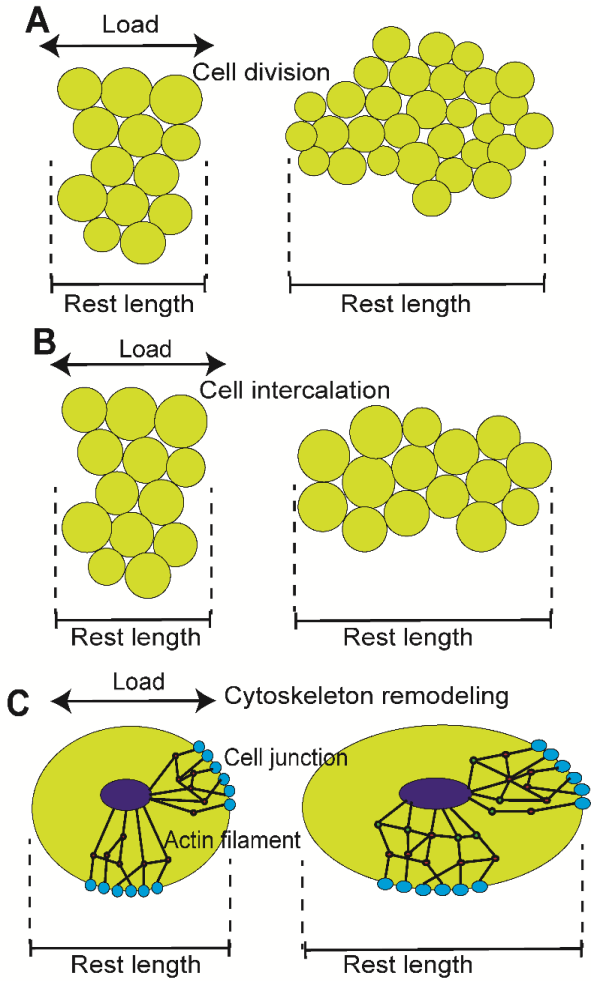

Figure 1.3. Cells can dissipate the force at the cell junction in three ways. A) Oriented division of cells in the direction of the principal stress which adds mass to this direction and increases the rest length. **B)** Reorganization of cells through intercalation. **C)** Molecular remodeling of the cytoskeleton which decreases the stress on the fibers (19).

Another mechanism is through cell intercalation, in which cells can exchange their positions with neighbors so that the resting length increases and the force dissipates (52, 54-56) (**Figure 1.3B**). Rearranging the tissue in this manner leads to additional mass in the direction of the load. Intercalation requires a combination of mechanisms, including adhesive changes at the cell-cell and cell-ECM adhesion sites that allow cells to reposition, cytoskeletal events through which cells exert the forces needed for cell neighbor exchange,

and cell polarity changes to regulate these processes (57). Moreover, the molecular remodeling of the cytoskeleton inside the cell by the upregulation of filaments and cross-linker molecules also dissipates the internal stress (58-62) (**Figure 1.3C**). Consequently, the rest length increases, and the stress on the cytoskeleton decreases (63). Further, the fluid-like behavior of the actin cytoskeleton allows extrinsic stresses to be dissipated by the molecular turnover of cytoskeletal components (64), hence reducing the load on each adhesion complex at the cell-cell junction (65).

1.3.3. Crosstalk between cell-cell and cell-ECM adhesion under mechanical stretch

It has been shown that modulation of cell-cell and cell-ECM adhesions are coordinated during tissue morphogenesis. Increasing the number of cell-ECM adhesion complexes leads to a decrease in the expression of cell-cell adhesion molecules, especially E-cadherin, during mouse lung morphogenesis (66, 67). The adhesion of osteoblasts to collagen in bone formation promotes cell-cell adhesion on the apical surface (68). The formation of cell-ECM adhesions in cancer cells hinders the formation of cell-cell adhesion, as was demonstrated by the negative feedback between the two adhesions when cells were cultured on surfaces coated with both types of adhesion molecules (69). On the other hand, cell-cell adhesion can locally disrupt the formation of cell-ECM adhesion. A study on epithelial cells showed that cadherin formation prevents cell-ECM adhesion formation, which arrests cell migration (70) and results in the disassembly of cell-ECM adhesion in the contact region (71). On the contrary, the disruption of cell-cell adhesion can promote the formation of cell-ECM adhesion complex to facilitate cell migration (72, 73).

Mechanical stretch affects mechanosensors at the cell-cell junctions in association with mechanosensors at the focal adhesion sites. Integrins and cadherins are both connected to actin filaments. Therefore, the same set of molecules are recruited in these junctions when they are subjected to external forces. Interaction of integrin and cadherin causes an upregulation in the expression of RhoA to reorganize the cytoskeleton in response to the mechanical force (74). Actomyosin contractility is one of the major responses to mechanical forces induced at AJs and focal adhesions. In fact, the role of AJs at the cell-cell contact to communicate with cell-ECM adhesions has been well documented (75). These signaling activities include the vinculin signaling facilitated by α-catenin, stress sensing initiated by E-cadherin (76), and the transcriptional activities through β-catenin nucleus translocation (77).

At the tissue level, these integrated networks of actin filaments form a strong connection between neighboring cells and between cells and the ECM. These connections lead to a global transmission of the mechanical force across the tissue when stretched to facilitate collective migration and tissue homeostasis (75). Further, when an external force is applied, since both adhesion types sense the force, a force balance between these junctions is established to maintain tissue integrity. As a result, activating the FAK leads to deactivating VE-cadherins (78). Conversely, weak cell attachment to the substrate results in the aggregation of cells and an increase in cell-cell adhesion (78).

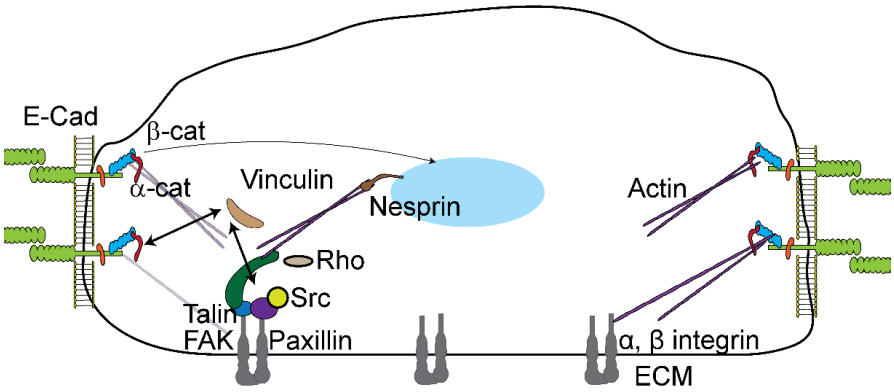

Figure 1.4. Crosstalk of cell-cell adhesion and cell-ECM adhesion mechanotransduction. Cadherin junctions at cell-cell adhesion site have crosstalk with focal adhesion points. Vinculin can be recruited either at AJ in parallel with α-catenin or at the focal adhesion junction in parallel with Paxillin (19).

1.4. Mechanical stretching as a candidate for a therapeutic option

The biophysical processes of strengthening cell-cell adhesion and reducing internal tissue stress lead to a wide variety of physiological phenomena, which allows the scientific community to contemplate whether mechanical stretching can become a suitable candidate for therapeutic options. These efforts resulted in a range of studies correlating mechanical stretch with wound healing and tissue regeneration.

1.4.1. Wound healing

It is widely accepted that mechanical forces are involved in both wound healing and scar formation. Mechanically stretched engineered tissues in bioreactors may have excellent organization, functionality, and strength compared with unstretched counterparts (4). Fibroblasts have been extensively studied in biomechanical wound models, and physical forces are known to influence the expression of ECM genes and inflammatory genes involved in scar formation (79-81). Increased mechanical stresses in the wound

environment induce hypertrophic scarring via stimulation of mechanotransduction pathways, and as a result, cell proliferation, angiogenesis, and epithelization are accelerated (82).

Most wound healing processes occur as a result of the activation of mechanotransduction pathways (83). Rapid embryonic repair of epithelial tissues involves the collective migration of cells around the wound bed. This migratory behavior requires the generation and transmission of mechanical forces for the cells to move and coordinate their movements. Understanding the different aspects of wound healing requires an understanding of the mechanical signals involved in the process and the way these signals are modulated by the mechanical properties of cells, as well as the way the signals are converted into biochemical cues that affect cell behavior (84). Mechanical stimulation modulates integrin, wingless-type (Wnt), protein kinase B, FAK, and several other key molecules downstream of FAK (79). For instance, when mechanical stretch is applied, Src kinase interacts with integrin intracellular domains (85) and FAK (86) at the focal adhesion site, and this further promotes signaling events at the cytoplasmic domain, including talin, paxillin, and vinculin production (87) (**Figure 1.4**). These signaling events promote the assembly of adhesion complexes and facilitate cell migration. For instance, talin is one of the most important proteins that plays a vital role in cell migration (88). In addition, the dynamic interactions of paxillin with α5 integrin and α-actinin has been implicated in the formation of protrusive regions during cell migration (89).

1.4.2. Tissue regeneration

Cyclic loading and inducing mechanical stresses are ways of improving the mechanical properties of engineered tissues and also help in accelerating the regeneration

of cells (90). It is necessary to understand biomechanical stimuli in cells as they may hold the key to prepare tissues with adequate mechanical integrity for implantation purposes. This has been demonstrated in muscle and cardiac tissues. It was shown that mechanical strain affects the maturation of cardiac tissue, cell-cell interaction, and gap junctions (91). Furthermore, in vivo-like forces were applied to human bio-artificial muscles (HBAMs) as they differentiated. By applying a cyclic load, the HBAMs acquired improved tissue elasticity and therefore an increased myofiber diameter when compared to unstretched HBAMs (92). Moreover, cyclic mechanical stretching stimulates the proliferation of cardiomyocytes within engineered early embryonic cardiac tissue and this increase is blocked by p38MAPK inhibitor (93). Further, a bioreactor was used to investigate the influence of mechanical stresses and strains on the properties of mature arteries (94). In the study, cells were subjected to mechanical stress while they were cultured on a substrate, and they adapted to surrounding functional demands while growing to obtain cohesive regenerated tissues (94).

1.4.3. Stem cell differentiation under mechanical stretching

Recently, researchers have focused on applying mechanical stimulation to stem cells in regenerative medicine. Several studies have reported the effects of mechanical stretch on stem cell differentiation toward cardiovascular cell types since they are under continual strain in nature (95). In one study, mechanical loading showed to improve myocardium regeneration and reduced apoptosis during cardiomyocyte differentiation (96). It was also demonstrated that mesenchymal stem cell commitment and differentiation to ligament cells could be stimulated by mechanical stretch loading (97). A comprehensive review of the effect of mechanical loads associated with F-actin on the differentiation of

stem cells revealed that the fate decision of stem cells was mostly governed by mechanical and chemical cues correlated with microfilament proteins and intercellular adhesion molecules (98). For instance, it was documented that cyclic mechanical stretching sped up ECM-induced osteogenic differentiation along with promoting the overall expression (99). Moreover, the RhoA/ROCK, cytoskeletal organization, and FAK were shown to regulate mechanical stretch-induced realignment of hMSCs (100).

Mechanical stretch can further induce the migration of stem cells, such as bone marrow-derived stem cells and MSCs, resulting in their production of expanded skin tissue and skin regeneration (101). For instance, the application of cyclic loading on bone marrow stromal cells promotes cell migration through the FAK-ERK1/2 pathway (102). In addition, MSCs have been transplanted into animal models of skin tissue to investigate the effect of mechanical loading on the migration of these cells to regenerate the skin (103). Further, cyclic mechanical loading can be used to increase cardiomyocyte proliferation in early embryonic cardiac tissue (93).

1.5. Conclusion

Mechanical stimuli have been extensively used to reveal different aspects of cells' behavior. These mechanical forces can then be transduced into biochemical signals to respond to external forces. At the molecular level, there are three different methods that cells use to withstand the force and maintain tissue integrity. These include catch bond formation, other protein recruitments, and cadherin bond clustering. In these situations, the cell tries to reduce the force to each individual bond and avoid being ruptured. At the tissue level, groups of cells respond to the force in terms of oriented cell division, cell intercalation, and cytoskeleton reorganization. In these methods, the resting length

decreases to reduce the applied force to the whole tissue. Mechanical stimuli were also used for wound healing, tissue regeneration, and stem cell differentiation. Recent studies have been showing that these external forces can affect cell migration speed (in wound healing) and proliferation (in tissue regeneration). Further, the application of forces to stem cells makes them differentiate into muscle or cardiomyocyte cells which are subjected to continuous force in nature.

CHAPTER 2

CURRENT TECHNIQUES TO STUDY CELLULAR FORCES AND THEIR MECHANICS

Portions of this material have previously appeared in the following publication: R. Yang, J. A. Broussard, K J. Green, and H D. Espinosa, Extreme Mechanics Letters, Volume 20, 2018, 125-139.

A wide variety of techniques have been used to impose mechanical stimuli on living cells. Most early studies were done on groups of cells, using techniques such as substrate deformation, in which cells are cultured on a deformable substrate, and flow-induced shear, in which fluid flowing over a culture of cells imposes shear stress on the cells. Most of the cell mechanical properties are anisotropic due to the inherent heterogeneity of cells, so studying cells in groups only gives average responses instead of uncovering the complex response individual cells have. Technological advances allowed for the study of cells on an individual level and many techniques were developed to do this. Some of these methods include atomic force microscopy (AFM), optical traps/optical tweezers (OT), magnetic beads, and micropipette aspiration. These techniques allow for the manipulation of single cells and can, therefore, be used to uncover the anisotropic properties of cells. More advanced methods of cell probing are commonly called micro-electromechanical systems (MEMS). These devices generally include piezo-electric controlled actuators to impose stresses on the cells, either by directly attaching to the cell or moving a structure that the cell is attached to. Some examples of MEMS devices include uniaxial and biaxial pullers, micropillars, and cantilever beams. These devices offer the highest force and displacement

resolutions. In this chapter, we will introduce the techniques used to study cell behavior under external loads.

2.1. Monolayer based stretching

Interrogating cells in a monolayer is the most convenient way to study cell-cell adhesion and the effect of mechanotransduction in healthy and diseased conditions. In these methods, cells are seeded and grown on a flexible substrate which is then stretched through the application of a load. These loads are transduced to biochemical signals through different pathways depending on the nature of the load (104-106). Different cell types behave in different ways to the same stimulation, which has yet to be fully studied (107). Investigators have cultured various cell types on these flexible substrates, such as bone cells (108), lung cells (109), and neurons (110), to study cell responses to the stretching force, including cell proliferation, migration, differentiation, cytoskeleton rearrangement, and other mechanotransduction responses.

Two common load types have been used to investigate cell-cell adhesion using flexible substrates. The simplest is static loading, in which a fixed strain is applied to the substrate and held. Viscoelastic properties of cells such as relaxation time can be investigated with this load type. Conversely, dynamic loading is used to subject the substrate to a time-varying strain. The effect of strain amplitude and frequency on tissue behavior of melanocytes has been explored with this load shape (111). In-plane uniaxial and biaxial stretching are commonly used as methods to apply a uniformly distributed force to cells. To apply the load, the substrate is attached to a mechanism that stretches the substrate upon actuation. Bone cells and embryonic osteoblasts were investigated using this stretching method (112, 113) (**Figure 2.1A** and **2.1B**). Uniaxial and biaxial stretching

methods are mainly used to study the effect of load on bone tissue (107, 114, 115). A similar in-plane technique uses vacuum pressure to apply strain to the substrate of cultured HEK293 cells (**Figure 2.1C**) and offers a uniform, equiaxial strain on cells (116). Four-point bending (117, 118) is an out-of-plane technique for applying strain to the substrate (**Figure 2.1D**). This method offers a low strain and uniform longitudinal and lateral stresses on cells. The curved template method is another out-of-plane stretching technique in which the substrate is pressed on a curved template which deforms the substrate out-of-plane (**Figure 2.1E**). By controlling the shape of the curved template, a uniform strain can be achieved (119).

The main advantage of the 2D substrate deformation methods compared to other techniques such as fluid flow and 3D cell culture is that the amount of force can be precisely adjusted. Determining the force in fluid flow-induced shear requires rigorous calculations and the force in 3D culture is directed in three dimensions, making the exact amount of force on cells difficult to be calculated. The stiffness of the substrate is a parameter that plays an important role in the resolution of the applied load. Substrate stiffness is controlled by changing the substrate's thickness or chemical composition. By altering the substrate stiffness, researchers can get different force resolutions, allowing for even more control of the force. However, obtaining a fine resolution through control of substrate stiffness is still an issue. Another advantage of 2D substrate deformation methods is the variety of load conditions that can be applied to the substrate. When compared to fluidic flow and 3D stretching, more options for load applications are available for substrate deformation.

Aside from these advantages, the 2D stretching method has some limitations. Since the load is applied to a cell monolayer, it is almost impossible to directly and quantitatively

measure the adhesion forces at either the cell-cell or cell-ECM adhesions. Albeit, there is some statistical analysis that can be done on these data, but the exact amount of the adhesion force is not obtainable. Furthermore, stretching cell monolayers cannot reveal the underlying mechanotransduction crosstalk between cell-cell and cell-ECM adhesions (117). Studies have shown the interplay between integrin and cadherin-based adhesions when cells are stimulated by external load or fluid shear (75, 120, 121). Since monolayer stretching applies to stress and strain to both adhesion complexes at the cell-cell and cell-ECM contacts, it is difficult to decouple the mechanotransduction pathways originating from the two interfaces. A detailed discussion of this crosstalk from recent cell stretching studies is presented in the following section.

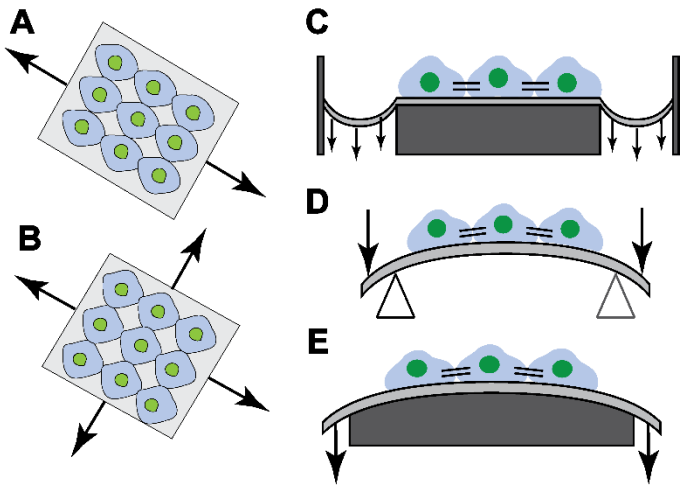

Figure 2.1. **Mechanical stretching of a monolayer of cells. A)** Uniaxial stretching. **B)** Biaxial stretching. **C)** Equiaxial stretching with vacuum suction. **D)** Four points bending substrate flection; **E)** Stretching with a curved template (122).

Fluid flow can be used to impose shear stress onto a group of cells. To do this, cells are cultured on the surface of a fluid flow channel. As fluid flows over the culture, shear stress is imposed on the cells from the boundary layer between the cells and the fluid (**Figure 2.2A**). This method has been used in a variety of studies, including investigating

the influence of fluid shear on the proliferation of bovine aortic endothelial cells (123) and investigating rolling adhesion of white blood cells in shear flow (124). The primary advantage of this method is the natural environment this study takes place in. Cells commonly interact with fluid flow in vivo, so this setup allows for a very natural testing environment. Two kinds of fluid flow systems are commonly used. The first is a parallel plate system, in which fluid flow is driven through a small rectangular chamber using a pressure differential. A variety of parallel plate systems have been developed (125-131), and technological advances allowed for smaller microscopic parallel plate systems (132-134). In these studies, the dimensions of the channel can be varied to control the flow characteristics and thus shear stress and are kept small to ensure a low Reynolds number and thus laminar flow. In one study, the width of the fluid flow channel was varied between 0.25 and 1 mm, which changed the shear stress imposed on a culture of fibroblasts (135).

The other system is a cone and plate system, in which a cone is rotated along its axis above the surface of a circular plate (**Figure 2.2B**). Many studies have used this technique (136-140). The tangential speed of the cone increases with increased distance from the axis of rotation, but the distance between the cone and flat plate also increases, resulting in uniform shear stress distributions along with the plate and the cone surface. By varying the angle of the cone and the speed of rotation, many shear stresses can be achieved.

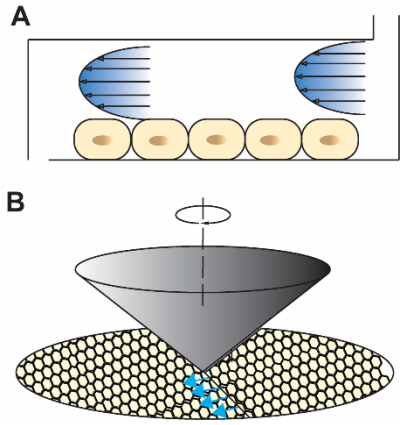

Figure 2.2. Fluid shear applied to the cell layer to study cell mechanics. A) Fluid flows in a chip with a layer of cells. Different flow rates result in different shear stress on cells. **B)** The rotating cone can make different shear stress at different angular velocities and distances from the axis of rotation (117).

2.2. Cell-substrate and cell-cell interaction measurement

Traction Force Microscopy (TFM) is the first mature technique to measure cell-generated forces (141). In 2D TFM (**Figure 2.3A**), by measuring the substrate deformation induced by cellular contractile forces, a stress map can be generated to quantify these interaction forces per unit area. To this end, gel substrates embedded with fluorescence beads are used to grow adherent cells. The dislocations of beads due to gel deformation are calculated by comparing beads images captured when cells are attached and when cells are trypsinized off the substrate. Several image processing methods (even ImageJ plugins (142)) can compute the so-called displacement field by the traction force from the attached cells (143). Common substrates used for TFM include polyacrylamide or silicon-based gels. They are selected due to their linear elasticity and optical transparency, and normally their elastic moduli can be tuned over several orders of magnitudes (144). Knowing the elastic moduli of the substrates, the displacement field can be converted to the stress field or traction force by integrating the stress field over an area. To consider the normal

component of the traction force in addition to the in-plane one, 3D TFM has been developed in recent years (145, 146). There are layers of complexity and potential sources of inaccuracy in computing the 3D displacement field involving ECM degradation and nonlinearity of local deformation in 3D ECM among others (147). But some study does show traction force differences between 2D and 3D matrix conditions (148).

In the study of cell-cell adhesion, TFM has so far produced the most reliable results by indirectly quantifying cell-cell tugging forces through their force balance with cell-ECM traction forces. These findings show direct evidence of crosstalk between cell-cell and cell-ECM adhesions (149-151). On the one hand, integrin-mediated adhesions regulate the tension and composition of cell-cell junction (21, 143, 152-154); on the other hand, cadherin-based cell-cell adhesions in epithelial cells modulate cell-ECM traction forces (149). In the latter case, by controlling calcium level and genetically switching off cadherin (E-, and P-cad), a study has shown remarkably different traction force patterns for keratinocytes: cooperative traction force with maximum stress at the peripheral of cell colonies, and independent and significant traction force evenly distributed throughout the colonies (149). Similar cooperative activities of cell-cell and cell-ECM adhesion were also observed in heart muscle cells (71). Further, the force balance, as well as molecular tension in E-cad, are modulated by spatial distributions of adhesion sites (155).

Microposts are purely mechanical devices that are used to measure adhesion and traction forces cells exert on the surface they adhere to. In this experimental setup (**Figure 2.3B**), an array of microposts are fabricated. The geometry and composition of the microposts determine their stiffness. When a cell is placed on the bed of microposts, the posts bend as the cell exerts a force on them. Using optical microscopy, the deflection

distance and direction can be measured, and knowing the stiffness of the post, these measurements can be converted into the force the cell is exerting on the micropost. The primary advantage of this technique is the large number of independent force measurements that can be taken at once, which when combined, gives a vector map of traction forces the cell exerts. However, there is no way to control the strain the microposts induce on the cell, so this is a passive technique. Also, forces can only be measured on the plane between the cell and the end of the posts, and forces normal to this cannot be quantified. One implementation of this technique used microposts with varying stiffness by changing the geometry of individual microposts. This allows for control of the sensitivity of force measurements on certain regions of the cell (156). Another study embedded some of the microposts with magnetic cobalt nanowire. This allowed for control of the microposts with the magnetic wire using an externally controlled magnetic field, allowing for active control of forces on regions of the cell adhered to these microposts. This setup was used to study the relationship between external mechanical forces and internal biologically induced forces by applying a force to the magnetic microposts and observing focal adhesion and traction forces on non-magnetic posts near the magnetic posts (157).

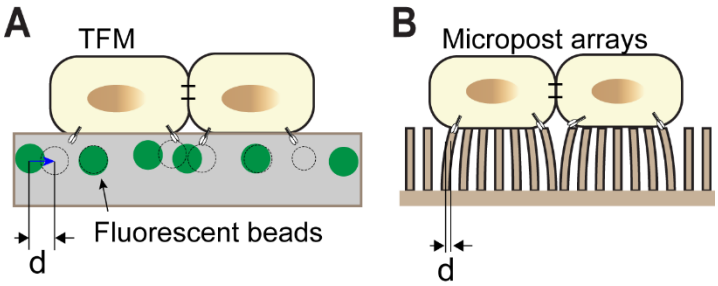

Figure 2.3. Cell-ECM adhesion forces measurement. A) TFM **B)** Micropost (117).

2.3. Individual cells or cell pairs forces measurements

2.3.1. Micropipette Aspiration

Micropipette Aspiration is a simple technique in which a single cell is aspirated into the tip of a micropipette (**Figure 2.4Ai**). The micropipette is positioned on the cell, and a vacuum inside the micropipette slowly aspirates the cell into the micropipette. By making the micropipette inside diameter smaller than the cell, compressive strains are imposed on the cell as it enters the micropipette (158). This technique imposes large strains on cells, and as a result, is incompatible with some cell types (159). Also, there are high-stress concentrations along the edge of the pipette, and there is friction between the pipette surface and the cell, which impacts results. This method has commonly been used to study the viscoelastic behavior of cells, as cells slowly aspirate into the micropipette (160, 161). Mathematical models have been used to convert resulting strains into stresses in erythrocytes (162, 163) and chondrocytes (164), but they have limited accuracy due to the many assumptions the models use.

In addition to aspirating cells, micropipettes have been used to manipulate individual cells for other kinds of tests. In one experiment, two cells were brought into contact with each other using two micropipettes (**Figure 2.4Aii**). The micropipettes use a slight vacuum that can securely hold the cell on the micropipette without significant aspiration to not introduce additional strains. After some time, the cells adhere to each other. Then, the pressure in one of the micropipettes is increased until the cell bond breaks. By knowing the pressure needed to break the cell bond, the mean adhesion force can be found (165, 166). Two other studies were done which used two micropipettes to stretch a single cell. In one, a slight vacuum was used to hold the cell on the tips of the micropipettes, and one

micropipette tip was actuated to strain the cell. One micropipette was attached to a cantilever beam with a strain gauge, which could be used to quantify the input force to the cell (167). In the other, the tips of two micropipettes were coated with a urethane resin adhesive, which allowed a cell to adhere to them. One of the micropipettes was rigid and stationary, and the other micropipette was flexible and actuated with a piezoelectric actuator. The deflection of the flexible micropipette was recorded and used to determine the force applied to the cell (168).

2.3.2. Optical Traps and Stretchers

Optical traps use the conservation of momentum of diffracting photons to impart small forces on dielectric objects (169). This method has been used to study many molecules (170), including the kinetics of RNA unfolding (171). When used to study cells, dielectric microbeads are adhered to the cell and act as handles for the optical trap. The adhesion strength limits the maximum force an optical trap can exert on a cell (172, 173). Once the microbeads adhere to the cell, a laser is directed through one of the microbeads, refracting the laser. The refraction changes the momentum of the photons, and thus changes the momentum of the microbead, inducing a force. The microbead is attracted to the focal point of the laser, and therefore the force can be controlled by altering how the laser is focused on the microbead (174). For this to work, the refractive index of the bead must be larger than the refractive index of the medium the cell is in. Generally, this technique is used to apply static loadings to cells, but can also be used for cyclic loadings, using an acousto-optic modulator (175).

One study using optical traps looked at the impact malaria had on the mechanical properties of diseased red blood cells. In this study, healthy red blood cells (173) and

infected blood cells (176, 177) were stretched using an optical trap. The diseased cells were tested in various stages of the infection, and it was found that the shear modulus steadily increased throughout the infection, increasing by about an order of magnitude by the final stage of the infection. A variation to optical traps, known as optical stretchers, uses divergent lasers that interact directly with the cell without the need for microbead handles (**Figure 2.4B**). In this technique, the laser spot size must be larger than the cell for stability. Two lasers are directed on diametrically opposite sides of the cell, and as photons interact with the cell, they impose a force on the cell, causing it to stretch. In addition to the requirement of the refractive index of the cell being larger than the refractive index of the surrounding medium, the cell's refractive index must be homogeneous. This technique has an advantage over optical traps in that higher laser powers can be used. This is because the laser is unfocused, so the intensity of the laser is much less than the focused laser used for optical traps (178-180). The two main advantages of these techniques are their high force resolution and lack of physical contact with the cell. Using these techniques, sub pN forces can be achieved, and cells can be studied in more natural environments because they do not need to be physically attached to an instrument. However, the maximum achievable force is limited to a couple of hundred pN, and high laser power may impart radiation damage onto the cell.

2.3.3. Magnetic Beads

Magnetic beads can be used as handles to apply forces to a cell. First, the beads are coated with a biochemical that allows them to bind to specific cell surface receptors (111). Once they are attached, they can be manipulated through the control of an external magnetic field (**Figure 2.4C**). This method was developed in 1950 (181) and has been used

in a variety of studies, including applying cyclic loadings to cells (182-184). Two main advantages of this technique are the ability to apply torque to cells and the ability to easily apply cyclic loadings through control of the magnetic field. However, due to unfavorable scaling of magnetic forces with size, applying large forces with this technique requires large beads relative to cell size (185).

2.3.4. Atomic Force Microscopy (AFM)

AFM is a technique that was originally developed to map the surface of nanoscale structures. A silicon-based probe with a sharp tip is mounted on a cantilever beam and is brought into contact with a surface. As it contacts the surface, the cantilever beam bends, and by tracking its deflection by recording the angle at which a laser beam is deflected off the back of the cantilever beam, the height of the surface can be measured (**Figure 2.4Di**). This technique has been adapted to study cell mechanics by relating the amount the cantilever beam deflects to the force the probe is placing on a cell by knowing the stiffness of the cantilever beam. AFM has been used to study global elastic properties (186, 187) and global viscoelasticity properties (188), as well as smaller-scale properties of cell nuclei (189). This technique offers sub pN force resolution and sub-nm displacement resolution but has a limited maximum force and displacement. In addition to compressive forces, AFM can also be used to apply tensile forces to a cell. One way this can be done is by culturing cells directly on the AFM tip. This allows for easy manipulation of cells and has been used to study cell-cell and cell-substrate interactions (190). In addition, the AFM tip can be functionalized to bind to cell surface receptors in a technique widely accepted as single-molecule force spectroscopy (SMFS) (**Figure 2.4Dii**). Once functionalized, the probe can be retracted to apply tensile forces and unwind or break molecular bonds (191).

SMFS has been used extensively to study binding affinities for a host of molecules, including the unbinding of DNA protein pairs (192, 193).

In the study of cell-cell adhesion, AFM has been used in the context of single-cell force spectroscopy (SCFS) (194, 195) (**Figure 2.4Diii**). This technique is similar in principle with micropipette-based cell-cell adhesion studies using DPA, where two cells are brought into contact and pulled apart to quantify their interaction. Compared with the DPA method, SCFS offers a higher resolution (pN compared to nN for DPA) and less native strain to the cells before contact. In SCFS adhesion measurements, a living cell is first attached to a tip-less AFM cantilever, normally utilizing matrix protein coating, and the cell was brought into contact with another cell on the substrate by lowering the cantilever using a z-piezo stage. During the retraction phase, the interactions can be measured by recording the cantilever deflection. The sensitivity in force measurement and the fine position control by the z-piezo stage enables the quantifications of subtle cell-cell interactions during the initial phase of adhesion. These forces are often retraction rate-dependent and dwelling time-dependent (194, 196). A prolonged dwelling time often leads to the study of cooperative binding. SCFS studies have led to the conclusion that levels of E-Cad determine the adhesion strength between different types of progenitor cells in zebrafish development (197). Destructive methods are also used to probe cellular responses including the use of laser pulses (198-200) or AFM probes (201, 202) to dissect cytoskeleton components.

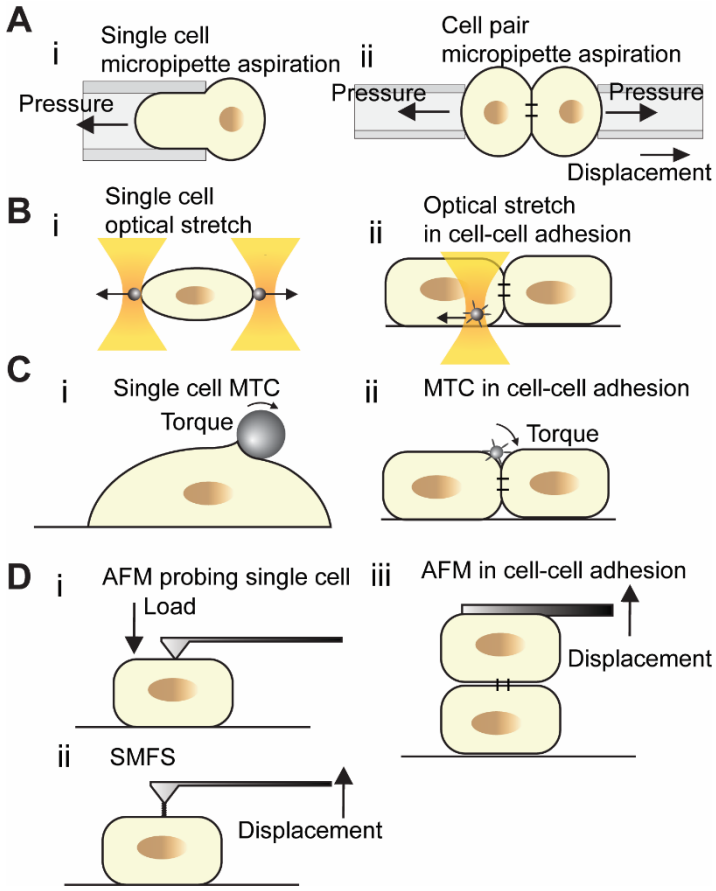

Figure 2.4. Individual cell and cell pair adhesion force measurement. A) Micropipette aspiration (i). Single cell (ii). Cell pair **B)** Optical stretch (i). Single cell (ii). Call pair **C)** Magnetic beads (i). Single cell (ii). Cell pair **D)** AFM based measurements (i). and (ii). Single cell (iii). Cell pair (117).

2.4. MEMS devices

2.4.1. Cantilever beam deflection

A wide array of MEMS devices that use cantilever beam deflection have been developed. In general, these devices use a cantilever beam to deform a cell. As the cell deforms, the force also bends the cantilever beam, and by knowing the stiffness of the beam, the force can be found by measuring the deflection of the beam. Many designs utilizing this technique have been made, with an array of force ranges and sensing capabilities. A 1-dimensional and a 2-dimensional cantilever beam MEMS device were

developed for probing cells (203). The 1-D sensor is only capable of measuring force in the x-direction. A probe used to stimulate the cell is attached to two sets of parallel beams. The beams confine the movement of the probe to a single dimension and also act as a spring with a known spring constant (**Figure 2.5Ai**). This structure is actuated with a piezoelectric actuator, and as the probe interacts with the cell, the beams are deformed. This deformation is recorded and converted into a force using the known spring constant. The 2-D sensor only has one beam attached to the probe, instead of two sets of parallel beams (**Figure 2.5Aii**). This allows the probe to move in both the x and y-direction. Another set of cantilever beam MEMS devices were developed that featured much higher resolutions than previous designs (204). These devices featured many cantilever beams connected on their ends. By doing so, each beam only deflects slightly, which limits the nonlinear effects of beam deflection calculations, increasing resolution without limiting force range (**Figure 2.5Aiii**). One configuration simply connects one beam to the end of the next beam, with the probe at the end. This configuration allows for measurements in two dimensions with high resolutions, but it has a lower measurement range. The second configuration connects pairs of parallel beams end to end. This only allows for force measurement in one direction, but it has a much larger measurement range. By controlling the number of beams used, the force range and resolution can be controlled.

2.4.2. Moveable platforms

In a moveable platform MEMS device, a cell adheres to a platform that is split into two or more parts. The cell adheres to the platform while the parts are together, and then the parts of the platform are separated using a piezoelectric actuator and mechanical linkages. As the parts of the platform come apart, the cell is stretched, and the degree to

which the cell is strained can be controlled by the separation distance between the parts of the platform. Two variations of this technique have been implemented, a uniaxial puller and a biaxial puller.

2.4.2.1. Uniaxial puller

A uniaxial puller consists of two platforms, one of which is fixed while the other is moveable (**Figure 2.5B**). The moveable platform is attached to a piezoelectric actuator, which can control the displacement of the platform. In one study, a uniaxial puller was used to study the mechanical properties of hydrated collagen fibrils (205). An electrostatic comb drive actuator was used to actuate one of the platforms, while the other was held rigidly in place. The main advantages of using an electrostatic comb-drive actuator include low power consumption using moderate driving voltages, and high speed and accuracy. Also, the use of an electrostatic comb drive actuator allowed for the cyclic loading of the cell.

2.4.2.2. Biaxial puller

A biaxial puller was developed that used an electrostatic comb-drive actuator and a cleverly designed kinematic linkage that allowed for controlled actuation of four segments of a platform at the same time (206). In this setup, one part of the stage was fixed, while the other three were connected to a kinematic linkage that was connected to the electrostatic actuator (**Figure 2.5C**). When the actuator moves, the linkage causes the three mobile portions of the platform to move in mutually orthogonal directions from each other, and if small displacements are assumed, they move away from each other at the same speed. This results in a uniform biaxial strain on the cell.

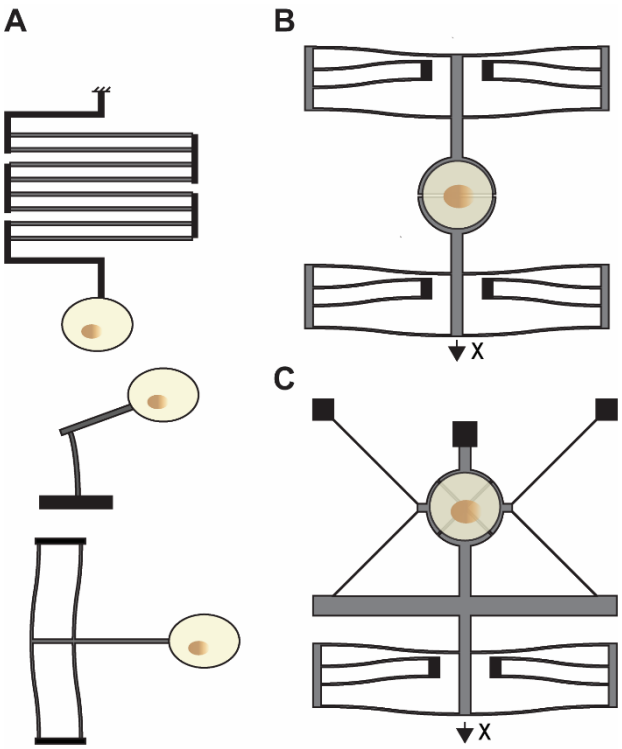

Figure 2.5. MEMS-based cellular force measurements. A) Beams **B)** Uniaxial puller **C)** Biaxial puller (117).

2.4.3. 3D Nanofabrication

Two-photon polymerization (TPP) has enabled the fabrication of devices at the nanoscale and more importantly using biocompatible fabrication materials (207). A new class of micro-scaffold with nanometer-scale features has been developed for cell attachment and growth (208-211), for force measurement from cell adhesion-induced interactions (212), and stimulation of focal adhesions (213).

2.5. Conclusion

Characterizing the intricacy of the biophysical and biochemical response requires techniques that can quantify cell-generated forces and apply precise forces to cell-cell adhesion complexes. Several widely-used techniques in the quantitative assessment of cell-

generated forces include traction force microscopy (TFM) (214) and elastomer-based micropillar arrays (215). These methods provided great insights into the actin-based cell-extracellular matrix (ECM) adhesion networks. In addition, micro-scaffolds fabricated by 3D printing have been used to measure cell forces in a 3D microenvironment (209, 216). Nevertheless, for the study of cell-cell adhesion, one has to quantify indirectly, relying on the force-balance between cell-cell and cell-ECM adhesions (215). More importantly, the quantification methods are restricted to static observations and fail to apply desirable mechanical stimuli. Cyclic stretching is able to provide mechanical stimuli to a monolayer of cells and induce a variety of cellular responses (217). However, the lack of stress measurement during loading has positioned the method as a stimulator rather than a quantitative mechanical analyzer. Besides, it is impossible to apply defined loads onto each individual cell junction using a monolayer cell stretcher, thus making it a qualitative stimulator (53). To date, the mechanics of the cellular junctions remains poorly understood with regard to the role of various components of the junction play in maintaining the integrity of the cell adhesion during mechanical stress. Specifically, the majority of the studies are carried out on isolated cells where mature intercellular junctions are yet to form, and the focus can only be placed on the separation of the cadherin bonds. And yet, when mechanical stretch testing is conducted on a monolayer of cells, the lack of stress measurement during loading and the inability to apply defined loads onto each individual cell junction renders the study qualitative.

CHAPTER 3

SCAμTT, A SINGLE CELL ADHESION INTERFACE MECHANICAL CHARACTERIZATION PLATFORM

Portions of this material have previously appeared in the following publication: Amir Monemian Esfahani, Jordan Rosenbohm, Bahareh Tajvidi Safa, Nickolay V Lavrik, Grayson Minnick, Quan Zhou, Fang Kong, Xiaowei Jin, Eunju Kim, Ying Liu, Yongfeng Lu, Jung Yul Lim, James K Wahl, Ming Dao, Changjin Huang, Ruiguo Yang, Proceedings of the National Academy of Sciences, (2021) 118 (7). Used with permission.

3.1. Proposed design for single cell-cell adhesion interrogation

A novel micro-device has been designed and fabricated to interrogate the mechanical behavior of the cell-cell junction. This device consists of two moveable islands with known spring constants. A single epithelial cell (keratinocyte cell line) is picked up using the Eppendorf single cell isolation system and placed on each island. When a mature junction forms between the cell pair across the gap between the islands, it is strained for the evaluation of mechanical strength until it fails. To do this, the displacement of Island 2 is directly controlled using an AFM system, which can displace the island between 0 to 50 μm, while Island 1 is displaced under the tensile force through the cell-cell junction. The device is integrated on top of an inverted microscope which is used to monitor the displacement of the islands, from which the deformation of the beams is determined. Island 1, therefore, functions as a force sensor that can be used to measure nano-Newton range forces applied to the cell junction by relating its displacement to the spring constant of the beam that supports it. The stretch test process is captured by a screen recorder and divided

into individual frames which are analyzed by a digital image correlation method to track the islands' displacements (**Figure 3.1**).

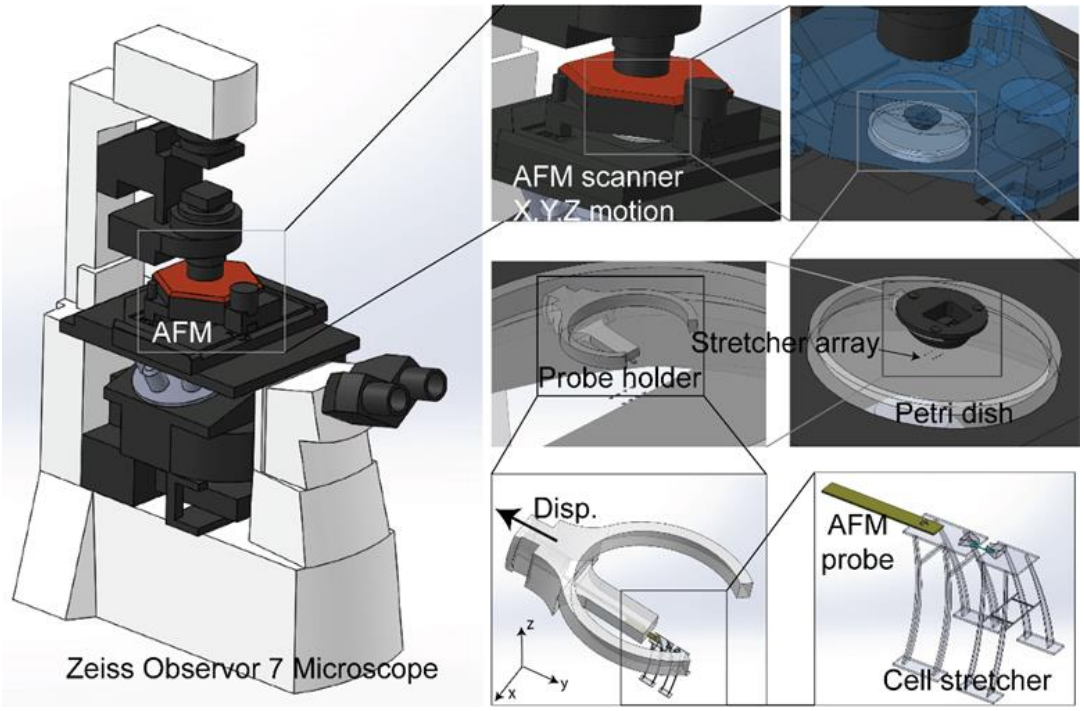

Figure 3.1. Detailed illustration of the entire SCAμTT platform. We used the AFM setup as a tool to stretch the platform. Specifically, we utilized its precise X, Y, and Z positioning capabilities to capture the pillar on the device within a hole drilled into the tip of a cantilever probe tip, and could subsequently define a path for the tip to follow at a specified speed to apply strain at a controlled strain rate to the platform. We did not use any other functions such as spectroscopy. To help illustrate how the AFM setup is integrated into our platform, we drew a Solidworks model. An AFM probe with a hole drilled in the tip with a focused ion beam (FIB) is mounted on the scanner head, and the AFM system is then placed on the stage of an inverted microscope above the sample. The probe tip is then moved using controls on the stage and the AFM software until the pillar is captured within the hole on the probe tip. From here, a line for the probe tip to follow is defined within the AFM software along with the scanning speed to displace the tip in the Y-direction and apply the strain at a controlled strain rate.

The stiffness of the supporting beams was designed to be as close to the stiffness of the cell-cell junction (0.01 N/m – 0.5 N/m) (218) as possible to acquire the best balance

between force-sensing resolution and applied strain to the cell-cell junction, with the ability to measure a force in the range of 0 – 50 nN at the junction (219, 220). The resolution of the device is determined by the minimum force which can be detected by Island 1 which is related to its stiffness. If the beams are too stiff, the movement of the island will not be seen under the microscope. A compliant beam will allow the island to move more, allowing the displacement to be more accurately quantified. On the other hand, their stiffness must be high enough to prevent it from collapsing during the fabrication process. Several generations of the sensing beam structure have been designed, fabricated, and tested, and their stiffness was calculated using COMSOL Multiphysics simulation software. The first generation was a group of parallel horizontal beams. A design with 5 sets of beams was proposed as the first design. After the simulation, the calculated stiffness was $K = 1\times10^5$ N/m, which, compared to biological samples, was too large to measure the stress in the cell-cell junction (**Figure 3.2A**). By reducing the number of beams, decreasing the beam width from 5 μm to 2.5 μm, and increasing the beam length from 80 μm to 150 μm, we were able to decrease the stiffness to 4.6 N/m (**Figure 3.2B**). However, this was still too large to measure stress. Since we reached the maximum printing dimensions of the 3D printer device without stitching, we could not increase the length and due to the structure stability, we could not decrease the width of the beams. A serpentine beam was then proposed to further decrease the stiffness with these geometric constraints in mind. This design further reduced the stiffness of the structure (K = 1.05 N/m) but was still too stiff (**Figure 3.2C**). The force-displacement curves of these designs are compared in **Figure 3.2D**. It is worth mentioning that these stiffness data are all calculated in air.

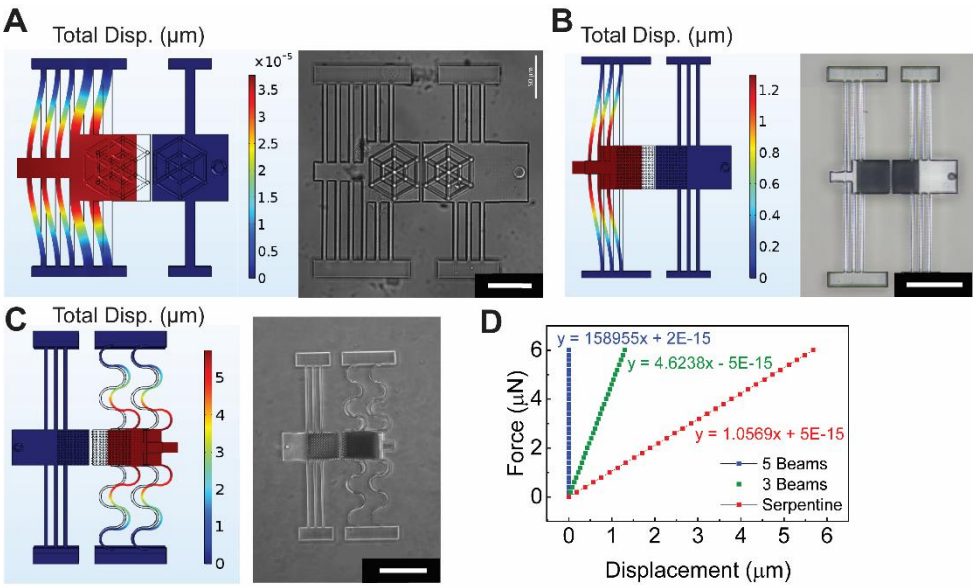

Figure 3.2. Design, simulation, and fabrication of the first generation of the single cell pair stretcher (horizontal). **A)** Horizontal beam design with 5 parallel beams attached to the sensing island and 1 pair of beams attached to the actuating island. This design had the highest stiffness (K = 1e5 N/m) and was not able to measure the junction stress. Scale bar = 50 μm. **B)** Horizontal beam design with 3 pairs of beams attached to the sensing and actuating islands, with the width decreased from 5 μm to 2.5 μm and length increased from 80 μm to 150 μm. The new stiffness was 4.6 N/m which is not low enough to measure the junction stress. Scale bar = 100 μm. **C)** Horizontal beam design in which the sensing island beams are changed from the straight to the serpentine design which is less stiff. This design had 1.05 N/m stiffness which is still too stiff to measure the junction stress. Scale bar = 100 μm. **D)** The force versus displacement of different designs has been plotted to compare and find their stiffness.

All the horizontal beam designs have a stiffness higher than our desired values (0.01 N/m – 0.5 N/m). So, a vertical beam design was proposed (**Figure 3.3A**). The vertical beam with a height of 280 μm was able to give us a stiffness close to our goal (0.22 N/m). However, the beams being exactly underneath the islands creates high-intensity background noise during fluorescent imaging, blocking the signal from cells. Therefore, we designed a double cantilever beam design by moving the beams' bases to the sides of

the islands (single Λ-shape). Theoretically, this change resulted in increasing the stiffness, so the design was modified by decreasing the beam thickness from 5 μm to 2.5 μm and increasing its height to 300 μm. With COMSOL simulation, its stiffness is lower than the other beam geometry designs (0.08 N/m); however, it collapsed during fabrication (not shown in the figure). Adding another set of Λ-shape beams (double Λ-shape) to increase stability still resulted in the collapse of the structures (**Figure 3.3B**). Finally, a set of trusses were added horizontally to connect the vertical beams and enhance stability (stabilized A-shape), while decreasing the beam thickness to 2 μm, resulting in stable structures with stiffness of 0.11 N/m. (**Figure 3.3C, D**). It is worth mentioning that these stiffness data are all calculated in air. Compared with horizontal beams, vertical beams offer greater control of their length which allows for easy adaptation to this desired stiffness and offers better structural stability during the TPP fabrication process. A set of vertical "A-shaped" beams were designed and fabricated considering different constraints in beam stiffness, beam stability, fabrication limitations, and imaging requirements.

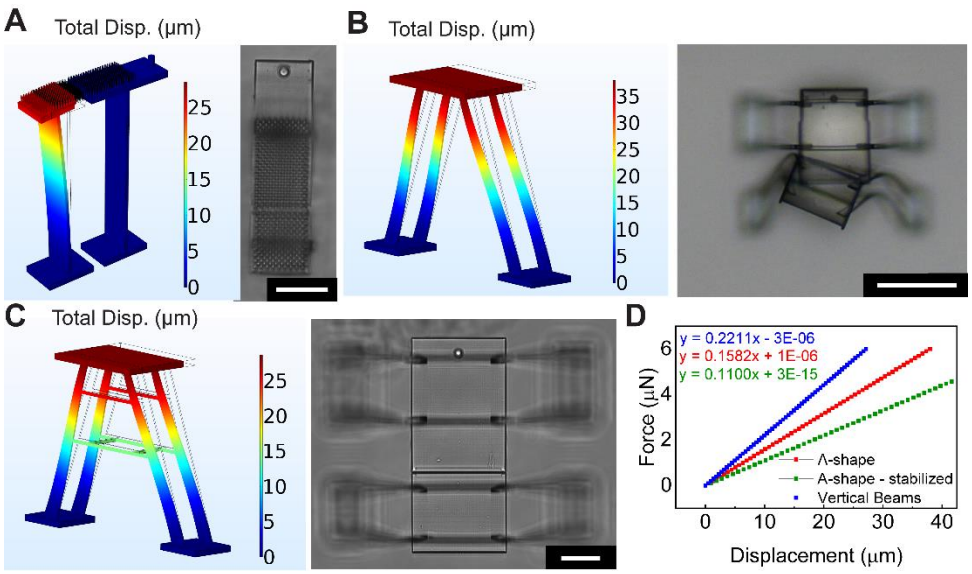

Figure 3.3. Design, simulation, and fabrication of the second generation of the single cell pair stretcher (vertical). A) The vertical beam design was less stiff compared to the horizontal beam design and more stable during fabrication. The new design had a height of 280 μm and its stiffness was 0.22 N/m, which allows us to measure the junction stiffness. Scale bar = 50 μm. **B)** The double Λ-shape design solved the background noise issue, but it was not stable during fabrication and collapsed. Scale bar = 100 μm. **C)** The double A-shape design with the supporting truss was the final design because of its stiffness and stability. Scale bar = 50 μm. **D)** The force versus displacement of the vertical beam designs has been plotted to compare and find their stiffness.

3.2. Device fabrication and calibration

3D models of the micromechanical structures for biological cell mechanical interrogation were compiled in COMSOL using the built-in CAD. Various preliminary designs, including planar structures, were implemented using TPP stereolithography and tested in terms of their processability and susceptibility to damage by capillary forces. The compiled models were evaluated using the Solid Mechanics module (linear elastic materials approximation). The finite element analysis (FEA) in COMSOL allowed us to

estimate effective spring constants of the flexible beams supporting a pair of microscale plates for cell attachment. As a result of the FEA analysis and experimental tests applied to multiple iteratively refined designs, we identified the most promising design that could be fabricated with high yield and fidelity. The rationale behind this design is as follows. First, compared to doubly clamped (bridge) structures, singly clamped (cantilever) beams provide a more linear elastic response with significantly lower sensitivity to intrinsic stresses. Second, the parallelogram arrangement of the twin-beam leaf springs improves the leveling of the cell-bearing platforms and the overall mechanical stability of the devices. Furthermore, vertical beams separated by larger distances from the substrate are preferable over horizontal beams closer to the substrate due to the better ability of the former to withstand capillary forces after fabrication. Finally, the thinnest beams that could be reliably fabricated with high accuracy and yield were approximately 2 mm thick. This minimum thickness, combined with the targeted stiffness, dictated the width and the length of the beams in the implemented structures.

To fabricate several batches of structures, microscale 3D printing based on TPP was used (221). CAD files in STL format exported from COMSOL 4.2 software were imported into the Describe software (Nanoscribe, GmbH) to compile job files for the Photonic Professional (GT) tool (Nanoscribe, GmbH). The slicing and hatching distances were selected to be 0.4 μm and 0.3 μm, respectively. The vendor-supplied liquid photoresist, IP-S, and a 25x immersion microscope objective were used to print structures in the galvo-scanning mode using the so-called deep-in laser lithography (DiLL) optical arrangement.

Glass coverslips with diameters ranging from 11 to 25 mm and thicknesses of approximately 160 μm were used as substrates in the present study. Prior to 3D printing, the glass substrates were coated with indium tin oxide (ITO) to achieve optical reflectivity of the IP-S/substrate interface sufficient for autofocusing. The ITO layer had a thickness of approximately 50 nm and was deposited using direct current sputtering of an ITO target in an Ar plasma. In our initial tests, we found that mechanical 3D structures printed directly on ITO-coated glass had insufficient adhesion and would detach from the substrate after prolonged soaking or incubation in aqueous solutions. To address this commonly encountered issue of insufficient adhesion between smooth substrates and 3D structures fabricated using TPP, we used an in-house developed protocol in which an additional layer of porous silicon oxide (PSO) was deposited on top of ITO-coated coverslips. PSO with a thickness of approximately 2 μm and a high density of nanopores was found to act as an excellent anchoring layer, eliminating detachment of the 3D printed structures from the substrate during soaking and subsequent experiments in aqueous solutions.

To prevent the deposited cells from migration, a bowtie structure was designed and fabricated with one trapezoid on each island (**Figure 3.4C**). This makes it more likely for cells to form a junction between the islands within the gap. Studies showed that an average cell-cell junction length is between 8 to 12 μm (219). Also, a single cell needs a space of 40 μm by 30 μm when attached to a surface (220). The area of the trapezoid and the length of its opening edge were optimized to preserve the physiological conditions with an area large enough to sustain cell growth and an opening edge of 12 μm to facilitate junction formation at the interface between the two islands (220). The gap between the two movable islands, particularly between the bowtie opening where the junction forms, should be kept

to a minimum to facilitate junction formation, but a gap distance of less than 2 μm leads to unwanted polymerization of the resin that tethers the two islands during the fabrication process. We increased the gap of the non-bowtie region to 6 μm to reduce the risk of attachment of the islands (**Figure 3.4D**).

To measure the stiffness of the "A-shaped" beam structure, a tipless cantilever probe with a thermally tuned stiffness was used to apply force on an isolated sensing structure in Phosphate-buffered saline (PBS) solution. Based on the displacement of the probe and the force measurement from the AFM probe, the deflection and subsequently the stiffness of the microstructure were determined. The modulus of elasticity of TPP fabricated materials varies with laser power, print speed, and post-process curing methods. In this study, fabrication parameters remained as consistent as possible. A Nanosurf AFM was used to conduct force spectroscopy experiments on horizontally printed sensing microstructures to attain an average stiffness value. A tipless cantilever probe (TL-NCL by Nanosensors) with a known and thermally tuned stiffness, k_p, was used to press on horizontally fabricated sensing microstructures with beam thickness, $t = 2\ \mu m$ (**Figure 3.4E**). AFM uses the deflection of the probe, Δx_p, and its known stiffness, k_p, to measure the applied force, P_{AFM}. The sensing microstructure is also subjected to the same force as it produces the reaction to cause the probe deflection:

$$P_{AFM} = \Delta x_p \cdot k_p = \Delta x_{sens} \cdot k_{sens} \tag{3-1}$$

Here, Δx_{sens} and k_{sens} are the deflection and stiffness of the sensing microstructure, respectively. The AFM outputs the data as force, P_{AFM}, versus displacement, d (**Figure 3.4F**). As shown in **Figure 3.4E**, the probe is deflected upwards and the structure

downwards, therefore the deflection of the microstructure can be calculated by the following:

$$\Delta x_{sens} = d - \Delta x_p \tag{3-2}$$

To evaluate the data to find the stiffness, the probe deflection is first found from equation (3-1). Next, the structure deflection is solved using equation (3-2). Lastly, by substituting the values into the sensing part of the equation (3-1), the stiffness can be found:

$$k_{sens} = \frac{P_{AFM}}{\Delta x_{sens}} = \frac{1}{d/P_{AFM} - 1/k_p} \tag{3-3}$$

To analyze the AFM data, a MATLAB script was used to smooth and average the AFM force versus deflection curves and to calculate the sensing structure stiffness by fitting the averaged line of the data, where the slope was equal to the stiffness.

For each measurement, the automated detection of the AFM was used to initiate contact between the probe and the structure. Once contact was established, a constant probe displacement rate was initiated to apply force on the structure until the force set point was achieved. The probe was then retracted until it was no longer in contact with the structure before beginning the process again. This produced the force-displacement curve from which the stiffness of the beam can be extracted (**Figure 3.4F**). The calculated beam stiffness was found to be 0.049 ± 0.005 N/m under liquid conditions (**Figure 3.4G**), which is within the desired range. This stiffness value remains valid for a sensing beam deflection of ~6 μm (i.e., a maximum force of 294 nN), displaying a large linear range. It is worth mentioning that the TPP printing parameters, including laser power and scan speed, can have a significant influence on the measured stiffness. Considering the resolution of DIC

at a few tens of nanometers, this sensing beam stiffness can resolve the forces of a few cadherin bonds (~40 pN for each cadherin bond (222)).

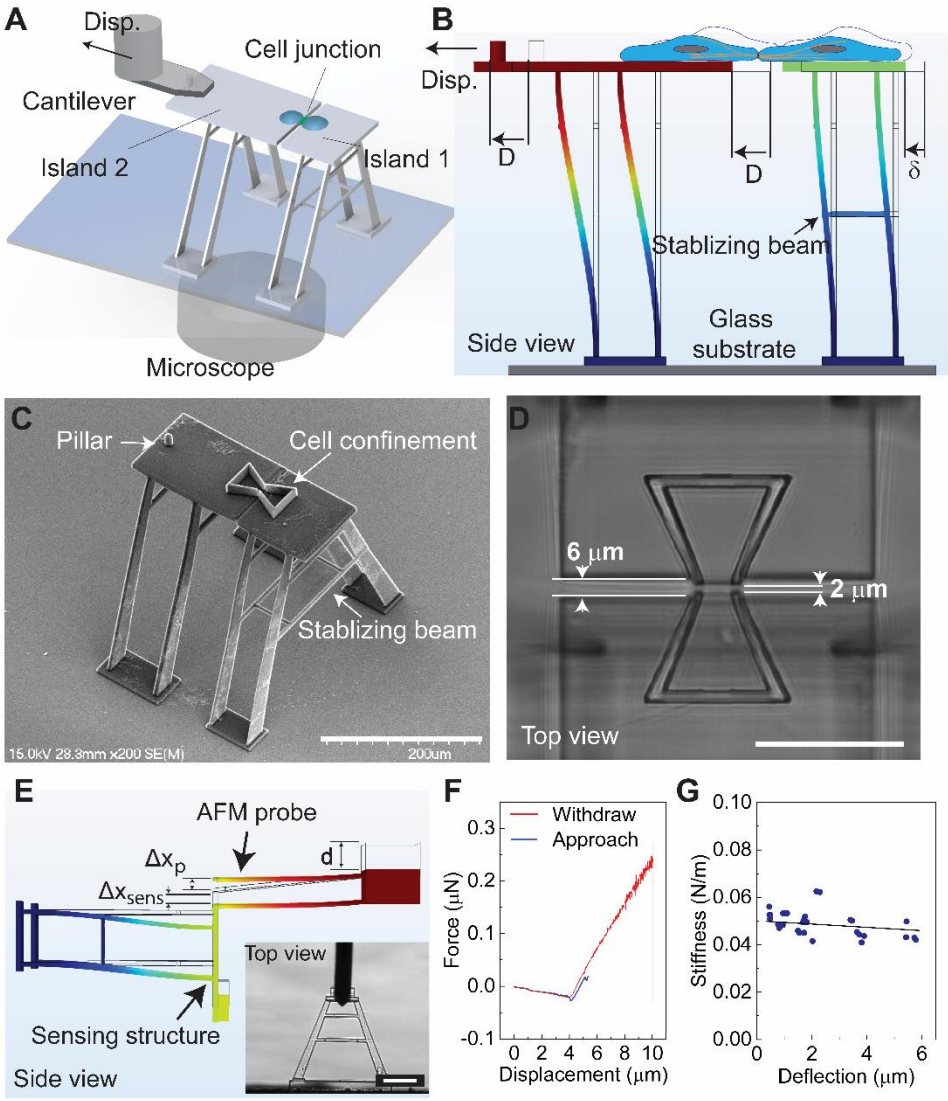

Figure 3.4. A single cell-cell adhesion interface mechanical characterization platform. A) A single cell pair with junctional contacts is formed on Islands 1 and 2. To apply mechanical strain to the cell-cell junction, an AFM-based manipulation system displaces Island 2. **B)** The deflection of Island 1 (δ) under the applied displacement (D) is recorded to determine the force-displacement relationship. **C)** SEM image of the structures fabricated on top of a glass substrate. The bowtie structures confine the cells on each island. **D)** The two islands were spaced 6 μm apart to prevent attachment of the islands to each other, with a 2 μm gap

between the cell-confining bowties to allow formation of the cell-cell junction. **E)** To measure the stiffness, an AFM probe applies force to the structure until a displacement set point is achieved, and then retracts. The AFM records the applied force, P_{AFM}, and vertical displacement d. The vertical structure displacement, Δx_{sens}, and deflection of the AFM probe, Δx_p, are determined from the AFM output. The inset image shows the probe applying force onto the structure. **F)** A representative force-displacement curve obtained at a maximum applied force of 294 nN is shown. **G)** Sensing structure stiffness, k_{sens} vs. structure deflection, Δx_{sens} is plotted (n=30). Scale bars: 200 μm in **C**; 50 μm in **D**; 100 μm in **E** (223).

To examine the elasticity of the structure, two experiments were performed with a controlled displacement and release. The first one was a 25 μm displacement and sudden release of the structure and the second one was a 50 μm displacement and sudden release. Since lower strain rates have more impact on the viscoelastic properties of the material, we used 100 nm/s (0.005 s^{-1}) for both experiments. **Figure 3.5** shows the displacement-time plots for the experiments. For the 25 μm displacement, 0.135 seconds after release, and for the 50 μm displacement, after 4.72 seconds, both return to the original position within the resolving power of the DIC, thus ruling out major plastic deformation. Further, the rapid release and return of the 25 μm test demonstrate that the viscoelastic effect can be negligible with this displacement, slightly less so with the 50 μm test. In our cell stretch experiments, the displacement of the sensing island is within 5 μm, in which elastic deformation dominates according to this experiment.

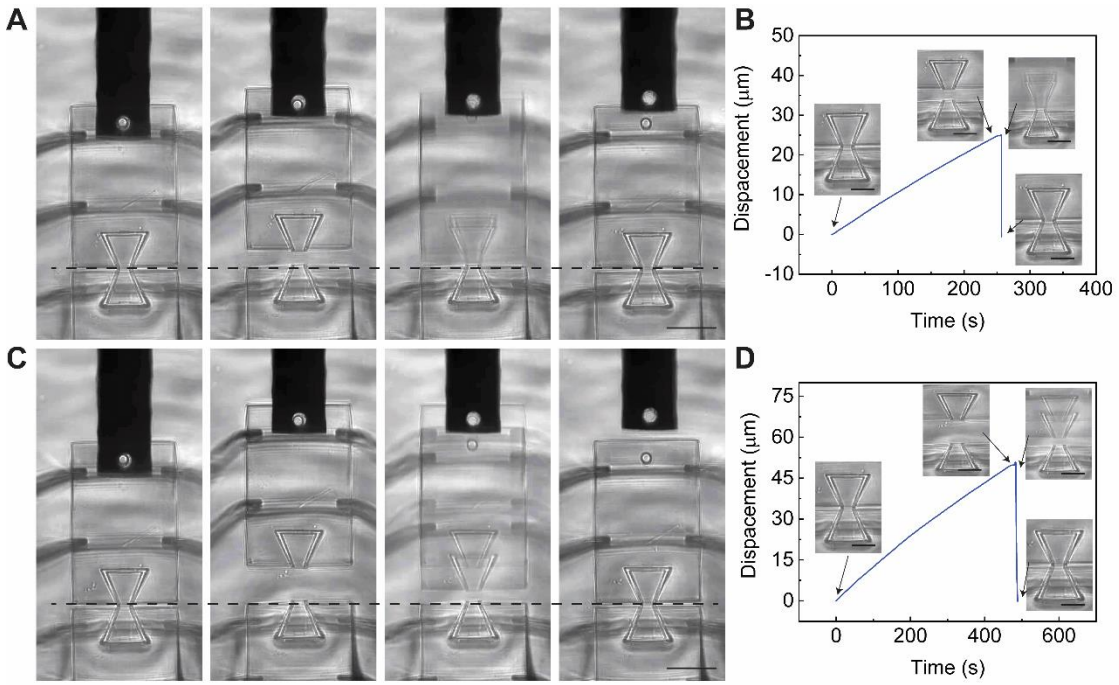

Figure 3.5. Elastic deformation of the structure. A) 25 µm displacement and sudden release. Scale bar: 50 µm. **B)** Displacement versus time for the 25 µm displacement. Scale bar: 25 µm. **C)** 50 µm displacement and sudden release. Scale bar: 50 µm. **D)** Displacement versus time for the 50 µm displacement. Scale bar: 25 µm.

3.3. Cell deposition procedure

Cell manipulation was performed using the well-known Eppendorf cell isolation system. This setup consists of a microcapillary (Piezo Drill Tip ICSI, Eppendorf) integrated with a pressure controller (CellTram® 4r Air/Oil, Eppendorf) and a 3D manipulator (TransferMan® 4r, Eppendorf), allowing for precise 3D cell manipulation. The inner diameter of the microcapillary was chosen based on the cell diameter (approximately 15 µm). To aspirate and hold a cell on the needle tip, the inner diameter should be less than the cell diameter. Based on available needle sizes from Eppendorf, we selected Piezo Drill Tip ICSI with a 6 µm inner diameter. The needle is connected to the capillary and through a tube to the pressure controller. The tube is filled with mineral oil, and a small

displacement of the pressure controller cylinder creates positive or negative pressure at the needle tip. The needle approaches the cell using the 3D manipulator (**Figure 3.6A**). When it touches the cell membrane, a negative pressure is applied to aspirate the cell (**Figure 3.6B**). While the cell is held at the needle tip, it is positioned above Island 2, and a positive pressure is applied to detach the cell from the needle and place it on the surface (**Figure 3.6C**). The same procedures are performed to place the second cell on Island 1 (**Figure 3.6D, E, and F**). This process is performed inside a temperature-controlled chamber.

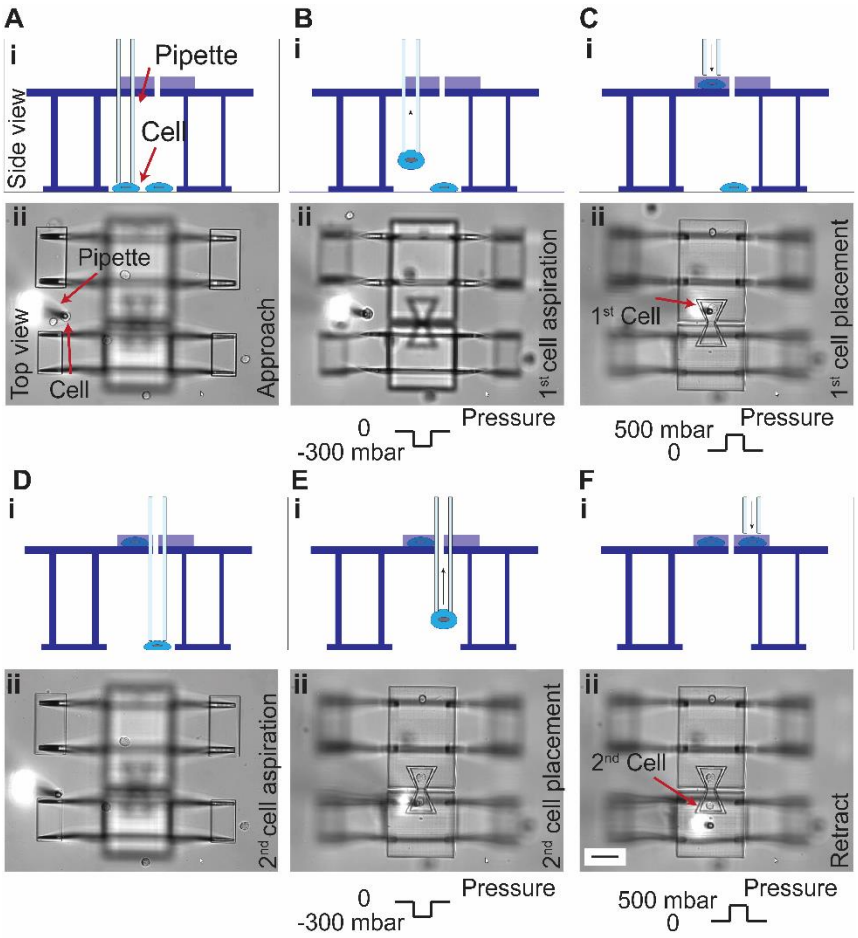

Figure 3.6. Cell deposition procedure. A) One cell is targeted and the microcapillary approaches the cell using the 3D manipulator. **B)** A negative pressure is applied with the pressure controller to aspirate and hold the cell. **C)** The manipulator moves the cell to the structure and a positive pressure is applied to

deposit the cell on one of the islands. **D-F)** The same steps are performed to aspirate and deposit the second cell on the other island.

3.4. Cell-cell adhesion junction formation

A431 E-cadherin GFP tagged cells were cultured in a growth medium composed of Dulbecco's modified Eagle's medium (DMEM) and supplemented with 10% fetal bovine serum (Chemie Brunschwig AG) and 1% penicillin-streptomycin (Invitrogen). The experimental medium consisted of CO2-independent growth medium (Invitrogen) supplemented with 2 mM L-glutamine (Sigma-Aldrich Chemie GmbH), 10% fetal bovine serum, and 1% penicillin-streptomycin. All solutions were filtered through 0.22 μm pore-size filters before use. Shortly before each experiment, PBS was replaced with 2 ml of the experimental medium. All experiments were performed in a temperature-controlled enclosed chamber at 37 °C.

As shown in **Figure 3.7A**, a pair of E-cadherin GFP-tagged A431 cells were successfully deposited and placed inside the bowtie structure. 16 hours after cell deposition and incubation, cells were stained for actin and DAPI and imaged. The cells successfully grew within the bowtie structures on top of each island and formed a mature junction by expressing E-cadherin GFP (**Figure 3.7B**).

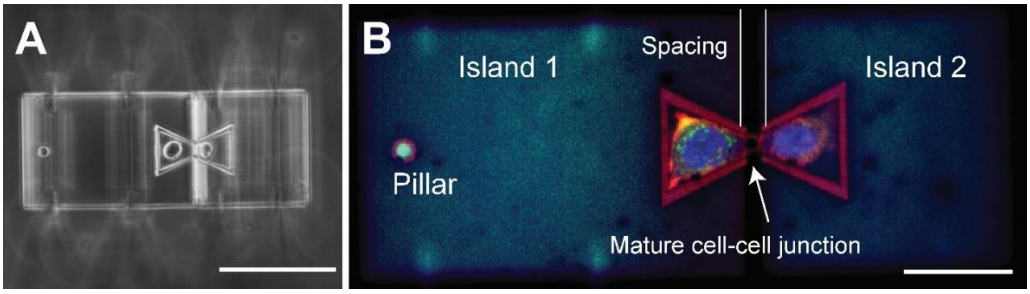

Figure 3.7. Cell-cell adhesion junction formation and cell growth on the scaffolds. A) Cell deposition onto the fabricated structure shows the ability to place cells in the opposing bowtie confinement

scaffolds. Scale bar: 100 µm. **B)** A pair of cells form a mature cell-cell junction 16 hours after cell deposition and incubation as shown by the expression of E-cadherin GFP. The cell junction spans across the gap between the two movable islands. Cells were stained for actin and DAPI. Scale bar: 50 µm (223).

The A431 cells were E-cadherin GFP tagged and so the junctions can be seen without adding staining solutions. Alexa Fluor™ 657 Phalloidin (Invitrogen) was used to stain the actin filaments and the nuclei were stained with DAPI (Invitrogen). The substrate with the cells was placed in a glass-bottom petri dish. The cells were washed twice with PBS, pH 7.4, and fixed using 4% formaldehyde solution in PBS for 15 minutes at room temperature, and then washed two times with PBS. Subsequently, they permeabilized with a solution of 0.1% Triton X-100 in PBS for 5 minutes, and then washed twice with PBS. To enhance the quality of the actin fluorescent intensity, 4 drops of Image-iT™ FX Signal Enhancer (Thermofisher) were added and incubated at room temperature with a humid environment for 30 minutes. After removing the solution and washing with PBS, the Phalloidin staining solution with a ratio of 1:100 in PBS was placed on the substrate for 30 minutes at room temperature and then washed with PBS. Then, the DAPI (Invitrogen) solution with a ratio of 1:1000 with PBS was placed on the substrate and incubated for 10 minutes at room temperature. The solution was removed, and the substrate was washed with PBS. Finally, 3 mL of pure water was added to the petri dish for imaging. A Nikon A1-NiE upright confocal system (60X water immersion objective) driven by NIS-Elements Confocal image acquisition and analysis program (Nikon software) was used for immunofluorescent imaging of cells on the structures. All image reconstruction and channel alignment were performed within the Nikon software.

Since the polymer used for fabricating the device was autofluorescent, we needed to quench it. The substrate with the structures was placed inside of a glass-bottom petri dish,

washed with 70% ethanol, and immediately soaked with PBS for 10 minutes until all the ethanol dissolved. To enhance the quality of the images, the whole substrate was submerged in 0.3% Sudan Black B in 70% ethanol for one hour to eliminate the autofluorescence of the polymer. To dissolve excessive Sudan Black, the substrate was submerged in 70% ethanol for 1 hour and then soaked with PBS for 10 minutes. The substrate was then coated with fibronectin to enhance the adhesion and growth of the cells on the structures. Fibronectin with a concentration of 50 µg/ml was added on the substrate and left in the incubator for 2 hours. Finally, the fibronectin solution was removed, and the substrate was washed with PBS two times.

The immunofluorescence images of these cells on the structure prove the biocompatibility of the polymer. E-cadherin expression shows the cell-cell junction formation and actin shows that cells spread and grow on the structure (**Figure 3.8**). As we expected, the junction is formed within the gap, thus proving the ability to deposit and grow cells on the novel device and for a junction to form between the cells.

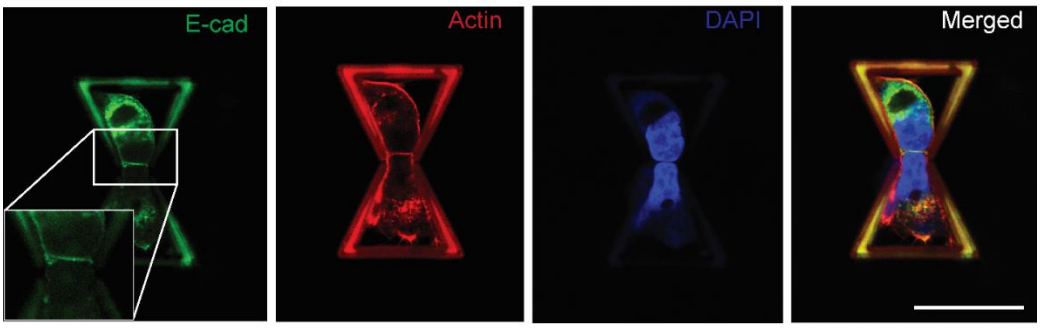

Figure 3.8. Formation of a mature cell-cell adhesion junction. To demonstrate the biocompatibility of the structures, A431 cells with GFP-tagged E-cadherin were deposited onto the structures. Actin filaments were stained 16 hours after deposition. E-cadherin imaging shows the formation of a mature cell-cell junction and actin filaments imaging shows that cells maintain a spread shape on the structure. Scale bar: 50 µm (223).

To demonstrate focal adhesion formation and cell attachment to the substrate, zyxin was stained. Zyxin is a focal adhesion protein that is expressed when a cell forms a cell-ECM junction. Staining zyxin together with actin filaments confirms that cells successfully form focal adhesions on the structure (**Figure 3.9**). Zyxin staining was performed to visualize the focal adhesion points between cells and the structure. After fixing the cells, the anti-Zyxin antibody produced in rabbit (Sigma) with a ratio of 1:250 with PBS was added to the sample and refrigerated for 24 hours. Next, the solution was removed, and the sample was washed with PBS. Then, PBS was replaced by Goat anti-Rabbit IgG (H+L), Superclonal™ Recombinant Secondary Antibody, Alexa Fluor 647 (Thermofisher) and incubated for 1 hour at 37 °C. Finally, the sample was washed with PBS and the actin and DAPI protocol were performed.

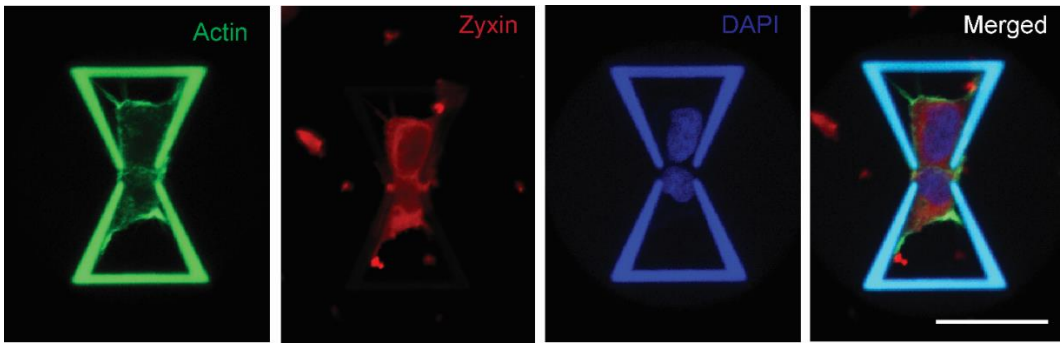

Figure 3.9. Cell-ECM junction formation. Zyxin and actin filaments were stained to visualize the formation of cell-ECM adhesion (focal adhesion), confirming that cells successfully attach to and grow on the structures. Scale bar: 50 μm (223).

To find the best time for the stretch test after cell deposition, a time-lapsed study was performed. Cells were stained and imaged after 4 hours, 8 hours, 16 hours, and 24 hours (**Figure 3.10**). The results revealed that cells do not form a mature junction before 8 hours after cell deposition, and after 16 hours, they form a mature junction and are ready for the stretch test. However, after 24 hours, they start proliferating, and as a result, there will be

more than two cells. Therefore, all experiments were conducted around 16 hours after cell deposition and incubation. A mature cell-cell junction, defined as the homeostatic state when E-Cad levels and distribution are stabilized at the cell-cell contact (224), is formed between the cell pair as indicated by the expression of GFP-tagged E-Cad, which bridges the gap between the two islands and mechanically couples them. The immunofluorescence images of these cells on the structure suggest that the polymer material used in the TPP fabrication is biocompatible and allows for proper cell attachment and growth. Staining zyxin, a widely used mature focal adhesion protein marker (225), together with F-actin confirms that cells successfully form focal adhesions on the structure.

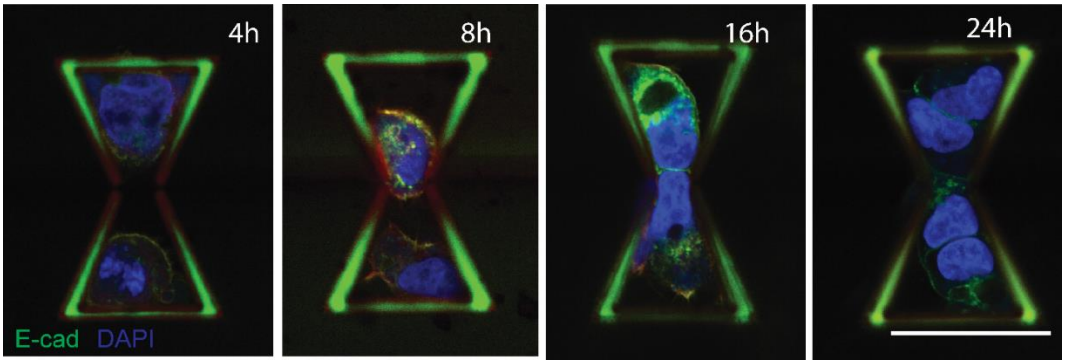

Figure 3.10. Time-lapse images of the cell-cell adhesion formation. A time-lapse study of cell growth after deposition was performed to find the optimized time for the stretch test. Images show that cells do not form a junction before 8 hours, form a mature junction after 16 hours, and begin proliferating after 24 hours. To stretch a single cell pair, all experiments were done around 16 hours after cell deposition. Scale bar: 50 μm (223).

CHAPTER 4

DISPLACEMENT-CONTROLLED MECHANICAL CHARACTERIZATION OF THE CELL-CELL JUNCTION

4.1. Cell-cell junction stretch test

For the stretch test, Sudan Black was not used because it blocks the light, which makes cell deposition and cell tracking impossible to perform. The substrate with the structures was placed inside of a glass-bottom petri dish, washed with 70% ethanol, and immediately soaked with PBS for 10 minutes until all the ethanol dissolved. The substrate was then coated with fibronectin (50 μg/ml) to enhance the adhesion and growth of the cells on the structures. The fibronectin solution was placed on the substrate and left in the incubator for 2 hours. The solution was removed, and the substrate was washed with PBS.

To push and pull the structure, an AFM setup was used. For this purpose, the AFM probe was drilled using FIB etching to make a circular hole with a diameter of 15 μm so that it could capture the pillar (10 μm diameter) on the structure. When the junction is mature, the stretch test is performed. The substrate with the structures and cells was placed under the AFM setup integrated with an inverted microscope. The AFM probe approaches the pillar on Island 2 and captures it within the through-hole. From here, the AFM can apply displacement (from 0 to 100 μm with 10 nm resolution) with different displacement rates (from 50 nm/s to 20 μm/s) to Island 2 to stretch the cell-cell junction. After several experiments, we found that a 50 μm displacement with a 5 % s^{-1} strain rate was enough to break the junction. Hence, we applied this displacement for all experiments and tried different displacement (strain) rates to study the rate dependency of the junction's behavior.

Strain rate is defined by the displacement rate divided by the initial length. The diameter of each cell is approximately 20 μm. We assumed a pair of cells that have a junction in between are attached fully to the substrate and when the force is applied, half of each cell is detached and contributes to the stretch test. Therefore, the initial length will be 20 μm.

Each stretch test was recorded and analyzed with a customized DIC-based program to calculate each island's movement. The displacement of each island was obtained by averaging the displacement of markers in the ROI in each frame. Similarly to previous studies on epithelial monolayers (53), the strain was calculated by dividing the difference of the two islands' displacements by the initial length: $\varepsilon = (D - \delta)/L_0$, where D is the Island 2 (actuation) displacement, δ is the Island 1 (sensing) displacement, and L_0 is the initial length. This initial length was defined as the nucleus-to-nucleus distance of the cell pair which was measured to be 19.18 ± 0.50 μm (**Figure 4.1**). We had assumed that deformation occurred in the region of the cell near the junction, and the region of the cell behind the nucleus was fully attached to the substrate via cell-ECM adhesion with negligible deformation. This assumption was validated by tracking the movement of marker points inside the nucleus region, and the results showed that compared with the elongation of the region of the cell near to the junction, the region behind the nucleus remained relatively unmoved (**Figure 4-2**). Understandably, cells adhered to the device via discrete focal adhesion spots at the base of the cell, and these adhesions could actively change during the stretching process. Nevertheless, under large deformation (as the deformation of the cell pair during the stretch can reach several folds of the initial length), the influence of the small variation of the initial length on the calculated stress-strain relationships can be mitigated. Force was calculated using Hooke's Law, $F = k\delta$, where k

is the sensing island stiffness obtained from the AFM experiment. The effective engineering stress was defined by dividing the calculated force by the cross-section area of the junctional region, following the same concept adopted by previous studies on epithelial monolayers (53). The cross-section area was treated as the junction length multiplied by the thickness of the cell-cell contact region. The measured data showed that the cell-cell junction length varied significantly from one cell pair to another. Thus, the length data obtained from the processing of the cell doublet images in each stretch test was used. The cell-cell contact region was found to be 10.24 μm in thickness with limited variations measured from confocal z-stack imaging (**Figure 4.1C**). The length of the junction is determined by measuring the length of the cell-cell contact with GFP-tagged E-cadherin, the nucleus-to-nucleus distances are calculated by examining the center-of-mass for the nucleus DAPI staining, and the thickness of cell-cell junctions are measured by examining the z-stack images of a single junction on a TPP-printed scaffold to determine the number of images in which the junction is in focus.

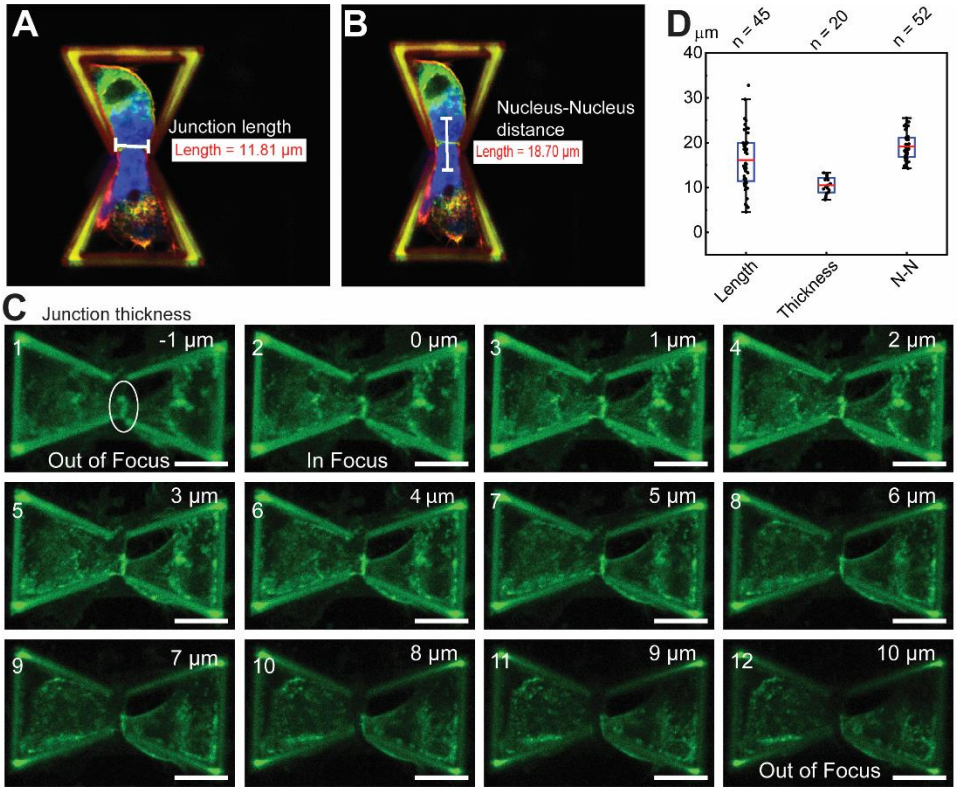

Figure 4.1. Cell-cell junction dimension quantification and analysis. **A, B)** A cell pair adhered well on the device with a cell-cell junction within the gap. The junction length was measured through the junction line which is determined with the GFP-tagged E-cadherin. The nucleus-to-nucleus distances are examined by DAPI staining. **C)** Z-stack images of a cell-cell junction for thickness measurement (scale bar = 20 μm). To determine the junction thickness, cells were deposited in bowtie structures and allowed to form junctions overnight. Then, z-stack images were taken of each bowtie structure with a cell-cell pair with a spacing of 1 μm between each image. To find the thickness of the junction, the image with the bottom of the junction in focus was determined, and then each image after was examined until the top of the junction was just out of focus. From here the thickness was determined based on the number of images between these identified images (from 2 to 12). Based on the new values, we changed our assumption for the junction area in stress calculation and recalculated all previous data. **D)** Cell-cell junction length, thickness, and the nucleus-to-nucleus distance were measured and plotted (n = 45 for junction length measurements, n = 20 for thickness measurements, and n = 52 for nucleus-to-nucleus (N-N) distance measurements).

We chose to define the initial length as the distance between the nuclei based on some observations during the stretching process. We observed that regions of the cell

nearest to the junction deformed the most, while regions behind the nucleus remained relatively unmoved. To show that the region behind the nucleus is almost intact during the stretch test, we analyzed the change in displacement of a distinctive spot as a marker with respect to the edge of the bowtie, $L_M(t)$, and compared it with the displacement difference of the two movable islands, $L(t)$. As shown by the representative frames of a stretch test example, the marker, approximately in the region of the cell nucleus, was displaced only slightly from its original position relative to the edge of the bowtie ($L_M(0)$) and the maximum $L_M(t)$ reaches only 1.8 μm as compared to the maximum of $L(t)$ at 47.5 μm. Therefore, we assumed that the cell is fully anchored behind the nucleus, and while there may be some adhesions on the side near the junction, the majority of the deformation happens in this region, and these adhesions are most likely ruptured first, making this assumption more accurate. We do understand this assumption is not perfect and that there are a number of confounding factors to introduce error into the strain calculation. However, under large deformation (as the deformation of the cell pair during the stretch can reach several folds of the initial length), the influence of these errors on the calculated stress-strain relationships is mitigated.

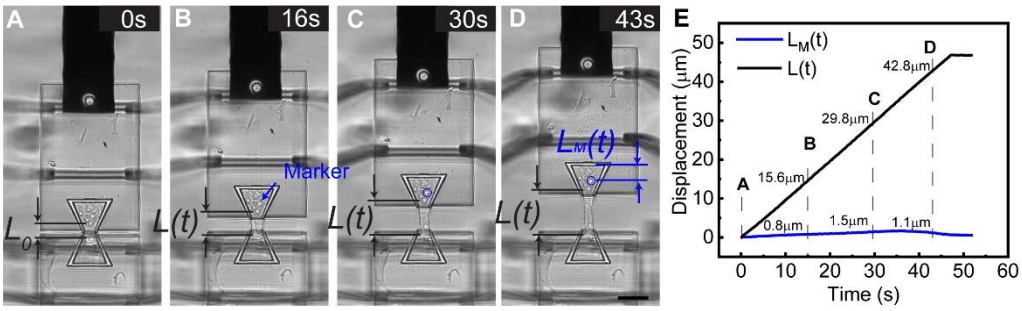

Figure 4.2. Initial length calculation. A-D) Selected frames from an example stretch test showing the displacement of the upper island with respect to the lower island, $L(t)$, and the displacement of a marker close to the nucleus of the cell on the upper island with respect to the edge of the bowtie, $L_M(t)$. **E)** Plot of the displacement change over the course of the stretch test for $L(t)$ and $L_M(t)$. Scale bar = 20 μm.

A modified version of MATLAB digital image correlation (DIC) was used to analyze the frames from the stretch test. The first frame was considered as the reference and the rest of the frames were compared to the reference frame to calculate the displacement of each island. A region of interest with markers within the region was defined for both islands. Then, the MATLAB code calculated the markers' new coordinates with respect to the first frame, from which the displacement of the islands was calculated (**Figure 4.3**).

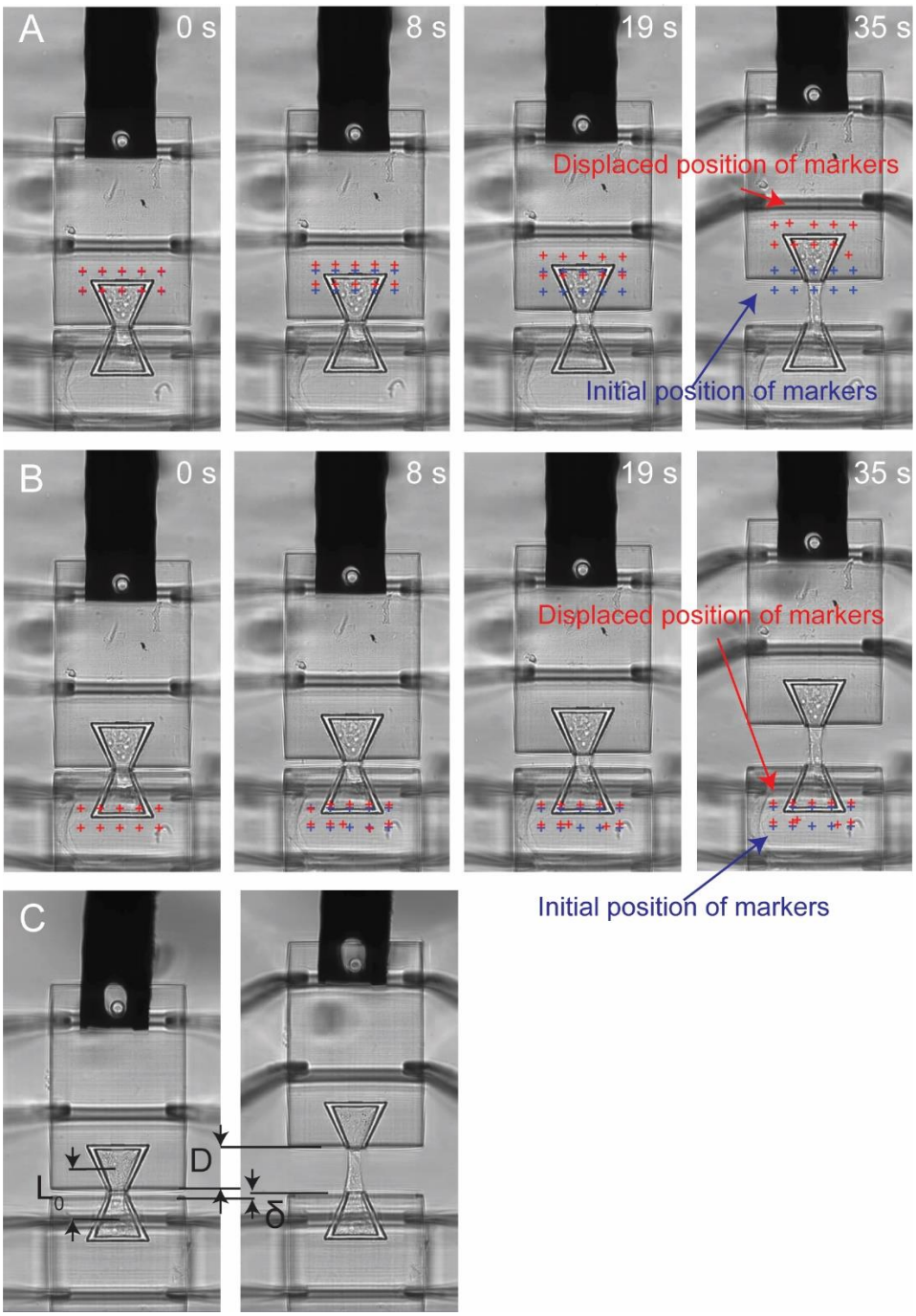

Figure 4.3. Stress-strain curve calculation from the capture video frame of mechanical testing. **A)** Four representative frames showing the initial and new markers for displacement tracking. **B)** Parameters definition for strain and stress calculation. **C)** A representative stress-strain curve.

To interrogate the mechanical behavior of the cell-cell junction, we stretched the junction by displacing Island 2 at different rates. We examined four strain-rates ranging

from 0.005 s^{-1} to 0.5 s^{-1} and observed different modes of stress relaxation and cell-cell adhesion failure that are strongly strain-rate dependent. We first stretched the cell pair at a strain rate of about 0.005 s^{-1} (100 nm/s in displacement rate) and observed that none of the junctions failed at the end of the 50 μm displacement. A typical set of time-series images shows that there is no sign of rupture in the cell-cell junction (**Figure 4.4A**). The stress-strain curve exhibits a typical viscoelastic behavior wherein the stress increases nonlinearly with a decreasing rate as the strain increases, and the cell pairs are elongated to a maximum strain of 221.8 ± 8.2% at a maximum stress of 1.72 ± 0.73 kPa (**Figure 4.4B**). Under a strain rate of 0.05 s^{-1}, cell-cell junctions begin to show some signs of rupture through a gradual necking process seen in the time-series images and experience a maximum strain of 217.8 ± 10.0% and stress of 1.09 ± 0.63 kPa at the point of failure (**Figure 4.5A, B**). The stress-strain curve shows three different regions: a viscoelastic region, a plateau region (i.e. necking process), and a linear region up to failure at 217.8% strain. Among all the stretch tests performed under this strain rate ($n > 20$), 47% of them resulted in complete cell-cell adhesion rupture, indicating that 0.05 s^{-1} may represent a critical strain rate beyond which stress accumulation induced by mechanical stretching outperforms stress relaxation. Similar observations can be made from a strain rate of 0.25 s^{-1} with a less obvious plateau region, a higher stress level at failure, and more rapid and complete junction failure (**Figure 4.6A, B**). All stretch tests at the strain rate of 0.25 s^{-1} resulted in complete junction rupture, in clear contrast to the 0.05 s^{-1} strain rate. At a strain rate of 0.50 s^{-1}, the stress-strain curve starts with a viscoelastic region, followed by a linear region up to the rupture point. A stress level of 3.04 ± 1.36 kPa was observed at the failure point and junctions failed at 215.1 ± 37.4% strain (**Figure 4.7A, B**). The gradual disappearance of the plateau region from low

strain rate to high strain rate tests suggests stress accumulation at high strain rate due to lagging and inadequate stress relaxation.

Our tensile tests demonstrate that the cell pair can withstand a remarkably large strain level before the cell-cell junction completely ruptures. This clearly contrasts with data obtained from suspended cell doublets without a mature cell-cell adhesion using dual micropipette aspiration (DPA), in which cadherin bonds rupture at small strain and low levels of stress(226). Under low strain rates, the cell-cell junction remains largely intact even when the strain is higher than 200%. Comparing with the 0.50 s^{-1} strain rate, the lower maximum stress under the strain rate of 0.005 s^{-1}, where cell-cell adhesion complexes remain largely intact, indicates the existence of another effective stress dissipation scheme inside cells. Considering the dynamic nature of cytoskeletons among all the intracellular structures, we speculate that the mechanical stress is dissipated via the remodeling and reorganization of their cytoskeletons. However, under high strain rates, the cell pair dissipates stress primarily through the dissociation of cell-cell adhesion complexes and complete breakage occurs at a strain level of ~200%. In addition, all failures occur at the cell-cell contact symmetrically through the rupture of the cell-cell adhesion complex, as observed from stretching tests at different strain rates (**Figure 4.8**). The image series of the tensile test (**Figures 4.4A, 4.5A, 4.6A, 4.7A**) and the zoom-in images of the cell-cell adhesion region (inset of **Figures 4.4B, 4.5B, 4.6B, 4.7B**) show the decrease in length of the mutual cell junction until complete separation, suggesting intermediate bond dissociation accompanying the straining process which leads to ultimate cell adhesion complex failure. The absence of asymmetrical failure, potentially at the cytoskeleton to cell membrane tether at one side of the cell pair, implies that the cell-cell adhesion complex

represents the weakest link in the cytoskeleton-cell adhesion-cytoskeleton system. Moreover, the rupture of the cell-cell junction occurs gradually at lower strain rates, like unzipping a zipper, with localized snap and retraction of the cytoskeleton near the failure point at the edge of the cell-cell contact.

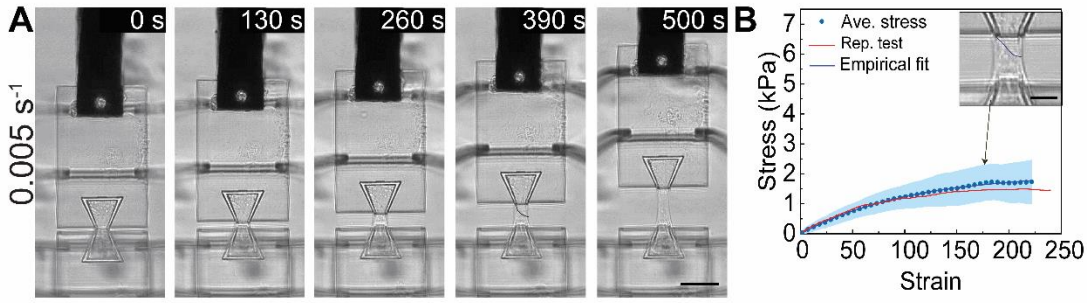

Figure 4.4. Representative image frames and the corresponding stress-strain curves for stretch tests performed at strain rates of 0.005 s^{-1}. Average stress-strain curve (Avg. stress, dotted line) ± standard deviation (blue region) (223).

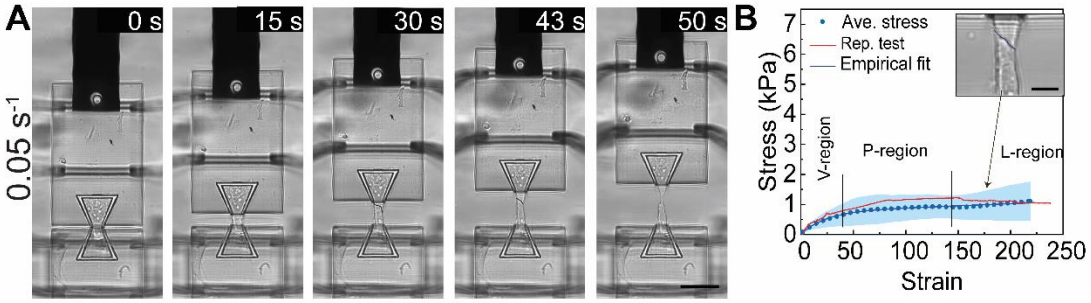

Figure 4.5. Representative image frames and the corresponding stress-strain curves for stretch tests performed at strain rates of 0.05 s^{-1}. Average stress-strain curve (Avg. stress, dotted line) ± standard deviation (blue region) (223).

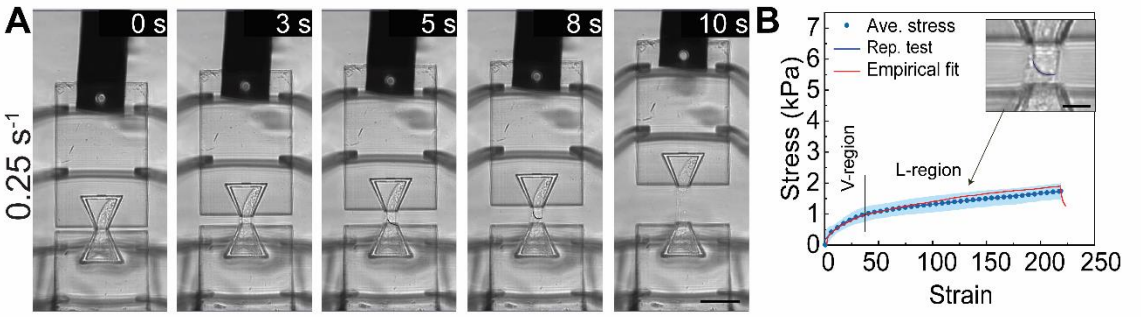

Figure 4.6. Representative image frames and the corresponding stress-strain curves for stretch tests performed at strain rates of 0.25 s^{-1}. Average stress-strain curve (Avg. stress, dotted line) ± standard deviation (blue region) (223).

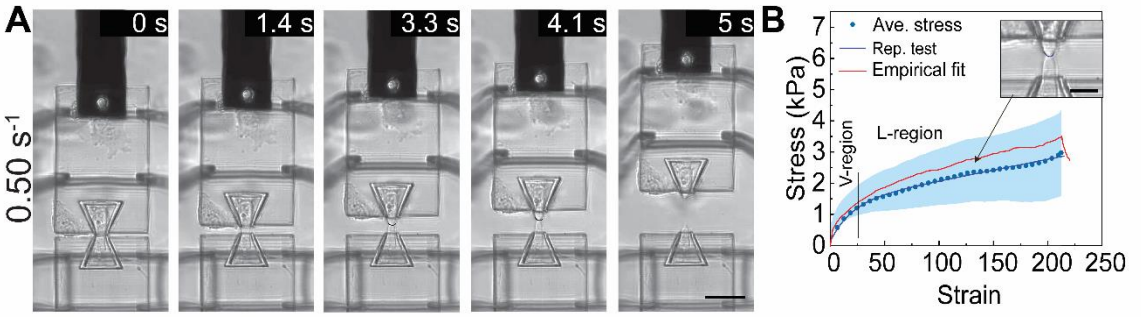

Figure 4.7. Representative image frames and the corresponding stress-strain curves for stretch tests performed at strain rates of 0.50 s^{-1}. Average stress-strain curve (Avg. stress, dotted line) ± standard deviation (blue region) (223).

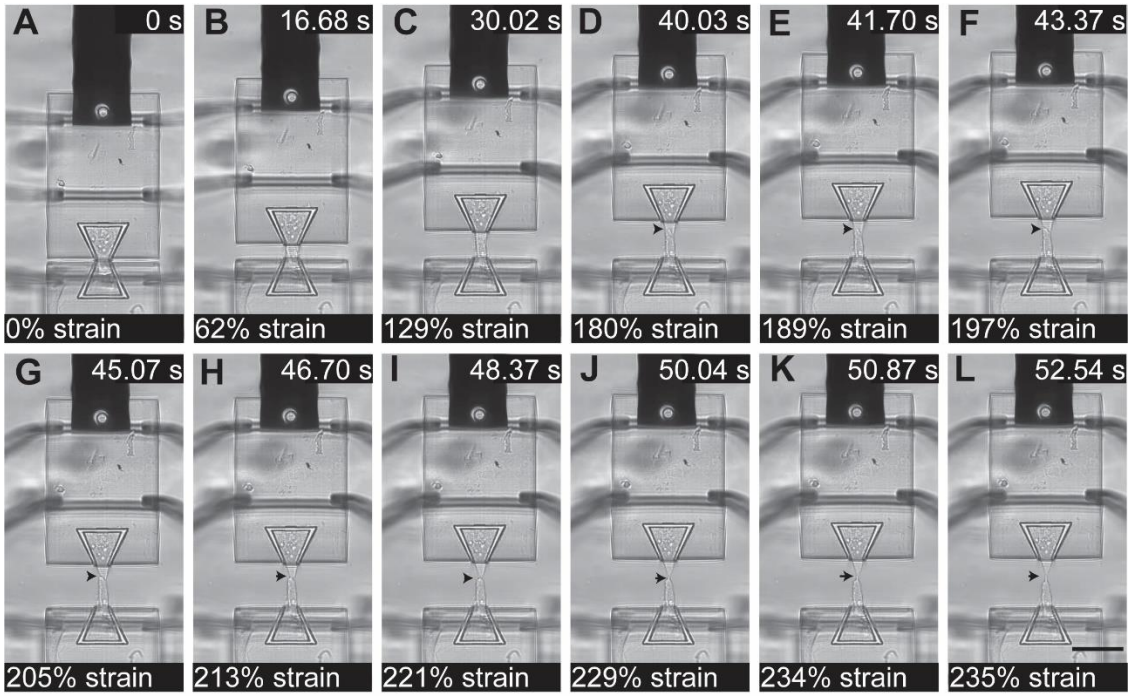

Figure 4.8. A representative time-lapse series of frames show the cell junction ruptured symmetrically under an increasing strain. The arrowhead indicates the cell-cell junction in each frame. Scale bar: 20 μm.

4.2. A mechanosensing constitutive model for the viscoelastic behavior of a cell pair

The stress-strain relationships from the four types of tensile tests of varied strain rates can be well fitted with an empirical exponential growth function plus a linear function: $\sigma = -Ae^{-B\varepsilon} + C\varepsilon$, supporting an overall viscoelastic behavior (**Figures 4.4, 4.5, 4.6, and 4.7**). Considering that the cell membrane deforms along with their intracellular components when a pair of cells are stretched, the standard linear solid (SLS) model (**Figure 4.9A**), consisting of a Maxwell branch and an elastic branch, is the simplest model that can effectively capture such a viscoelastic behavior.

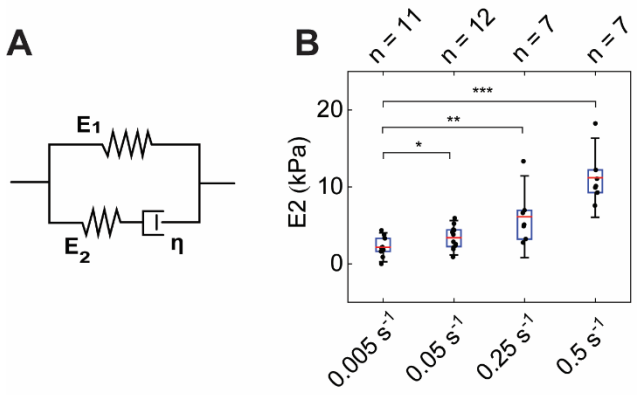

Figure 4.9. Fitting the stress-strain curves with the Standard Linear Solid (SLS) model. A) Diagram of the SLS model. **B)** The predicted spring constant E2 as a function of the strain rate. The equation for the SLS model: $\dot{\sigma}_{tot} + \frac{E_2}{\eta}\sigma_{tot} = \frac{E_1 E_2}{\eta}\varepsilon_{tot} + (E_1 + E_2)\dot{\varepsilon}_{tot}$ can be solved for a constant strain rate: $\sigma_{tot} = \eta\dot{\varepsilon}_{tot}\,(1 - e^{\left(-\frac{E_2}{\eta}t\right)}) + E_1\varepsilon_{tot}$. This equation was used to fit the stress-strain curves at strain rates: 0.005 s-1, 0.05 s-1, 0.25 s-1 and 0.5 s-1.

The SLS model has been widely used to model the mechanical responses of suspended cells, where the Maxwell branch represents the intracellular components while the elastic branch represents the plasma membrane (227). Since minimal deformation of the cell nuclei was observed even at a strain level as large as 200% in our tensile tests, we expect that the elastic element in the Maxwell branch is primarily contributed by the cytoskeleton. Although the SLS model can reproduce the general shape of the stress-strain relationships, it predicts that the elastic modulus of the spring in the Maxwell branch increases with the increase in the strain rate (**Figure 4.9B**). This prediction is in contradiction to the fact that cytoskeleton growth hardly occurs at high strain rates given the limited response time. Alternatively, we modified the SLS model by incorporating a mechanosensing component to account for the stress dissipation mediated by cytoskeleton remodeling (228, 229). As shown in **Figure 4.10A**, the spring with Young's modulus of

E_1 represents the cell membrane while the second spring with Young's modulus of E_2 and the dashpot with the viscosity of η represent the elastic and viscous elements of intracellular components, respectively. The viscous component is contributed by the combined effect of cytoplasmic and cytoskeleton friction (230). The cytoskeleton of adherent cells constantly undergoes reorganization through dynamic assembly and disassembly to maintain its mechanical homeostasis in response to the tensile load. We expect that the elastic element of intracellular components is primarily contributed by the cytoskeleton, and E_2 can be considered as the collective moduli of all stress fibers that sustain the load and should be proportional to the number of individual stress fibers within the plane perpendicular to the stretching direction, as demonstrated by the inset in **Figure 4.10A**. The value of E_2 should be collectively determined by the cell-cell junction length and cell-cell adhesion complex density. The continuous growth of the cytoskeleton is expected to lead to an increase in the resting length of the second spring, which could partially or even completely relax the passive stress (σ_{S2}) resulting from stretching:

$$\sigma_{S2} = E_2(\varepsilon_{S2} - \varepsilon_0) \tag{4-1}$$

where ε_{S2} and ε_0 are the total strain of the second spring and the strain resulting from the continuous growth of the cytoskeleton, respectively. We relate the cytoskeleton growth rate with the strain rate of the second spring through a model parameter α:

$$\dot{\varepsilon}_0 = \alpha\dot{\varepsilon}_{S2} \tag{4-2}$$

where $0 \leq \alpha \leq 1$. When $\alpha = 0$, $\dot{\varepsilon}_0 = 0$, suggesting that the cytoskeleton does not grow at all, which corresponds to stretch with a very high strain rate. When $\alpha = 1$, equation (4-2) reduces to $\dot{\varepsilon}_0 = \dot{\varepsilon}_{S2}$, indicating that the growth of the cytoskeleton is able to completely release the passive stress, which could occur under stretch with an extremely

low strain rate. Therefore, α can be considered as an effective parameter to indicate the growth level of the cytoskeleton during the stretch test and thus the stress dissipation efficiency. The model predicts the following time-dependent relationship between stress (σ_{tot}) and strain (ε_{tot}):

$$\dot{\sigma}_{tot} + \frac{(1-\alpha)E_2}{\eta}\sigma_{tot} = [E_1 + (1-\alpha)E_2]\dot{\varepsilon}_{tot} + \frac{(1-\alpha)E_1E_2}{\eta}\varepsilon_{tot} \quad (4\text{-}3)$$

Under a constant strain rate condition, Eqn. (3) yields:

$$\sigma_{tot} = E_1\varepsilon_{tot} + \eta\dot{\varepsilon}_{tot}\left[1 - \exp\left(-\frac{(1-\alpha)E_2}{\eta}\frac{\varepsilon_{tot}}{\dot{\varepsilon}_{tot}}\right)\right] \quad (4\text{-}4)$$

As shown in **Figure 4.10B, C**, equation (4-4) can robustly capture the viscoelastic responses of cells under different strain rates. Fitting the stress-strain curves obtained in our stretch tests with Eqn. (4) allows us to predict how E_1, $(1-\alpha)E_2$ and η vary with the strain rate.

Our model predicts that E_1 is independent of the strain rate and has an average value of ~1.2 kPa (**Figure 4.10D**), which is consistent with previously reported values (230, 231). The viscosity η is predicted to monotonically decrease with the strain rate (**Figure 4.10E**), suggesting that the cytoplasm is a shear-thinning material. Such a shear-thinning feature has been identified for the cytoplasm of several other types of cells previously(232, 233). Plotting the predicted viscosity against the strain rate in a logarithmic scale reveals that the mechanical behavior of the cytoplasm can be approximated as a power-law fluid following the Oswald equation, i.e. $\eta = K\dot{\varepsilon}^{(n-1)}$, with the exponent of $n = -0.104$ (**Figure 4.10G**). In general, shear thinning is caused by flow-facilitated disentanglement of polymer chains, which is consistent with the expected enhanced alignment of cytoskeleton structures after

cells are subjected to uniaxial stretching (234). Since the cells are expected to have similar cytoskeleton structures to start with, we can directly compare the stress dissipation efficiency mediated by the cytoskeleton growth by assuming that E_2 has the same value. The predicted decrease in α from low strain rate to high strain rate suggests that the stress dissipation efficiency decreases with strain rate as a result of reduced cytoskeleton growth (**Figure 4.10F**). The predicted rate-dependent growth of the cytoskeleton is supported by the clear difference in the residual plastic strain after releasing the tensile load in our hysteresis tests (**Figure 4.10H**). We stretched the cell pair under two different strain rates (0.005 s^{-1} and 0.50 s^{-1}) to a strain level of about 40% and then completely released the mechanical load. The cell pair stretched under the strain rate of 0.005 s^{-1} resulted in a plastic strain of ~20%. However, less than 10% plastic strain is observed for the cell pair stretched under the strain rate of 0.50 s^{-1}, suggesting limited cytoskeleton growth under the high strain rate.

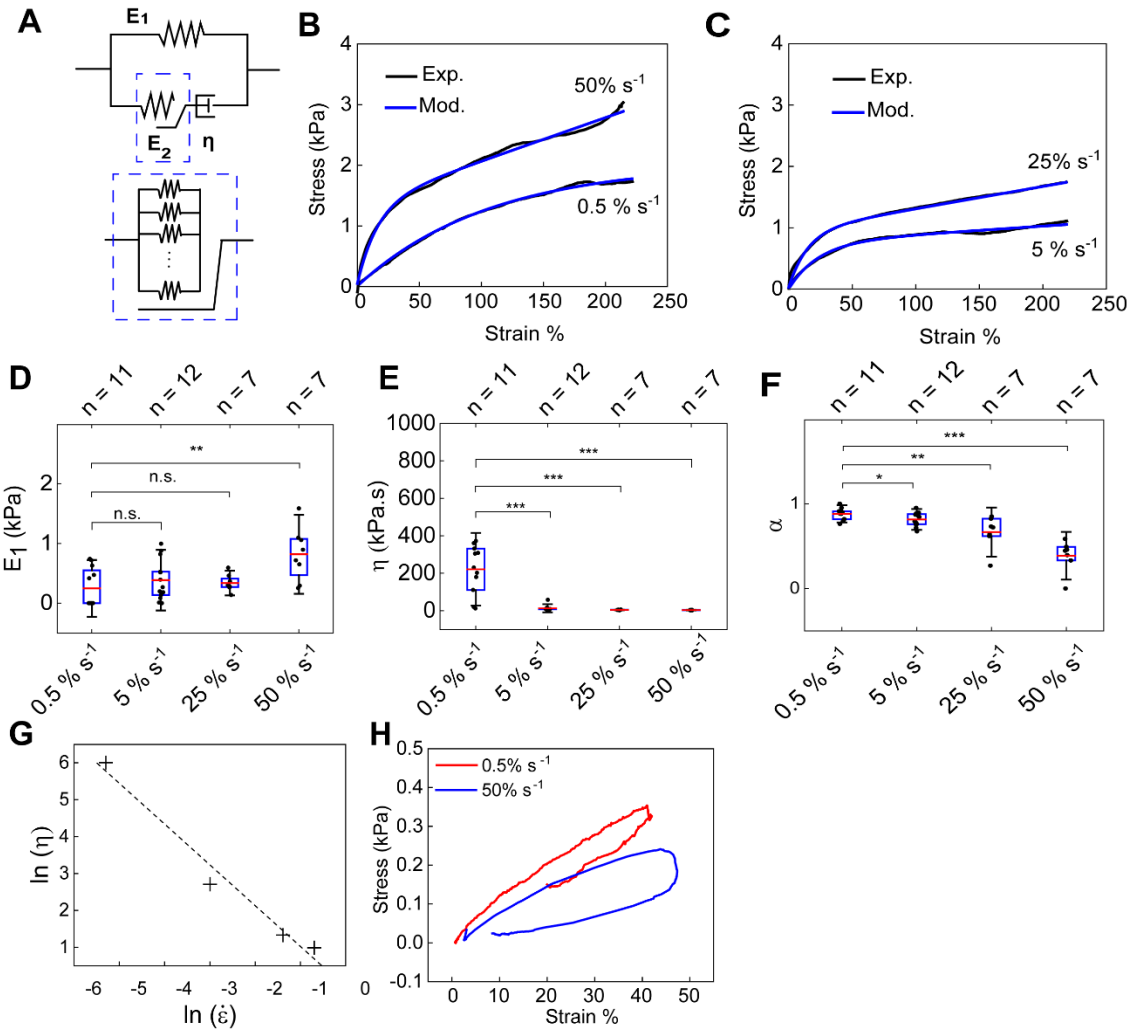

Figure 4.10. Strain rate-dependent and actomyosin contractility-controlled viscoelastic behavior of the cell pair. A) Diagram of the modified standard linear solid (MSLS) model that was used for fitting the experimental data. **B, C)** The stress-strain curves obtained by applying stretch at different strain rates (0.005 s-1, 0.5 s-1, 0.25 s-1, and 0.50 s-1) were fitted using Eqn. (4-4) according to the MSLS model. **D, F)** Box plots comparing the values of E_1 (d), η (e), and α (f) obtained from fitting the stress-strain curves using Eqn. (4-4) for different strain rates. **G)** The predicted viscosity is plotted with respect to the strain rates in a log-log scale. **H)** Hysteresis analysis is shown by recording the stress-strain relationship following a full cycle of application and release of tensile load on a cell pair at two strain rates (0.005 s-1 and 0.50 s-1). For each box plot, the number of experiments is indicated on top of each graph. *: $p<0.05$, **: $p<0.01$, ***: $p<0.001$ (223).

We next subjected the cell pair to cellular contractility modulators, RhoA Activator I: CN01, and myosin II inhibitor: blebbistatin (Bleb), to examine the impact of actomyosin activity on the mechanical behavior of the cell pair under mechanical stress. Stress-strain curves collected at a strain rate of 0.005 s^{-1} show a clear contrast between samples treated with CN01, Bleb, and DMSO control. Investigation of cellular contractility was performed using CN01, control DMSO, and Bleb with a 0.005 s-1 (100 nm/s) strain rate, and representative frames are shown in **Figure 4.11**. Control DMSO compared to control at 0.005 s-1 showed a sign of rupture because of DMSO (**Figure 4.11A**). CN01 increased the stress level and rupture did not occur in this test (**Figure 4.11B**). Since Bleb inhibits the myosin II pathway, the cell-cell adhesion junction ruptured at the initial stages and the stress level was low compared to other conditions (**Figure 4.11C**). Specifically, CN01 raises the overall stress level compared with controls at the same strain, while Bleb reduces the stress accumulation (**Figure 4.12A**). The stress-strain curves were then analyzed using the constitutive model. As expected, E_1 stays the same for all conditions (**Figure 4.12B**). Enhancement of actomyosin contractility by CN01 significantly increases η and E_2, while Bleb reduces both of them (**Figure 4.12C, D**). The increase (decrease) in both η and E_2 by CN01 (Bleb) is consistent with the enhanced (reduced) stress fiber formation.

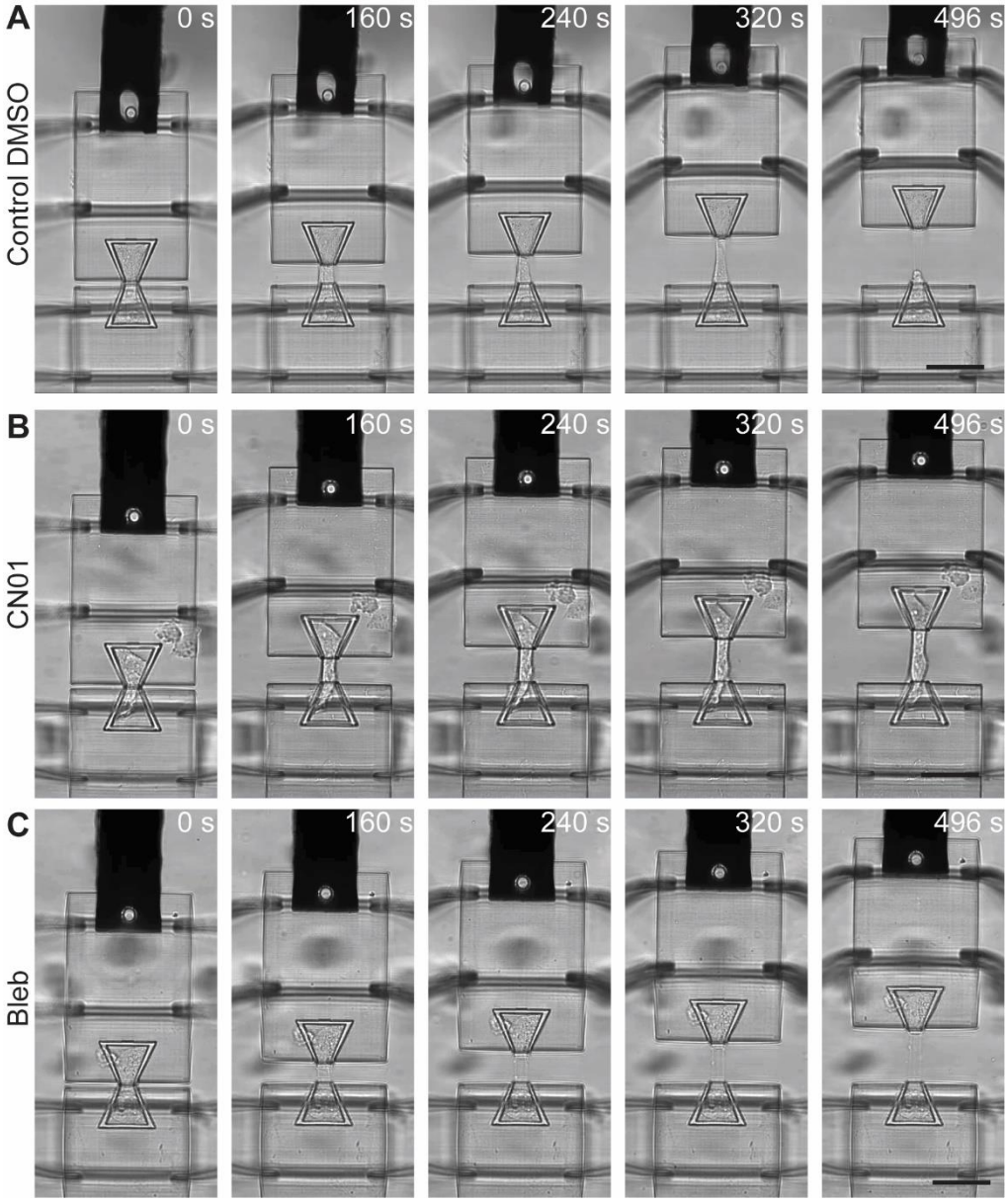

Figure 4.11. Series of frames for CN01, control, and bleb under 0.005 s-1 strain rate stretch test. A) Control DMSO. **B)** CN01. **C)** Bleb. Scale bar: 50 µm.

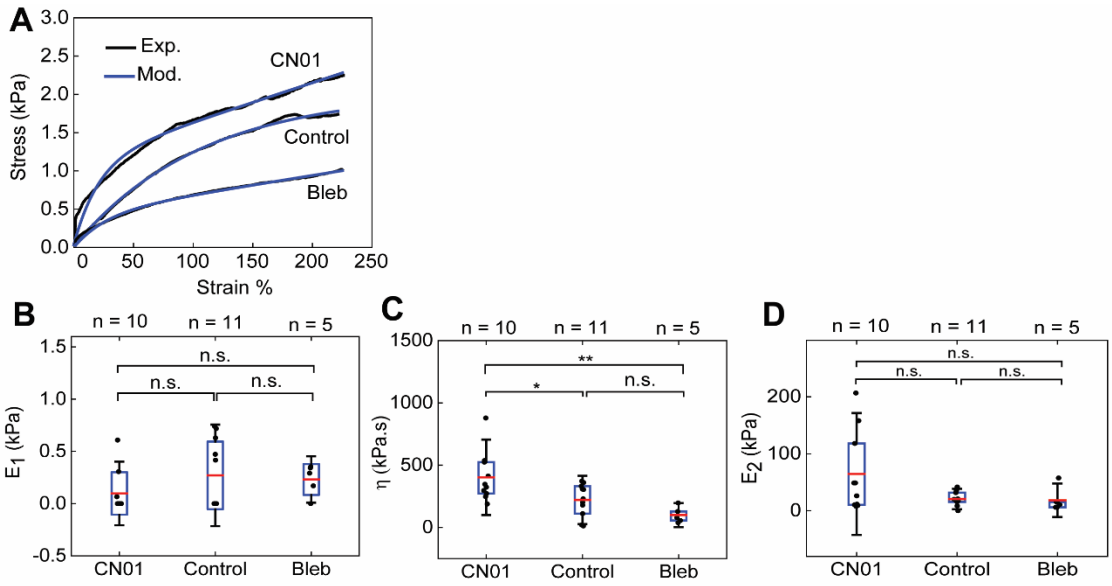

Figure 4.12. The effect of cytoskeleton dynamic on the stretch test. A) The stress-strain curves obtained by stretching cells treated with CN01, Bleb, and DMSO control at a rate of 0.005 s-1 are fitted using Eqn. (4-4). **B-D)** Box plots comparing the values of E_1 (B), η (C), and E_2 (D) obtained from fitting the stress-strain curves for cells treated with CN01 and Bleb using Eqn. (4-4). For each box plot, the number of experiments is indicated on top of each graph. *: p<0.05, **: p<0.01, ***: p<0.001 (223).

It is worth mentioning that the stress increase induced by CN01 can be partially suppressed by subsequent addition of ROCK inhibitor, exhibiting a reverse effect on the contractility modulation which can be captured dynamically by our SCAµTT platform (**Figure 4.13**). Collectively, our data support the idea that stress dissipation is facilitated by the actin filament growth during tensile loading conditions.

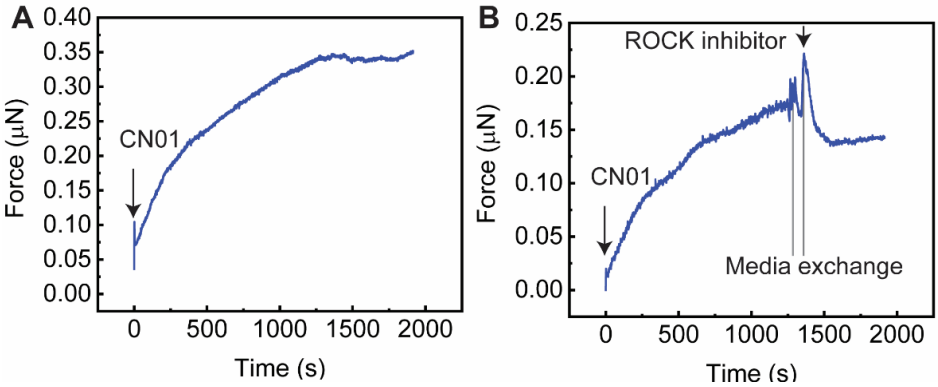

Figure 4-13. Reversal of the stress modulation effect of a RhoA activator by ROCK inhibitor. **A)** Temporal evolution of the force sustained by a cell pair in response to CN01 (1 unit/ml) while maintaining a constant strain of 0.5. **B)** Temporal evolution of the force sustained by a cell pair in response to sequential addition of CN01 (1 unit/ml) and ROCK inhibitor while maintaining a constant strain of 0.5.

4.3. Cadherins strengthening and rupture under rate-dependent stretch of cell-cell junction

We attribute the observed necking process to the rupture of cell-cell adhesion bonds, which is most apparent under the intermediate strain rate. A few cadherin bonds are ruptured in discrete steps at the edge of the cell-cell junction, which corresponds to a small drop in the measured forces in the force-displacement curve (**Figure 4.14**). To investigate the bond rupture, we selected a representative example of the stretch tests at the strain rate of 0.05 s^{-1} with obvious regions of junction rupture followed by stiffening, which is represented by each drop and rise in the curve (**Figure 4.14A**). The rupture of bonds releases the force in the stress fibers that were in direct connection with the bonds and locally relaxes the stretched cell membrane, consequently leading to a drop of the measured force. One representative region of interest (ROI) is plotted in **Figure 4.14B**, in which a total force drop of 5 nN and a junction length reduction of ~3 μm were observed for an approximately 490 nm displacement. Correspondingly, a total of ten image frames were

captured showing the snap and retraction of the cytoskeleton at the edge of the cell-cell junction (**Figure 4.14C**), and each discrete snap motion corresponds to a small drop in force. Considering the strength of a single cadherin bond of around 40 pN (235), this decline is the result of rupturing about a few hundred cadherin bonds in each discrete event with a resolution of a few bonds.

The bond dissociation events also exhibit strong strain-rate dependency. First, at a very low strain rate, the absence of bond rupture may be attributed to cadherin strengthening. This is confirmed by the clustering of GFP-tagged E-Cad when the cell doublet is subject to low levels of strain (<100%) at the strain rate of 0.05 s^{-1} (**Figure 4.15**). It has been observed that cadherin bond clustering in epithelial cells under tensile load occurs in a time scale of minutes, right in line with the time span of a low strain rate tensile test (about 10 minutes)(40). Second, the critical stress level at which cadherin bonds show initial signs of dissociation increases significantly with increasing strain rate (**Figure 4.14D**). As shown in **Figure 4.14E**, the initiation of bond rupture events occurs at similar strain levels of around 100% for all three strain rates. However, the critical stress is significantly higher for 0.50 s^{-1} (4.04 kPa) compared with 0.5 s^{-1} and 0.25 s^{-1} (0.99 kPa and 1.72 kPa, respectively).

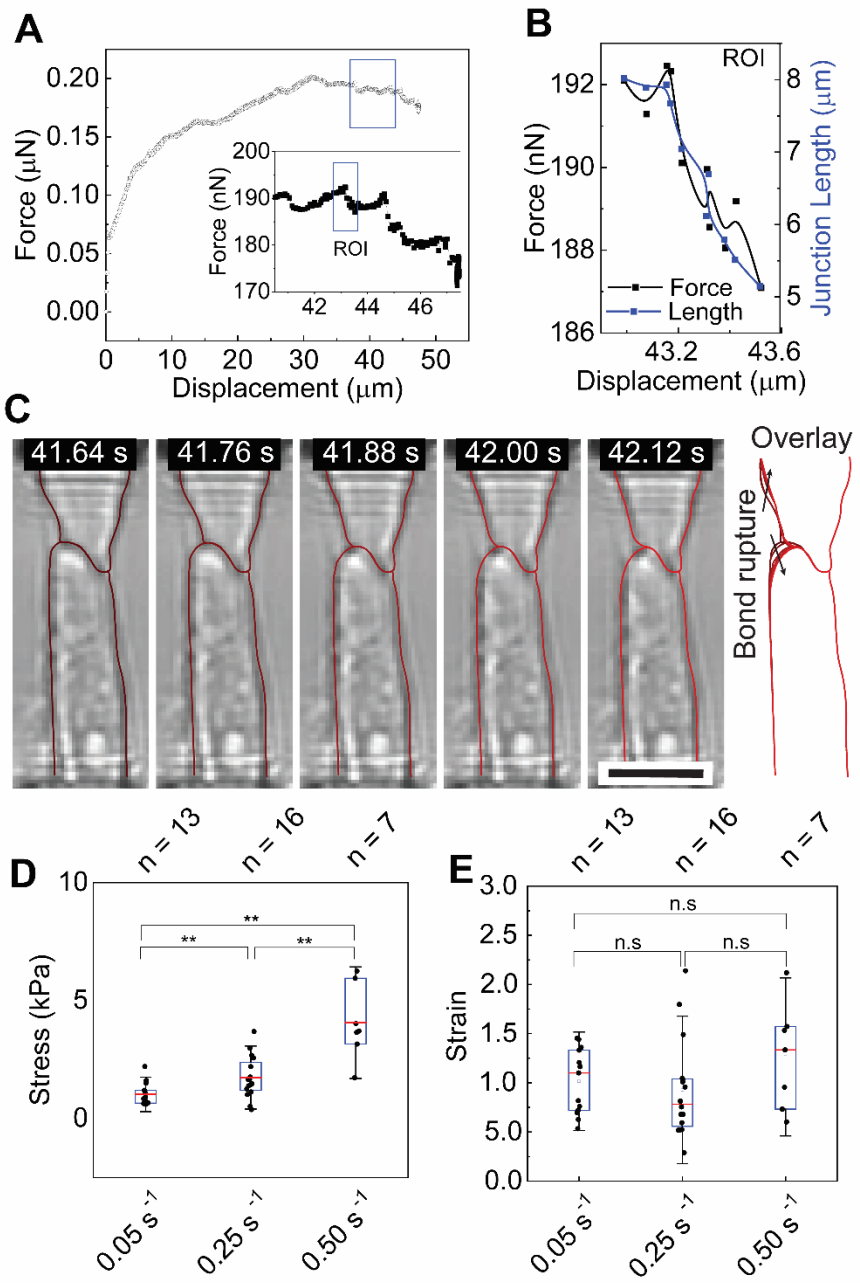

Figure 4.14. Cadherin bond rupture exhibits rate-dependent behavior during strain-rate controlled stretch. A) A representative force-displacement curve obtained at a strain rate of 0.05 s-1 is shown. Inset shows the zoom-in of the portions of the force-displacement curve indicated in the box. **B, C)** The force-displacement curve (black curve) and junction length (blue curve) (B) within the region of interest (ROI) in the inset of a are shown, with the outline of each cell traced in corresponding frames (C). The overlay in c shows the change in cell-cell junction length and shape of each cell (dark red in the first frame and light red in the last frame). **D, E)** Stress levels (D) and strain levels (E) at which the initiation of bond rupturing

occurs for the tensile tests at different strain rates: 0.05 s-1 (n = 13), 0.25 s-1 (n = 16), and 0.50 s-1 (n = 7). *: $p<0.05$. Scale bars: 25 μm in the inset of C (223).

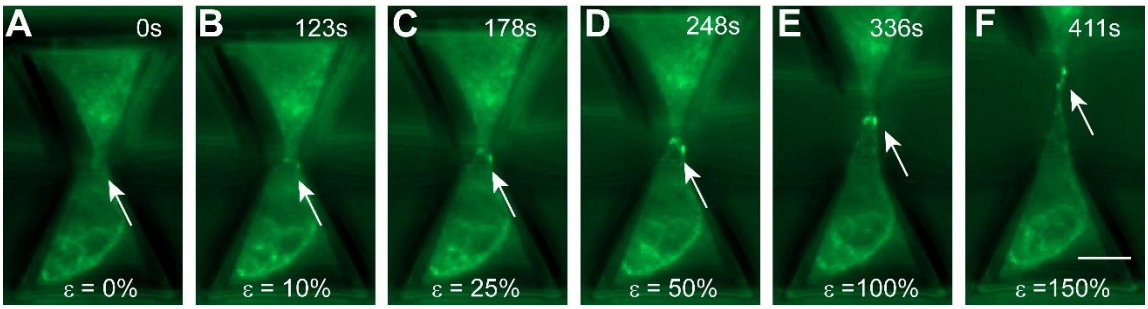

Figure 4.15. E-cadherin clustering in cell-cell junction under applied strain. A) Under 0 strain, A431 GFP-tagged E-cadherin cells have a little expression of E-cadherin at cell-cell junction. **B-E)** As strain is increased to 10, 25, 50, and 100, respectively, E-cadherin signal increases at the cell-cell junction, indicating clustering of E-cadherin in response to stretch. **F)** At 150 strain E-cadherin begins to retract from the cell-cell contact. Scale bar: 20 μm.

Considering the time span of a few seconds for a tensile test at the strain rate of 0.50 s^{-1}, bond clustering may not be the main contributor to the observed increase in the critical stress. On the other hand, the observed increase in the strength of cadherin bonds agrees well with previous reports from single molecule force microscopy studies of E-Cad bonds, which showed that the peak rupture force in E-Cad bonds increases logarithmically with the loading rate (235, 236). Knockdown of E-Cad by siRNA resulted in a decrease in the overall stress level during the strain application. To determine the E-cadherin bond effect on the stress-strain curve and bond rupture initiation, E-cadherin siRNA was transfected into A431 GFP-tagged E-cadherin cells. Transfection of E-cadherin siRNA (SCBT; SC35242) and control siRNA (SCBT; SC37007) were performed using Lipofectamine RNAiMAX Transfection Reagent (Invitrogen), according to the manufacturer's protocol. The expression of GFP was analyzed by fluorescence microscopy

after 48h. Full-length human E-cadherin fused at its C-terminus to GFP was constructed by first inserting an E-cadherin cDNA into pEGFP-N2 (Clontech, Mountain View, CA) and then inserting the tagged construct into a derivative of the LZRS retroviral expression vector. The final cDNA construct was fully sequenced to ensure no errors were introduced during subcloning. Cells were incubated with control siRNA and E-cadherin siRNA both using the Lipofectamine RNAiMAX reagent. The inhibition of E-cadherin expression was confirmed by fluorescence microscopy and immunoblotting. A knockdown of E-cadherin expression could be visualized by fluorescence microscopy after 48 h transfection. Also, immunoblotting showed that the protein levels of E-cadherin were dramatically decreased in the E-cadherin siRNA samples (48 h, 72 h, and 96 h) compared to control siRNA. These results show that E-cadherin siRNA downregulated the E-cadherin expression effectively (**Figure 4.16)**. Note, since we used A431 cells having GFP-tagged E-cadherin, the immunoblotting showed two bands for endogenous E-cadherin (120 kDa) and GFP-tagged E-cadherin (at around 150 kDa due to the addition of GFP of 27 kDa). The control siRNA sample displayed the same two bands, and E-cadherin siRNA induced decreases in both bands. Tensile test data (**Figure 4.17A-C**) compared the control siRNA and E-cadherin siRNA.

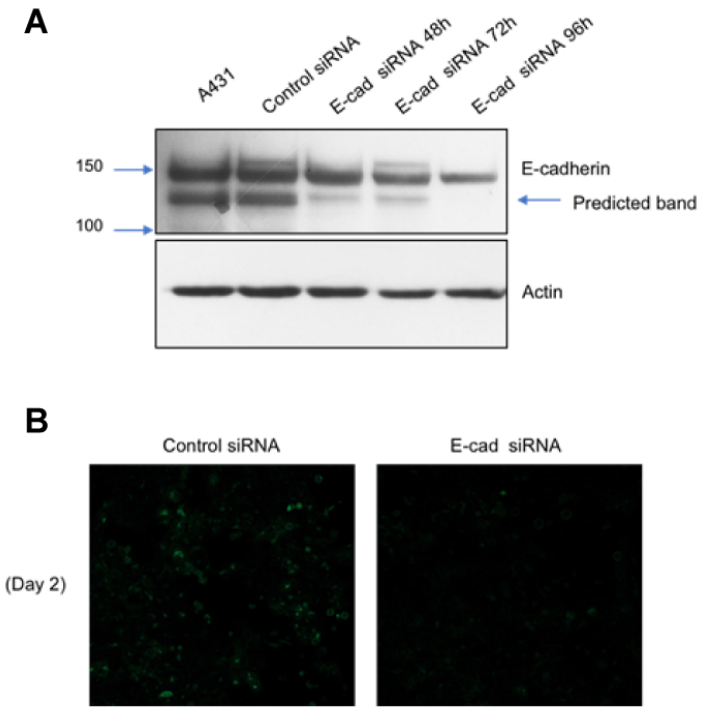

Figure 4.16. Confirmation of E-cadherin siRNA silencing. **A)** A431 GFP-tagged E-cadherin cells were transfected with control siRNA or E-cadherin siRNA. After 48 h, 72 h, and 96 h post-transfection with E-cadherin siRNA, expression levels of E-cadherin were decreased in both endogenous E-cadherin (120 kDa) and GFP-tagged E-cadherin (at around 150 kDa), as assessed by immunoblot. Actin levels were not affected by the siRNA transfection. **B)** GFP signal in GFP-tagged E-cadherin A431 cells was observed after 48 h transfection with control siRNA and E-cadherin siRNA by immunofluorescence.

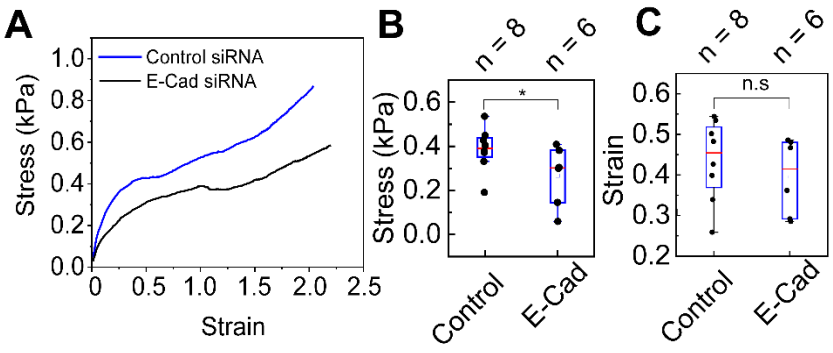

Figure 4.17. The role of E-cad on the cell stretch test. A-C) Average stress-strain curves (A) as well as stress levels (B) and strain levels (C) at which the initiation of bond rupturing occurs, for tensile tests at 0.05 s-1 on cells with E-Cad siRNA knockdown (n = 6) and control siRNA (n = 8). *: $p<0.05$ (223).

Analysis of the stress-strain curves of E-Cad knockdown cell pairs showed a significant decrease in the critical stress, as compared with controls using control siRNA. Interestingly, the strain levels at which cadherin bonds initiate unbinding remain unchanged with E-Cad knockdown (**Figure 4.16C**). This may suggest that the reduction in the number of E-Cad bonds decreased the total tension within the cytoskeleton network and thus the stress level during stretching, while the remaining bonds still rupture at similar strain levels. Collectively, our results demonstrate that E-Cad adhesions regulate the load-bearing potential of the cell-cell junction under tensile load and play a major role in the rate-dependent strengthening of the cell-cell junction.

4.4. Discussion

In this study, we fabricated a polymeric microstructure using TPP for displacement application and force sensing to examine the rate-dependent mechanical behavior of a single cell-cell adhesion complex. To faithfully characterize the intricacy of the biophysical and biochemical response of an individual cell-cell adhesion interface under large strains, a functional technique needs to fulfill the following requirements. First, it should have a highly sensitive force sensing component that allows easy quantification of pico- or nano-newton forces. Second, it should have the capability to apply mechanical strain or stress in a controlled manner. Third, the testing can be conducted under physiologically relevant conditions, especially allowing the formation of mature cell-cell junctions and cell-extracellular matrix (ECM) adhesions. Although several techniques have been developed for the quantitative assessment of cell-generated forces, including traction force microscopy (214), elastomer-based micropillar arrays (215), and 3D-printed micro-scaffolds (209, 216), they are restricted to static observations and unable to apply

mechanical stimuli, not to mention strain rate-controlled mechanical stretch. Techniques do exist to apply mechanical strain to a monolayer of cells, but the stress within individual cell-cell adhesions cannot be determined (53). Further, when a defined load is applied to individual cell-cell junctions in studies using AFM-based single-cell force spectroscopy (SCFS)(222, 237) and DPA (238, 239), it can only be carried out on isolated suspended cells where mature intercellular junctions are yet to form, and the focus can only be placed on the separation of cadherin bonds while the effect of stress relaxation of the cytoskeleton and the cell-ECM interactions are inaccessible (226).

To the best of our knowledge, SCAμTT is the first platform that allows *in situ* interrogation of the stress-strain characteristics of a mature cell-cell junction through defined strain and strain rate, promoting a paradigm shift in the mechanical characterization of cell-cell adhesions. Besides the capabilities discussed above, the throughput for mature cell-cell junction interrogation is also increased due to parallel sample preparation and testing, as the equipment for manipulating or stretching cells does not need to be used to hold cells in place during junction maturation. The presence of the mature cell-ECM junction allows for the application of large strains as in DPA, whereas the force sensitivity of the beams achieves force and displacement resolution comparable to SCFS (10 pN and 50 nm, respectively)(240). Besides its application in the mechanical characterization of single cell-cell junctions, SCAμTT can also be used to investigate the cytoskeleton mechanics and dynamics under controlled strains and/or strain rates, as well as in the study of the crosstalk between cell-cell adhesion and cell-ECM adhesion by incorporating micropillar array-based TFM into our platform. These studies can be carried out not only

on cell doublets but also on single cells and cell monolayers with minimal modification to the bowtie structure.

The ability of SCAμTT to quantify precisely the stress within a cell doublet at different strains enables us to decipher the strain rate-dependent behavior of the cytoskeleton-junction system as part of the adaptive viscoelasticity of epithelial cell-cell junctions (241). The stress-strain relationship at different strain rates reveals multiple rate-dependent stress dissipation mechanisms orchestrated by the cytoskeleton and the cell-cell junction. We showed that the cytoplasm exhibits a passive shear-thinning viscoelastic behavior following the Oswald equation. This power-law relationship between strain rate and viscosity suggests that such a passive stress dissipation mechanism plays a significant role in the stress response, particularly at high strain rates. It is worth mentioning that this relationship has been identified for the cytoplasm of suspended cells (232, 233), but has never been shown on adherent cells. In addition, we showed that the active cytoskeleton remodeling leads to continuous stress relaxation in the network of the cytoskeleton-cell junction (64). Particularly, loads with a higher strain rate result in limited cytoskeleton growth, and thus higher stress is accumulated within the network. When stress relaxation from the cytoskeleton growth fails to catch the increased stress induced by the continuous increase of the applied strain, a net accumulation of stress occurs. The increase in stress leads to the gradual unbinding of cadherin bonds to relax the stress at low strain rates. A robust junction allows a higher capacity for cytoskeleton tension, while a partially ruptured junction reduces this capacity. Although the expected active cytoskeleton remodeling has not been confirmed directly with high-resolution immunofluorescence imaging due to the strong autofluorescence of the printed microstructures on which cells are grown, it has been

validated indirectly by both the hysteresis tests and the contractility modulation experiments using cytoskeleton modulation drugs. Furthermore, as cell-cell adhesion is intimately coupled with cell-substrate adhesion (71), we expect that changing the ECM coating may affect the structure of the cell-cell junction and consequently its mechanical strength. However, we do not expect cell-ECM interaction to fundamentally change its strain rate-dependent mechanical response.

Directly measuring stress dynamics at a *single* cell-cell junction captures the real-time fracture process of junction cadherins at high strain rate. Specifically, we showed that epithelial cell-cell adhesions are mechanically the weakest linkage in the junction-cytoskeleton system and they represent the upper limit for the amount of stress that the system can tolerate before complete junction rupture occurs. However, when the cell-ECM adhesion is not sufficiently strong, failure is more likely to occur at focal adhesions. We observed that cells tended to detach from the islands during stretching experiments when a fibronectin concentration lower than 50 μm/mL was used to functionalize the bowtie structure. Moreover, we showed that, at high strain rate, stress accumulation cannot be dissipated fast enough even at low strain levels, and thus characterization of the critical strain and strain rate at which coordinated stress relaxation and E-Cad clustering can still be sufficient to mitigate stress buildup and to allow for such a remarkable strain tolerance is critical to understand epithelial fracture (242). Further, knockdown of E-Cad changed the strain rate-dependent behavior of the cell-cell junction, agreeing with previous reports that show E-Cad regulates epithelial viscoelasticity (243). This may also alter the patterns of cell proliferation and migration, which play important roles in disease outcomes. This

suggests that the mechanical interrogation platform could be used for quantifying disease states and evaluating the effectiveness of treatments.

4.5. Conclusion

In the present work, we developed a mechanical testing platform, SCAμTT, that can strain the mutual junction of a single cell pair with precisely defined strain and strain rates while simultaneously recording the junction stress. This platform allows *in situ* mechanical characterizations of a mature cell-cell junction under physiologically relevant conditions and is sensitive enough to resolve bond rupture events with a resolution of a few bonds. With this innovative platform, we performed strain-rate controlled mechanical characterization of a single mature cell-cell adhesion junction. We showed that cytoskeleton growth of the cell doublet could relax the stress buildup and prevent junction failure at low strain rates. At high strain rates, a synchronized junction failure occurs at remarkably large strain levels. We expect this platform and our biophysical understanding to form the foundation for the rate-dependent mechanics of cell-cell junctions.

CHAPTER 5

ONGOING PROJECTS

5.1. Stretch and hold analysis of a single cell pair

As one of the applications of the proposed platform, we decided to run some long-term stretch and hold experiments and interrogate the viscoelastic properties of the cell pair. After a few experiments, we noticed that cells are being tensed rather than relaxed after holding them for 30 minutes and the rate and amount of strengthening is strain-rate dependent. We went through the literature and found that there is a phenomenon called active remodeling of the cytoskeleton that happened when cells are under tension or compression. That means, when cells are under tension they try to actively remodel the cytoskeleton to respond to the external force and strengthen the cell body. In this way, they become tense and keep the cell shape. As a result, the internal stress increases. We ran this experiment for different strain rates from 100 nm/s to 10 μm/s and we noticed that at the lower strain rats, cells relaxed. The hypothesis behind this is that lower strain rates are slow enough for the cells to adapt to the condition. So, when they are held, there is not much strengthening while at the higher strain rates, cells have to respond after the stretch (**Figure 5.1A, B**). To validate this hypothesis, a few drugs have been rested on the cells. CN01 increases the stress level by activating RhoA. ROCK inhibitor decreases this activity but after about 300 seconds, cells started to remodel. Lat B completely disrupted the cytoskeleton. Therefore, cells couldn't remodel and stress levels decreased (**Figure 5.1 C, D**).

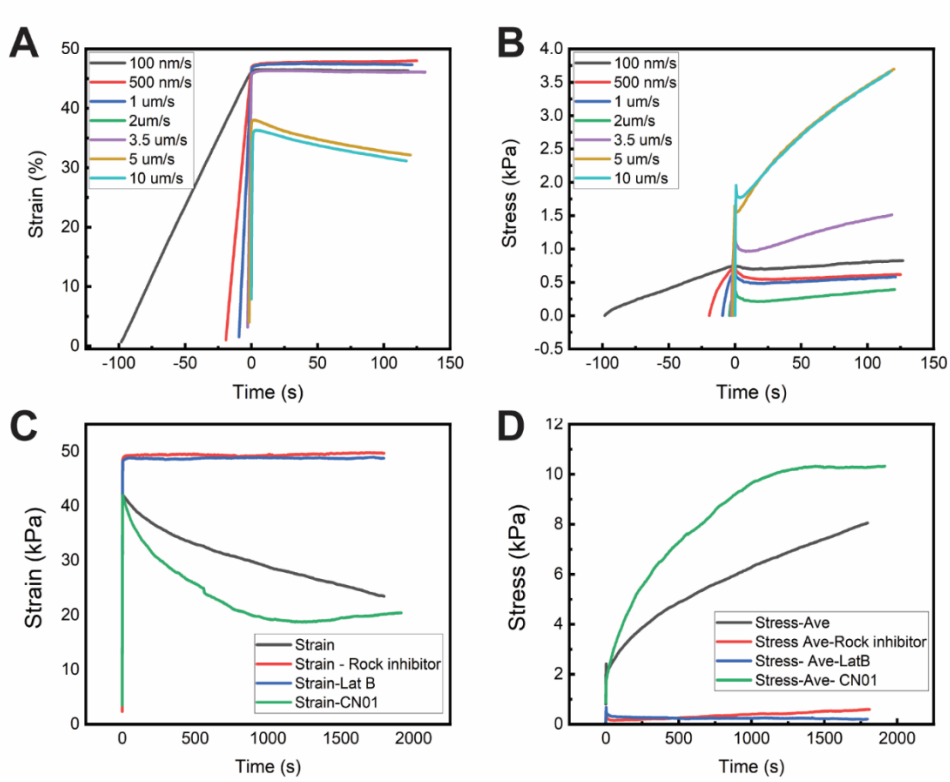

Figure 5.1. Active remodeling of the cytoskeleton. A) Strain changes during the stretch and hold for different strain rates. **B)** Stress changes during the stretch and hold experiment for different strain rates. **C)** Strain changes during the stretch and hold for different drugs. **D)** Strain changes during the stretch and hold for different drugs.

5.2. Characterization of IP-Visio microfibers

Nanoscribe company recently introduced a new material for their printers which has much less autofluorescent compared to IP-S. This material has the potential of being widely used in biological experiments. However, there is no document showing its mechanical properties. With our novel device, we printed microfibers of IP-Visio between the gap and stretched them. This experiment resembles the tensile test of steel but in micro-levels. Having the displacement of the sensor, we were able to characterize the mechanical

properties of the fibers from their stress-strain curves. The effect of printing parameters such as writing speed as well as geometry parameters such as width and depth of the beam have been analyzed. **Figure 5.2** shows a representative image and its corresponding plates' movement.

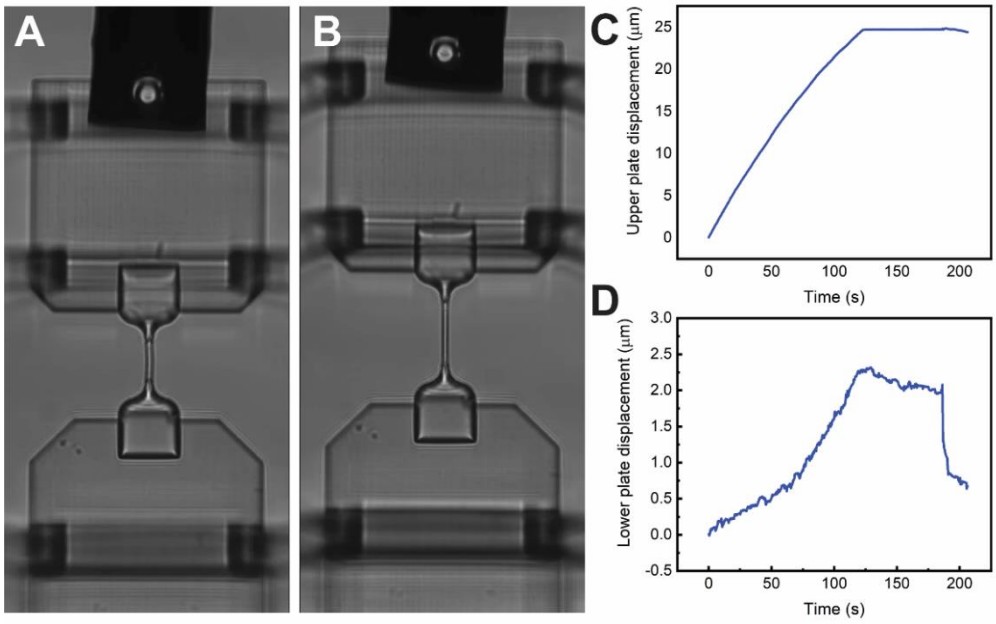

Figure 5.2. Mechanical characterization of microfibers. A) The first frame of the tensile test. **B)** The frame at the end of the tensile test. **C)** Upper plate displacement. **D)** Lower plate displacement.

5.3. PV screening of a single cell pair

We recently published a paper on the effect of mechanical stimulus on the life-threatening autoimmune blistering disease Pemphigus Vulgaris (PV). We showed that externally applied mechanical stress mitigates antibody-induced monolayer fragmentation and inhibits p38 MAPK phosphorylation activated by the anti-Dsg3 antibody. In this study, we used a monolayer of cells and stretched it in a PDMS cell culture chamber. Now we decided to apply the stress to a cell pair and try different anti-bodies to skin cells (HaCaT).

In this project, we are planning to run a stretch test until rupture, stretch and hold, AFM, and immunostaining at different conditions. **Figure 5.3** shows a representative curve from the stretch test. As it can be seen, the force level is much more than cancerous cells (A431).

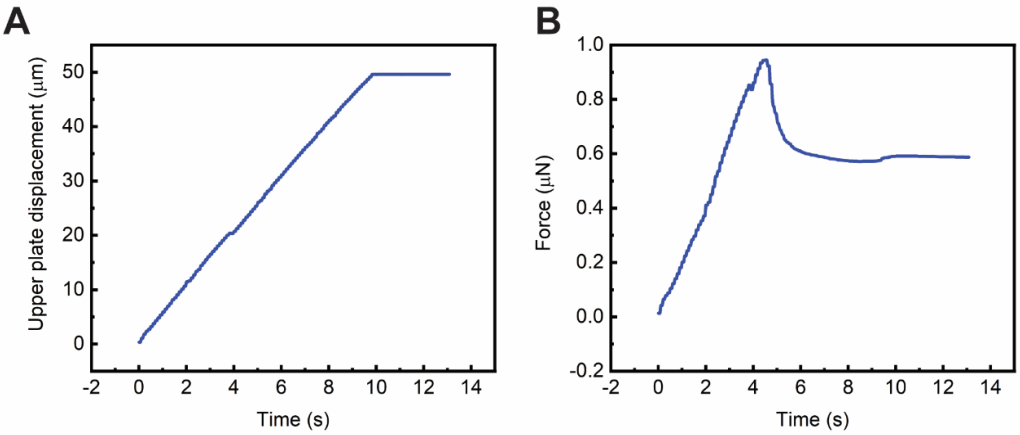

Figure 5.3. A representative curve from the stretch test of skin cells.

5.4. Desmoplakin mutation of the cell-cell junction

Desmoplakin is one of the proteins at the desmosome junction which plays an important role in maintaining the junction and keep the tissue integrity. In this experiment, we want to show this role quantitatively and at the cell level. The efficiency of the desmoplakin mutation is very low and we don't know whether the cells being stretched are muted or not. One way to make sure is to tag this protein with a color. With the current advances in the polymer for printing, we can detect the mutation and then run the stretch test. In this way, we will increase the efficiency and gather solid data. For this study, we will use A431 cells which are suppressed or overexpressed desmoplakin. The addition of doxycycline will induce the expression or mutation. **Figure 5.4** shows the effect of this induction on the cells.

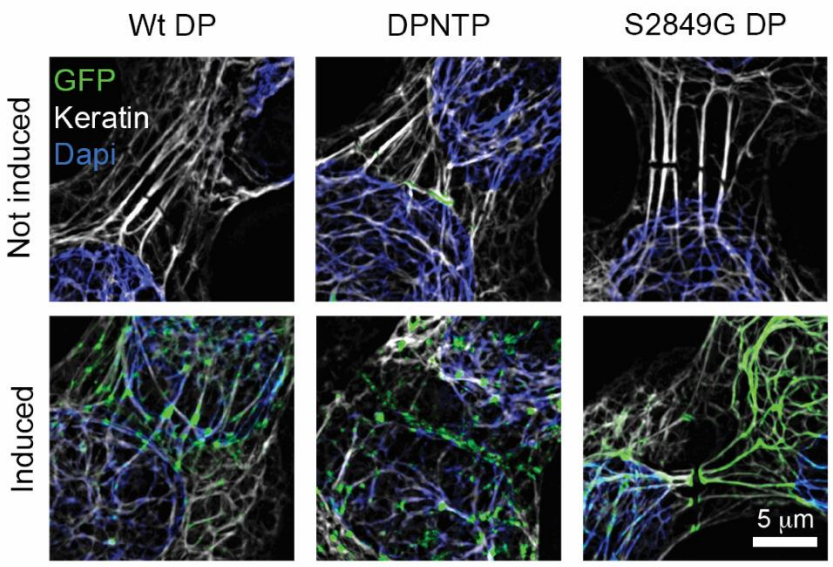

Figure 5.4. mutation and overexpression of desmoplakin in A431 cells (219)**.**

5.5. Traction force microscopy of the cell pair during the stretch test

During the stretch and hold experiments, we noticed that in addition to strengthening the junction and cytoskeleton, cells were anchoring more points to the substrate and trying to expand themselves. One way to measure these traction forces is by growing cells on an array of micropillars. So we modified our design in a way that we can measure the traction forces simultaneously with the adhesion forces. We added the array of pillars between the bowtie region and repeated the experiment. By tracking the pillars bending for each frame, we can correlate the stress-strain curve with the traction force. **Figure 5.5** shows the concept and fabricated design.

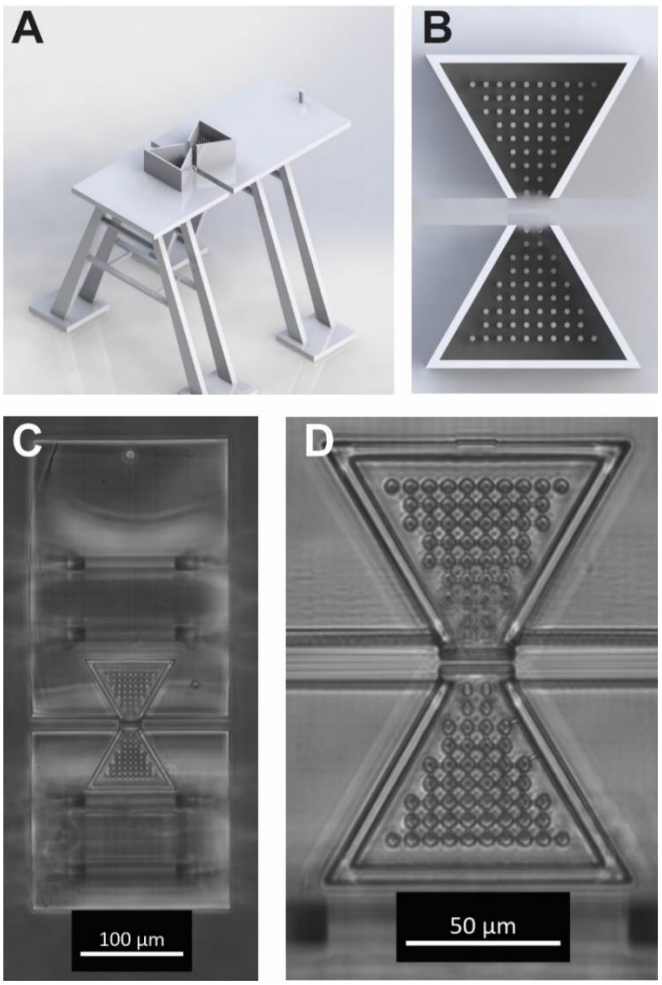

Figure 5.5. Traction force microscopy of the cell pair on the platform. A) Isometric view of the modified structure. **B)** Micropillars within the bowtie region. **C)** Top view of the fabricated structure. **D)** Micropillars within the bowtie

5.6. Application of FRET sensors to study the mechanotransduction pathway

The other application of the platform is to study the mechanotransduction pathway of cells subjected to external stress. To do this, we engineered FRET sensors to different proteins within the complex of cell junction and cytoskeleton.

REFERENCES

1. N. Wang, J. D. Tytell, D. E. Ingber, Mechanotransduction at a distance: mechanically coupling the extracellular matrix with the nucleus. *Nat. Rev. Mol. Cell Biol.* **10**, 75-82 (2009).
2. J. D. Humphrey, E. R. Dufresne, M. A. Schwartz, Mechanotransduction and extracellular matrix homeostasis. *Nat. Rev. Mol. Cell Biol.* **15**, 802-812 (2014).
3. T. J. Kirby, J. Lammerding, Cell mechanotransduction: Stretch to express. *Nat Mater* **15**, 1227-1229 (2016).
4. B. D. Riehl, J. H. Park, I. K. Kwon, J. Y. Lim, Mechanical stretching for tissue engineering: two-dimensional and three-dimensional constructs. *Tissue Eng Part B Rev* **18**, 288-300 (2012).
5. D. E. Ingber, Mechanical control of tissue morphogenesis during embryological development. *Int. J. Dev. Biol.* **50**, 255-266 (2006).
6. S. A. Gudipaty *et al.*, Mechanical stretch triggers rapid epithelial cell division through Piezo1. *Nature* **543**, 118-121 (2017).
7. H. Wolfenson, B. Yang, M. P. Sheetz, Steps in Mechanotransduction Pathways that Control Cell Morphology. *Annu Rev Physiol* **81**, 585-605 (2019).
8. B. Ladoux, W. J. Nelson, J. Yan, R. M. Mege, The mechanotransduction machinery at work at adherens junctions. *Integr. Biol. (Camb.)* **7**, 1109-1119 (2015).
9. W. Y. Wang, C. D. Davidson, D. Lin, B. M. Baker, Actomyosin contractility-dependent matrix stretch and recoil induces rapid cell migration. *Nat Commun* **10**, 1186 (2019).
10. G. Charras, A. S. Yap, Tensile Forces and Mechanotransduction at Cell-Cell Junctions. *Curr. Biol.* **28**, R445-R457 (2018).
11. J. M. Anderson, C. M. Van Itallie, Physiology and function of the tight junction. *Cold Spring Harb. Perspect. Biol.* **1**, a002584 (2009).
12. N. M. Kumar, N. B. Gilula, The gap junction communication channel. *Cell* **84**, 381-388 (1996).
13. N. J. Severs *et al.*, Gap junction alterations in human cardiac disease. *Cardiovasc. Res.* **62**, 368-377 (2004).
14. T. J. Harris, U. Tepass, Adherens junctions: from molecules to morphogenesis. *Nat. Rev. Mol. Cell Biol.* **11**, 502-514 (2010).
15. B. W. Benham-Pyle, B. L. Pruitt, W. J. Nelson, Cell adhesion. Mechanical strain induces E-cadherin-dependent Yap1 and beta-catenin activation to drive cell cycle entry. *Science* **348**, 1024-1027 (2015).
16. L. L. Witcher *et al.*, Desmosomal cadherin binding domains of plakoglobin. *J. Biol. Chem.* **271**, 10904-10909 (1996).
17. J. Waschke, The desmosome and pemphigus. *Histochem. Cell Biol.* **130**, 21-54 (2008).
18. H. J. Choi, W. I. Weis, Structure of the armadillo repeat domain of plakophilin 1. *J. Mol. Biol.* **346**, 367-376 (2005).
19. A. Monemian Esfahani *et al.*, Tissue Regeneration from Mechanical Stretching of Cell-Cell Adhesion. *Tissue Eng Part C Methods* 10.1089/ten.TEC.2019.0098 (2019).
20. J. L. Maitre, C. P. Heisenberg, Three functions of cadherins in cell adhesion. *Curr. Biol.* **23**, R626-633 (2013).
21. S. Yamada, W. J. Nelson, Localized zones of Rho and Rac activities drive initiation and expansion of epithelial cell-cell adhesion. *J. Cell Biol.* **178**, 517-527 (2007).
22. K. Manibog, H. Li, S. Rakshit, S. Sivasankar, Resolving the molecular mechanism of cadherin catch bond formation. *Nature Communications* **5** (2014).
23. W. A. Thomas *et al.*, alpha-Catenin and vinculin cooperate to promote high E-cadherin-based adhesion strength. *J. Biol. Chem.* **288**, 4957-4969 (2013).
24. M. Yao *et al.*, Force-dependent conformational switch of α-catenin controls vinculin binding. *Nature Communications* **5** (2014).

25. H. B. Jean-Léon Maître, 2,3 Simon Frederik Gabriel Krens,1 Guillaume Salbreux,2 Frank Jülicher,2 Ewa Paluch,4* Carl-Philipp Heisenberg, Adhesion Functions in Cell Sorting by Mechanically Coupling the Cortices of Adhering Cells. *Science* (2012).
26. N. Rohani, L. Canty, O. Luu, F. Fagotto, R. Winklbauer, EphrinB/EphB signaling controls embryonic germ layer separation by contact-induced cell detachment. *PLoS Biol.* **9**, e1000597 (2011).
27. E. Tabdanov, N. Borghi, F. Brochard-Wyart, S. Dufour, J. P. Thiery, Role of E-cadherin in membrane-cortex interaction probed by nanotube extrusion. *Biophys. J.* **96**, 2457-2465 (2009).
28. H. Wang, Y. Q. Huo, Adhesion Molecules and Atherosclerosis. *Atherosclerosis: Molecular and Cellular Mechanisms* Book_Doi 10.1002/9783527629589, 43-62 (2010).
29. K. Sundfeldt, Cell-cell adhesion in the normal ovary and ovarian tumors of epithelial origin; an exception to the rule. *Mol. Cell. Endocrinol.* **202**, 89-96 (2003).
30. E. Lozano, M. Betson, V. M. Braga, Tumor progression: Small GTPases and loss of cell-cell adhesion. *Bioessays* **25**, 452-463 (2003).
31. G. Berx *et al.*, E-cadherin is inactivated in a majority of invasive human lobular breast cancers by truncation mutations throughout its extracellular domain. *Oncogene* **13**, 1919-1925 (1996).
32. L. Ding *et al.*, Genome remodelling in a basal-like breast cancer metastasis and xenograft. *Nature* **464**, 999-1005 (2010).
33. N. A. Najor, Desmosomes in Human Disease. *Annu. Rev. Pathol.* **13**, 51-70 (2018).
34. C. Bierkamp, K. J. McLaughlin, H. Schwarz, O. Huber, R. Kemler, Embryonic heart and skin defects in mice lacking plakoglobin. *Dev. Biol.* **180**, 780-785 (1996).
35. J. E. Lai Cheong, V. Wessagowit, J. A. McGrath, Molecular abnormalities of the desmosomal protein desmoplakin in human disease. *Clin. Exp. Dermatol.* **30**, 261-266 (2005).
36. C. Buckley, J. Y. Tan, W. Weis, W. J. Nelson, A. Dunn, The Minimal Cadherin-Catenin Complex Binds to Actin Filaments under Force. *Biophys. J.* **108**, 11a-11a (2015).
37. J. Jurado, J. de Navascues, N. Gorfinkiel, alpha-Catenin stabilises Cadherin-Catenin complexes and modulates actomyosin dynamics to allow pulsatile apical contraction. *J. Cell Sci.* **129**, 4496-4508 (2016).
38. D. L. Huang, N. A. Bax, C. D. Buckley, W. I. Weis, A. R. Dunn, Vinculin forms a directionally asymmetric catch bond with F-actin. *Science* **357**, 703-706 (2017).
39. S. Rakshit, S. Sivasankar, Biomechanics of cell adhesion: how force regulates the lifetime of adhesive bonds at the single molecule level. *PCCP* **16**, 2211-2223 (2014).
40. C. Bertocchi *et al.*, Nanoscale architecture of cadherin-based cell adhesions. *Nat. Cell Biol.* **19**, 28-37 (2017).
41. J. L. Bays *et al.*, Vinculin phosphorylation differentially regulates mechanotransduction at cell-cell and cell-matrix adhesions. *J. Cell Biol.* **205**, 251-263 (2014).
42. J. L. Bays, H. K. Campbell, C. Heidema, M. Sebbagh, K. A. DeMali, Linking E-cadherin mechanotransduction to cell metabolism through force-mediated activation of AMPK. *Nat. Cell Biol.* **19**, 724-731 (2017).
43. Y. Kametani, M. Takeichi, Basal-to-apical cadherin flow at cell junctions. *Nat. Cell Biol.* **9**, 92-98 (2007).
44. R. Priya, A. S. Yap, G. A. Gomez, E-cadherin supports steady-state Rho signaling at the epithelial zonula adherens. *Differentiation* **86**, 133-140 (2013).
45. J. S. Bois, F. Julicher, S. W. Grill, Pattern formation in active fluids. *Phys. Rev. Lett.* **106**, 028103 (2011).
46. R. Priya *et al.*, Bistable front dynamics in a contractile medium: Travelling wave fronts and cortical advection define stable zones of RhoA signaling at epithelial adherens junctions. *PLoS Comput. Biol.* **13** (2017).
47. S. K. Wu *et al.*, Cortical F-actin stabilization generates apical-lateral patterns of junctional contractility that integrate cells into epithelia. *Nat. Cell Biol.* **16**, 167-178 (2014).

48. J. F. Joanny, J. Prost, Active gels as a description of the actin-myosin cytoskeleton. *Hfsp Journal* **3**, 94-104 (2009).
49. Y. Wu, P. Kanchanawong, R. Zaidel-Bar, Actin-delimited adhesion-independent clustering of E-cadherin forms the nanoscale building blocks of adherens junctions. *Dev. Cell* **32**, 139-154 (2015).
50. M. Smutny *et al.*, Myosin II isoforms identify distinct functional modules that support integrity of the epithelial zonula adherens. *Nat. Cell Biol.* **12**, 696-U147 (2010).
51. S. Verma *et al.*, A WAVE2-Arp2/3 actin nucleator apparatus supports junctional tension at the epithelial zonula adherens. *Mol. Biol. Cell* **23**, 4601-4610 (2012).
52. T. P. Wyatt *et al.*, Emergence of homeostatic epithelial packing and stress dissipation through divisions oriented along the long cell axis. *Proc. Natl. Acad. Sci. U. S. A.* **112**, 5726-5731 (2015).
53. A. R. Harris *et al.*, Characterizing the mechanics of cultured cell monolayers. *Proc. Natl. Acad. Sci. U. S. A.* **109**, 16449-16454 (2012).
54. K. C. Hart *et al.*, E-cadherin and LGN align epithelial cell divisions with tissue tension independently of cell shape. *Proc. Natl. Acad. Sci. U. S. A.* **114**, E5845-E5853 (2017).
55. C. Collinet, M. Rauzi, P. F. Lenne, T. Lecuit, Local and tissue-scale forces drive oriented junction growth during tissue extension. *Nat. Cell Biol.* **17**, 1247-+ (2015).
56. P. Campinho *et al.*, Tension-oriented cell divisions limit anisotropic tissue tension in epithelial spreading during zebrafish epiboly. *Nat. Cell Biol.* **15**, 1405-+ (2013).
57. E. Walck-Shannon, J. Hardin, Cell intercalation from top to bottom. *Nat. Rev. Mol. Cell Biol.* **15**, 34-48 (2014).
58. J. Prost, F. Julicher, J. F. Joanny, Active gel physics. *Nat. Phys.* **11**, 111-117 (2015).
59. N. Khalilgharibi, J. Fouchard, P. Recho, G. Charras, A. Kabla, The dynamic mechanical properties of cellularised aggregates. *Curr. Opin. Cell Biol.* **42**, 113-120 (2016).
60. X. Liang, M. Michael, G. A. Gomez, Measurement of Mechanical Tension at Cell-cell Junctions Using Two-photon Laser Ablation. *Bio-protocol* **6**, e2068 (2016).
61. D. T. Tambe *et al.*, Collective cell guidance by cooperative intercellular forces. *Nat Mater* **10**, 469-475 (2011).
62. J. N. Jodoin *et al.*, Stable Force Balance between Epithelial Cells Arises from F-Actin Turnover. *Dev. Cell* **35**, 685-697 (2015).
63. R. Clement, B. Dehapiot, C. Collinet, T. Lecuit, P. F. Lenne, Viscoelastic Dissipation Stabilizes Cell Shape Changes during Tissue Morphogenesis. *Curr. Biol.* **27**, 3132-+ (2017).
64. T. Wyatt, B. Baum, G. Charras, A question of time: tissue adaptation to mechanical forces. *Curr. Opin. Cell Biol.* **38**, 68-73 (2016).
65. M. Fritzsche, A. Lewalle, T. Duke, K. Kruse, G. Charras, Analysis of turnover dynamics of the submembranous actin cortex. *Mol. Biol. Cell* **24**, 757-767 (2013).
66. T. Onodera *et al.*, Btbd7 Regulates Epithelial Cell Dynamics and Branching Morphogenesis. *Science* **329**, 562-565 (2010).
67. T. Sakai, M. Larsen, K. M. Yamada, Fibronectin requirement in branching morphogenesis. *Nature* **423**, 876-881 (2003).
68. Y. Izu *et al.*, Type XII collagen regulates osteoblast polarity and communication during bone formation. *J. Cell Biol.* **193**, 1115-1130 (2011).
69. A. Al-Kilani, O. de Freitas, S. Dufour, F. Gallet, Negative Feedback from Integrins to Cadherins: A Micromechanical Study. *Biophys. J.* **101**, 336-344 (2011).
70. N. Borghi, M. Lowndes, V. Maruthamuthu, M. L. Gardel, W. J. Nelson, Regulation of cell motile behavior by crosstalk between cadherin- and integrin-mediated adhesions. *Proc. Natl. Acad. Sci. U. S. A.* **107**, 13324-13329 (2010).
71. M. L. McCain, H. Lee, Y. Aratyn-Schaus, A. G. Kleber, K. K. Parker, Cooperative coupling of cell-matrix and cell-cell adhesions in cardiac muscle. *Proc. Natl. Acad. Sci. U. S. A.* **109**, 9881-9886 (2012).

72. M. von Schlippe *et al.*, Functional interaction between E-cadherin and alpha v-containing integrins in carcinoma cells. *J. Cell Sci.* **113**, 425-437 (2000).
73. G. Livshits, A. Kobielak, E. Fuchs, Governing epidermal homeostasis by coupling cell-cell adhesion to integrin and growth factor signaling, proliferation, and apoptosis. *Proc. Natl. Acad. Sci. U. S. A.* **109**, 4886-4891 (2012).
74. J. T. Parsons, A. R. Horwitz, M. A. Schwartz, Cell adhesion: integrating cytoskeletal dynamics and cellular tension. *Nat. Rev. Mol. Cell Biol.* **11**, 633-643 (2010).
75. K. L. Mui, C. S. Chen, R. K. Assoian, The mechanical regulation of integrin-cadherin crosstalk organizes cells, signaling and forces. *J. Cell Sci.* **129**, 1093-1100 (2016).
76. N. Borghi *et al.*, E-cadherin is under constitutive actomyosin-generated tension that is increased at cell-cell contacts upon externally applied stretch. *Proc. Natl. Acad. Sci. U. S. A.* **109**, 12568-12573 (2012).
77. B. W. Benham-Pyle, B. L. Pruitt, W. J. Nelson, Mechanical strain induces E-cadherin–dependent Yap1 and β-catenin activation to drive cell cycle entry. *Science* **348**, 1024-1027 (2015).
78. Y. X. Wang *et al.*, Integrins regulate VE-cadherin and catenins: Dependence of this regulation on Src,, but not on Ras. *Proc. Natl. Acad. Sci. U. S. A.* **103**, 1774-1779 (2006).
79. L. A. Barnes *et al.*, Mechanical Forces in Cutaneous Wound Healing: Emerging Therapies to Minimize Scar Formation. *Adv Wound Care (New Rochelle)* **7**, 47-56 (2018).
80. M. Chiquet, V. Tunc-Civelek, A. Sarasa-Renedo, Gene regulation by mechanotransduction in fibroblasts. *Appl. Physiol. Nutr. Metab.* **32**, 967-973 (2007).
81. B. Eckes *et al.*, Mechanical tension and integrin alpha 2 beta 1 regulate fibroblast functions. *J. Investig. Dermatol. Symp. Proc.* **11**, 66-72 (2006).
82. R. Agha, R. Ogawa, G. Pietramaggiori, D. P. Orgill, A review of the role of mechanical forces in cutaneous wound healing. *J. Surg. Res.* **171**, 700-708 (2011).
83. H. S. Yu, J. J. Kim, H. W. Kim, M. P. Lewis, I. Wall, Impact of mechanical stretch on the cell behaviors of bone and surrounding tissues. *J Tissue Eng* **7**, 2041731415618342 (2016).
84. T. Zulueta-Coarasa, R. Fernandez-Gonzalez, Tension (re)builds: Biophysical mechanisms of embryonic wound repair. *Mech. Dev.* **144**, 43-52 (2017).
85. L. I. Plotkin *et al.*, Mechanical stimulation prevents osteocyte apoptosis: requirement of integrins, Src kinases, and ERKs. *Am J Physiol-Cell Ph* **289**, C633-C643 (2005).
86. N. Boutahar, A. Guignandon, L. Vico, M. H. Lafage-Proust, Mechanical strain on osteoblasts activates autophosphorylation of focal adhesion kinase and proline-rich tyrosine kinase 2 tyrosine sites involved in ERK activation. *J. Biol. Chem.* **279**, 30588-30599 (2004).
87. M. A. Razzak *et al.*, Cellular and Molecular Responses to Mechanical Expansion of Tissue. *Front. Physiol.* **7** (2016).
88. C. Huang *et al.*, Talin phosphorylation by Cdk5 regulates Smurf1-mediated talin head ubiquitylation and cell migration. *Nat. Cell Biol.* **11**, 624-U404 (2009).
89. C. M. Laukaitis, D. J. Webb, K. Donais, A. F. Horwitz, Differential dynamics of alpha 5 integrin, paxillin, and alpha-actinin during formation and disassembly of adhesions in migrating cells. *J. Cell Biol.* **153**, 1427-1440 (2001).
90. D. L. Butler *et al.*, The Impact of Biomechanics in Tissue Engineering and Regenerative Medicine. *Tissue Eng Part B-Re* **15**, 477-484 (2009).
91. V. F. Shimko, W. C. Claycomb, Effect of mechanical loading on three-dimensional cultures of embryonic stem cell-derived cardiomyocytes. *Tissue Eng Pt A* **14**, 49-58 (2008).
92. C. A. Powell, B. L. Smiley, J. Mills, H. H. Vandenburgh, Mechanical stimulation improves tissue-engineered human skeletal muscle. *Am J Physiol-Cell Ph* **283**, C1557-C1565 (2002).
93. K. C. Clause, J. P. Tinney, L. J. Liu, B. B. Keller, K. Tobita, Engineered Early Embryonic Cardiac Tissue Increases Cardiomyocyte Proliferation by Cyclic Mechanical Stretch via p38-MAP Kinase Phosphorylation. *Tissue Eng Pt A* **15**, 1373-1380 (2009).

94. K. Bilodeau, F. Couet, F. Boccafoschi, D. Mantovani, Design of a perfusion bioreactor specific to the regeneration of vascular tissues under mechanical stresses. *Artif. Organs* **29**, 906-912 (2005).
95. J. Lammerding, R. D. Kamm, R. T. Lee, Mechanotransduction in cardiac myocytes. *Cardiac Engineering: From Genes and Cells to Structure and Function* **1015**, 53-70 (2004).
96. J. S. Park *et al.*, Differential effects of equiaxial and uniaxial strain on mesenchymal stem cells. *Biotechnol Bioeng* **88**, 359-368 (2004).
97. G. H. Altman *et al.*, Cell differentiation by mechanical stress. *FASEB J.* **15**, 270-+ (2001).
98. Y. L. Fan, H. C. Zhao, B. Li, Z. L. Zhao, X. Q. Feng, Mechanical Roles of F-Actin in the Differentiation of Stem Cells: A Review. *Acs Biomaterials Science & Engineering* **5**, 3788-3801 (2019).
99. C. H. Huang, M. H. Chen, T. H. Young, J. H. Jeng, Y. J. Chen, Interactive Effects of Mechanical Stretching and Extracellular Matrix Proteins on Initiating Osteogenic Differentiation of Human Mesenchymal Stem Cells. *J. Cell. Biochem.* **108**, 1263-1273 (2009).
100. B. Y. Xu *et al.*, RhoA/ROCK, cytoskeletal dynamics, and focal adhesion kinase are required for mechanical stretch-induced tenogenic differentiation of human mesenchymal stem cells. *J. Cell. Physiol.* **227**, 2722-2729 (2012).
101. G. Song, Y. Ju, H. Soyama, T. Ohashi, M. Sato, Regulation of cyclic longitudinal mechanical stretch on proliferation of human bone marrow mesenchymal stem cells. *Mol. Cell. Biomech.* **4**, 201-210 (2007).
102. B. Zhang *et al.*, Cyclic mechanical stretching promotes migration but inhibits invasion of rat bone marrow stromal cells. *Stem Cell Res* **14**, 155-164 (2015).
103. X. Liang, X. Huang, Y. Zhou, R. Jin, Q. Li, Mechanical Stretching Promotes Skin Tissue Regeneration via Enhancing Mesenchymal Stem Cell Homing and Transdifferentiation. *Stem Cells Transl Med* **5**, 960-969 (2016).
104. I. Owan *et al.*, Mechanotransduction in bone: osteoblasts are more responsive to fluid forces than mechanical strain. *Am J Physiol* **273**, C810-815 (1997).
105. Y. Han, S. C. Cowin, M. B. Schaffler, S. Weinbaum, Mechanotransduction and strain amplification in osteocyte cell processes. *Proc. Natl. Acad. Sci. U. S. A.* **101**, 16689-16694 (2004).
106. S. W. Verbruggen, T. J. Vaughan, L. M. McNamara, Strain amplification in bone mechanobiology: a computational investigation of the in vivo mechanics of osteocytes. *Journal of the Royal Society Interface* **9**, 2735-2744 (2012).
107. F. Assanah, Y. Khan, Cell responses to physical forces, and how they inform the design of tissue-engineered constructs for bone repair: a review. *J. Mater. Sci.* **53**, 5618-5640 (2018).
108. D. P. Pioletti, J. Muller, L. R. Rakotomanana, J. Corbeil, E. Wild, Effect of micromechanical stimulations on osteoblasts: development of a device simulating the mechanical situation at the bone-implant interface. *J. Biomech.* **36**, 131-135 (2003).
109. X. Trepat *et al.*, Viscoelasticity of human alveolar epithelial cells subjected to stretch. *American Journal of Physiology-Lung Cellular and Molecular Physiology* **287**, L1025-L1034 (2004).
110. B. J. Pfister, T. P. Weihs, M. Betenbaugh, G. Bao, An in vitro uniaxial stretch model for axonal injury. *Annals of biomedical engineering* **31**, 589-598 (2003).
111. H. Wang, W. Ip, R. Boissy, E. S. Grood, Cell orientation response to cyclically deformed substrates: experimental validation of a cell model. *Journal of biomechanics* **28**, 1543-1552 (1995).
112. C. Hung, J. Williams, A method for inducing equi-biaxial and uniform strains in elastomeric membranes used as cell substrates. *Journal of biomechanics* **27**, 227-232 (1994).
113. J. L. Schaffer *et al.*, Device for the application of a dynamic biaxially uniform and isotropic strain to a flexible cell culture membrane. *J. Orthop. Res.* **12**, 709-719 (1994).

114. D. Somjen, I. Binderman, E. Berger, A. Harell, Bone remodelling induced by physical stress is prostaglandin E2 mediated. *Biochimica et Biophysica Acta (BBA)-General Subjects* **627**, 91-100 (1980).
115. G. Jin, G. H. Yang, G. Kim, Tissue engineering bioreactor systems for applying physical and electrical stimulations to cells. *J Biomed Mater Res B* **103**, 935-948 (2015).
116. C. P. Ursekar *et al.*, Design and construction of an equibiaxial cell stretching system that is improved for biochemical analysis. *PLoS One* **9**, e90665 (2014).
117. R. Yang, J. A. Broussard, K. J. Green, H. D. Espinosa, Techniques to stimulate and interrogate cell-cell adhesion mechanics. *Extreme Mechanics Letters* (2017).
118. M. Bottlang, M. Simnacher, H. Schmitt, R. Brand, L. Claes, A Cell Strain System for Small Homogeneous Strain Applications-Ein Zellstimulations-System zur Applikation kleiner homogener Dehnungen. *Biomedizinische Technik/Biomedical Engineering* **42**, 305-309 (1997).
119. J. Williams, J. Chen, D. Belloli, Strain fields on cell stressing devices employing clamped circular elastic diaphragms as substrates. *J. Biomech. Eng.* **114**, 377-384 (1992).
120. P. McMillen, S. A. Holley, Integration of cell-cell and cell-ECM adhesion in vertebrate morphogenesis. *Curr. Opin. Cell Biol.* **36**, 48-53 (2015).
121. K. Goodwin *et al.*, Cell-cell and cell-extracellular matrix adhesions cooperate to organize actomyosin networks and maintain force transmission during dorsal closure. *Mol. Biol. Cell* **28**, 1301-1310 (2017).
122. R. Yang, J. A. Broussard, K. J. Green, H. D. Espinosa, Techniques to Stimulate and Interrogate Cell-Cell Adhesion Mechanics. *Extreme Mechanics Letters* **In Press** (2017).
123. M. Levesque, R. Nerem, E. Sprague, Vascular endottielial cell proliferation in culture and the influence of flow. *Biomaterials* **11**, 702-707 (1990).
124. C. Dong, X. X. Lei, Biomechanics of cell rolling: shear flow, cell-surface adhesion, and cell deformability. *Journal of biomechanics* **33**, 35-43 (2000).
125. T.-H. Chun *et al.*, Shear stress augments expression of C-type natriuretic peptide and adrenomedullin. *Hypertension* **29**, 1296-1302 (1997).
126. T. G. Diacovo *et al.*, Interactions of human alpha/beta and gamma/delta T lymphocyte subsets in shear flow with E-selectin and P-selectin. *J. Exp. Med.* **183**, 1193-1203 (1996).
127. J. Frangos, L. McIntire, S. Eskin, Shear stress induced stimulation of mammalian cell metabolism. *Biotechnology and bioengineering* **32**, 1053-1060 (1988).
128. C. T. Hung, S. R. Pollack, T. M. Reilly, C. T. Brighton, Real-time calcium response of cultured bone cells to fluid flow. *Clin. Orthop. Relat. Res.* **313**, 256-269 (1995).
129. P. Kuijper *et al.*, Platelet-dependent primary hemostasis promotes selectin-and integrin-mediated neutrophil adhesion to damaged endothelium under flow conditions. *Blood* **87**, 3271-3281 (1996).
130. M. Levesque, R. Nerem, The elongation and orientation of cultured endothelial cells in response to shear stress. *J. Biomech. Eng.* **107**, 341-347 (1985).
131. H. Tseng, T. E. Peterson, B. C. Berk, Fluid shear stress stimulates mitogen-activated protein kinase in endothelial cells. *Circ. Res.* **77**, 869-878 (1995).
132. J. W. Song *et al.*, Computer-controlled microcirculatory support system for endothelial cell culture and shearing. *Analytical chemistry* **77**, 3993-3999 (2005).
133. E. Tkachenko, E. Gutierrez, M. H. Ginsberg, A. Groisman, An easy to assemble microfluidic perfusion device with a magnetic clamp. *Lab on a Chip* **9**, 1085-1095 (2009).
134. E. W. Young, A. R. Wheeler, C. A. Simmons, Matrix-dependent adhesion of vascular and valvular endothelial cells in microfluidic channels. *Lab on a Chip* **7**, 1759-1766 (2007).
135. H. Lu *et al.*, Microfluidic shear devices for quantitative analysis of cell adhesion. *Analytical chemistry* **76**, 5257-5264 (2004).
136. C. Dewey Jr, Effects of fluid flow on living vascular cells. *J. Biomech. Eng.* **106**, 31-35 (1984).

137. K. S. Furukawa *et al.*, Quantitative analysis of cell detachment by shear stress. *Materials Science and Engineering: C* **17**, 55-58 (2001).
138. C. Hermann, A. M. Zeiher, S. Dimmeler, Shear stress inhibits H2O2-induced apoptosis of human endothelial cells by modulation of the glutathione redox cycle and nitric oxide synthase. *Arteriosclerosis, thrombosis, and vascular biology* **17**, 3588-3592 (1997).
139. M. Mohtai *et al.*, Expression of interleukin-6 in osteoarthritic chondrocytes and effects of fluid-induced shear on this expression in normal human chondrocytes in vitro. *J. Orthop. Res.* **14**, 67-73 (1996).
140. A. v. van Grondelle *et al.*, Altering hydrodynamic variables influences PGI2 production by isolated lungs and endothelial cells. *J. Appl. Physiol.* **57**, 388-395 (1984).
141. M. Dembo, Y. L. Wang, Stresses at the cell-to-substrate interface during locomotion of fibroblasts. *Biophysical Journal* **76**, 2307-2316 (1999).
142. J. L. Martiel *et al.*, Measurement of cell traction forces with ImageJ. *Method Cell Biol* **125**, 269-287 (2015).
143. Q. Tseng *et al.*, Spatial organization of the extracellular matrix regulates cell-cell junction positioning. *Proc. Natl. Acad. Sci. U. S. A.* **109**, 1506-1511 (2012).
144. S. J. Han, Y. Oak, A. Groisman, G. Danuser, Traction microscopy to identify force modulation in subresolution adhesions. *Nat Methods* **12**, 653-656 (2015).
145. Anonymous, (!!! INVALID CITATION !!! {}).
146. C. Franck, S. A. Maskarinec, D. A. Tirrell, G. Ravichandran, Three-dimensional traction force microscopy: a new tool for quantifying cell-matrix interactions. *PLoS One* **6**, e17833 (2011).
147. W. R. Legant *et al.*, Measurement of mechanical tractions exerted by cells in three-dimensional matrices. *Nature Methods* **7**, 969-U113 (2010).
148. J. Steinwachs *et al.*, Three-dimensional force microscopy of cells in biopolymer networks. *Nat Methods* **13**, 171-176 (2016).
149. A. F. Mertz *et al.*, Cadherin-based intercellular adhesions organize epithelial cell-matrix traction forces. *Proc Natl Acad Sci U S A* **110**, 842-847 (2013).
150. C. A. Reinhart-King, M. Dembo, D. A. Hammer, Cell-Cell Mechanical Communication through Compliant Substrates. *Biophysical Journal* **95**, 6044-6051 (2008).
151. J. Y. Sim *et al.*, Spatial distribution of cell-cell and cell-ECM adhesions regulates force balance while maintaining E-cadherin molecular tension in cell pairs. *Mol Biol Cell* **26**, 2456-2465 (2015).
152. C. Martinez-Rico, F. Pincet, J. P. Thiery, S. Dufour, Integrins stimulate E-cadherin-mediated intercellular adhesion by regulating Src-kinase activation and actomyosin contractility. *J Cell Sci* **123**, 712-722 (2010).
153. G. F. Weber, M. A. Bjerke, D. W. DeSimone, Integrins and cadherins join forces to form adhesive networks. *J Cell Sci* **124**, 1183-1193 (2011).
154. V. Maruthamuthu, B. Sabass, U. S. Schwarz, M. L. Gardel, Cell-ECM traction force modulates endogenous tension at cell-cell contacts. *Proc. Natl. Acad. Sci. U. S. A.* **108**, 4708-4713 (2011).
155. J. Y. Sim *et al.*, Spatial distribution of cell–cell and cell–ECM adhesions regulates force balance while maintaining E-cadherin molecular tension in cell pairs. *Mol Biol Cell* **26**, 2456-2465 (2015).
156. J. L. Tan *et al.*, Cells lying on a bed of microneedles: an approach to isolate mechanical force. *Proceedings of the National Academy of Sciences* **100**, 1484-1489 (2003).
157. N. J. Sniadecki *et al.*, Magnetic microposts as an approach to apply forces to living cells. *Proceedings of the National Academy of Sciences* **104**, 14553-14558 (2007).
158. R. Rand, A. Burton, Mechanical properties of the red cell membrane: I. Membrane stiffness and intracellular pressure. *Biophys. J.* **4**, 115-135 (1964).

159. R. M. Hochmuth, Micropipette aspiration of living cells. *Journal of biomechanics* **33**, 15-22 (2000).
160. R. Hochmuth, H. Ting-Beall, B. Beaty, D. Needham, R. Tran-Son-Tay, Viscosity of passive human neutrophils undergoing small deformations. *Biophys. J.* **64**, 1596-1601 (1993).
161. M. Sato, M. J. Levesque, R. M. Nerem, Micropipette aspiration of cultured bovine aortic endothelial cells exposed to shear stress. *Arteriosclerosis, thrombosis, and vascular biology* **7**, 276-286 (1987).
162. T. Secomb, Red blood cell mechanics and capillary blood rheology. *Cell Biochem. Biophys.* **18**, 231-251 (1991).
163. T. Secomb, R. Hsu, Red blood cell mechanics and functional capillary density. *International Journal of Microcirculation* **15**, 250-254 (1995).
164. J. Wu, W. Herzog, M. Epstein, Modelling of location-and time-dependent deformation of chondrocytes during cartilage loading. *Journal of biomechanics* **32**, 563-572 (1999).
165. K.-L. P. Sung, L. A. Sung, M. Crimmins, S. J. Burakoff, S. Chien, Determination of junction avidity of cytolytic T cell and target cell. *Science* **234**, 1405-1409 (1986).
166. K. P. Sung, E. Saldivar, L. Phillips, Interleukin-1β induces differential adhesiveness on human endothelial cell surfaces. *Biochemical and biophysical research communications* **202**, 866-872 (1994).
167. H. Miyazaki, Y. Hasegawa, K. Hayashi, A newly designed tensile tester for cells and its application to fibroblasts. *Journal of biomechanics* **33**, 97-104 (2000).
168. K. Nagayama, S. Yanagihara, T. Matsumoto, A novel micro tensile tester with feed-back control for viscoelastic analysis of single isolated smooth muscle cells. *Med. Eng. Phys.* **29**, 620-628 (2007).
169. A. Ashkin, J. M. Dziedzic, Optical trapping and manipulation of viruses and bacteria. *Science* **235**, 1517-1521 (1987).
170. A. D. Mehta, M. Rief, J. A. Spudich, D. A. Smith, R. M. Simmons, Single-molecule biomechanics with optical methods. *Science* **283**, 1689-1695 (1999).
171. J.-D. Wen *et al.*, Force unfolding kinetics of RNA using optical tweezers. I. Effects of experimental variables on measured results. *Biophys. J.* **92**, 2996-3009 (2007).
172. M. Dao, C. T. Lim, S. Suresh, Mechanics of the human red blood cell deformed by optical tweezers. *Journal of the Mechanics and Physics of Solids* **51**, 2259-2280 (2003).
173. J. Mills, L. Qie, M. Dao, C. Lim, S. Suresh, Nonlinear elastic and viscoelastic deformation of the human red blood cell with optical tweezers. *MCB-TECH SCIENCE PRESS*- **1**, 169-180 (2004).
174. K. Svoboda, S. M. Block, Biological applications of optical forces. *Annual review of biophysics and biomolecular structure* **23**, 247-285 (1994).
175. J. Sleep, D. Wilson, R. Simmons, W. Gratzer, Elasticity of the red cell membrane and its relation to hemolytic disorders: an optical tweezers study. *Biophys. J.* **77**, 3085-3095 (1999).
176. J. Mills *et al.*, Effect of plasmodial RESA protein on deformability of human red blood cells harboring Plasmodium falciparum. *Proceedings of the National Academy of Sciences* **104**, 9213-9217 (2007).
177. S. Suresh *et al.*, Reprint of: connections between single-cell biomechanics and human disease states: gastrointestinal cancer and malaria. *Acta biomaterialia* **23**, S3-S15 (2015).
178. J. Guck, R. Ananthakrishnan, C. C. Cunningham, J. Käs, Stretching biological cells with light. *J. Phys.: Condens. Matter* **14**, 4843 (2002).
179. J. Guck *et al.*, The optical stretcher: a novel laser tool to micromanipulate cells. *Biophys. J.* **81**, 767-784 (2001).
180. J. Guck, J. Chiang, J. Kas (1998) The optical stretcher ua novel tool to characterize the cytoskeleton. in *Molecular Biology of the Cell* (AMER SOC CELL BIOLOGY PUBL OFFICE, 9650 ROCKVILLE PIKE, BETHESDA, MD 20814 USA), pp 105A-105A.

181. F. Crick, A. Hughes, The physical properties of cytoplasm: A study by means of the magnetic particle method Part I. Experimental. *Exp. Cell Res.* **1**, 37-80 (1950).
182. G. N. Maksym *et al.*, Mechanical properties of cultured human airway smooth muscle cells from 0.05 to 0.4 Hz. *J. Appl. Physiol.* **89**, 1619-1632 (2000).
183. M. Puig-De-Morales *et al.*, Measurement of cell microrheology by magnetic twisting cytometry with frequency domain demodulation. *J. Appl. Physiol.* **91**, 1152-1159 (2001).
184. B. Fabry, G. N. Maksym, R. D. Hubmayr, J. P. Butler, J. J. Fredberg, Implications of heterogeneous bead behavior on cell mechanical properties measured with magnetic twisting cytometry. *Journal of magnetism and magnetic materials* **194**, 120-125 (1999).
185. Y. Tseng, T. P. Kole, D. Wirtz, Micromechanical mapping of live cells by multiple-particle-tracking microrheology. *Biophys. J.* **83**, 3162-3176 (2002).
186. G. Charras, P. P. Lehenkari, M. Horton, Atomic force microscopy can be used to mechanically stimulate osteoblasts and evaluate cellular strain distributions. *Ultramicroscopy* **86**, 85-95 (2001).
187. M. Radmacher, 4.-Measuring the Elastic Properties of Living Cells by the Atomic Force Microscope. *Methods Cell Biol.* **68**, 67-90 (2002).
188. R. Mahaffy, S. Park, E. Gerde, J. Käs, C. Shih, Quantitative analysis of the viscoelastic properties of thin regions of fibroblasts using atomic force microscopy. *Biophys. J.* **86**, 1777-1793 (2004).
189. A. Vaziri, H. Lee, M. K. Mofrad, Deformation of the cell nucleus under indentation: mechanics and mechanisms. *J. Mater. Res.* **21**, 2126-2135 (2006).
190. M. Benoit, 5.-Cell Adhesion Measured by Force Spectroscopy on Living Cells. *Methods Cell Biol.* **68**, 91-114 (2002).
191. P. Hinterdorfer, 6.-Molecular Recognition Studies Using the Atomic Force Microscope. *Methods Cell Biol.* **68**, 115-141 (2002).
192. O. H. Willemsen *et al.*, Biomolecular interactions measured by atomic force microscopy. *Biophys. J.* **79**, 3267-3281 (2000).
193. B. T. Marshall, M. Long, J. W. Piper, T. Yago, Direct observation of catch bonds involving cell-adhesion molecules. *Nature* **423**, 190 (2003).
194. M. Benoit, D. Gabriel, G. Gerisch, H. E. Gaub, Discrete interactions in cell adhesion measured by single-molecule force spectroscopy. *Nat Cell Biol* **2**, 313-317 (2000).
195. J. Friedrichs *et al.*, A practical guide to quantify cell adhesion using single-cell force spectroscopy. *Methods* **60**, 169-178 (2013).
196. P. H. Puech, K. Poole, D. Knebel, D. J. Muller, A new technical approach to quantify cell-cell adhesion forces by AFM. *Ultramicroscopy* **106**, 637-644 (2006).
197. M. Krieg *et al.*, Tensile forces govern germ-layer organization in zebrafish. *Nature Cell Biology* **10**, 429-U122 (2008).
198. A. Heisterkamp *et al.*, Pulse energy dependence of subcellular dissection by femtosecond laser pulses. *Opt Express* **13**, 3690-3696 (2005).
199. S. Kumar *et al.*, Viscoelastic retraction of single living stress fibers and its impact on cell shape, cytoskeletal organization, and extracellular matrix mechanics. *Biophys J* **90**, 3762-3773 (2006).
200. A. Brugues *et al.*, Forces driving epithelial wound healing. *Nat Phys* **10**, 683-690 (2014).
201. R. Yang *et al.*, Cellular level robotic surgery: Nanodissection of intermediate filaments in live keratinocytes. *Nanomedicine: Nanotechnology, Biology and Medicine* **11**, 137-145 (2015).
202. K. Seiffert-Sinha *et al.*, Nanorobotic investigation identifies novel visual, structural and functional correlates of autoimmune pathology in a blistering skin disease model. *PLoS One* **9**, e106895 (2014).
203. S. Yang, T. Saif, Reversible and repeatable linear local cell force response under large stretches. *Exp. Cell Res.* **305**, 42-50 (2005).

204. J. Rajagopalan, A. Tofangchi, M. T. A. Saif, Linear high-resolution bioMEMS force sensors with large measurement range. *Journal of Microelectromechanical Systems* **19**, 1380-1389 (2010).
205. S. Eppell, B. Smith, H. Kahn, R. Ballarini, Nano measurements with micro-devices: mechanical properties of hydrated collagen fibrils. *Journal of the Royal Society Interface* **3**, 117-121 (2006).
206. N. Scuor *et al.*, Design of a novel MEMS platform for the biaxial stimulation of living cells. *Biomed. Microdevices* **8**, 239-246 (2006).
207. A. M. Greiner, B. Richter, M. Bastmeyer, Micro-engineered 3D scaffolds for cell culture studies. *Macromol. Biosci.* **12**, 1301-1314 (2012).
208. A. M. Greiner *et al.*, Multifunctional polymer scaffolds with adjustable pore size and chemoattractant gradients for studying cell matrix invasion. *Biomaterials* **35**, 611-619 (2014).
209. F. Klein *et al.*, Two-component polymer scaffolds for controlled three-dimensional cell culture. *Adv Mater* **23**, 1341-1345 (2011).
210. B. Richter *et al.*, Guiding Cell Attachment in 3D Microscaffolds Selectively Functionalized with Two Distinct Adhesion Proteins. *Adv Mater* **29** (2017).
211. B. Richter *et al.*, Three-dimensional microscaffolds exhibiting spatially resolved surface chemistry. *Adv Mater* **25**, 6117-6122 (2013).
212. F. Klein *et al.*, Elastic fully three-dimensional microstructure scaffolds for cell force measurements. *Adv Mater* **22**, 868-871 (2010).
213. A. C. Scheiwe, S. C. Frank, T. J. Autenrieth, M. Bastmeyer, M. Wegener, Subcellular stretch-induced cytoskeletal response of single fibroblasts within 3D designer scaffolds. *Biomaterials* **44**, 186-194 (2015).
214. W. R. Legant *et al.*, Multidimensional traction force microscopy reveals out-of-plane rotational moments about focal adhesions. *P Natl Acad Sci USA* **110**, 881-886 (2013).
215. Z. J. Liu *et al.*, Mechanical tugging force regulates the size of cell-cell junctions. *Proceedings of the National Academy of Sciences of the United States of America* **107**, 9944-9949 (2010).
216. F. Klein *et al.*, Elastic Fully Three-dimensional Microstructure Scaffolds for Cell Force Measurements. *Advanced Materials* **22**, 868-+ (2010).
217. R. Kaunas, P. Nguyen, S. Usami, S. Chien, Cooperative effects of Rho and mechanical stretch on stress fiber organization. *Proceedings of the National Academy of Sciences of the United States of America* **102**, 15895-15900 (2005).
218. R. Yang, J. A. Broussard, K. J. Green, H. D. Espinosa, Techniques to stimulate and interrogate cell-cell adhesion mechanics. *Extreme Mech Lett* **20**, 125-139 (2018).
219. J. A. Broussard *et al.*, The desmoplakin/intermediate filament linkage regulates cell mechanics. *Mol. Biol. Cell*, mbc. E16-07-0520 (2017).
220. Z. Liu *et al.*, Mechanical tugging force regulates the size of cell-cell junctions. *Proc. Natl. Acad. Sci. U. S. A.* **107**, 9944-9949 (2010).
221. B. H. Cumpston *et al.*, Two-photon polymerization initiators for three-dimensional optical data storage and microfabrication. *Nature* **398**, 51-54 (1999).
222. P. Panorchan, J. P. George, D. Wirtz, Probing intercellular interactions between vascular endothelial cadherin pairs at single-molecule resolution and in living cells. *J. Mol. Biol.* **358**, 665-674 (2006).
223. A. M. Esfahani *et al.*, Characterization of the strain-rate-dependent mechanical response of single cell-cell junctions. *Proc. Natl. Acad. Sci. U. S. A.* **118** (2021).
224. S. de Beco, C. Gueudry, F. Amblard, S. Coscoy, Endocytosis is required for E-cadherin redistribution at mature adherens junctions. *Proceedings of the National Academy of Sciences of the United States of America* **106**, 7010-7015 (2009).

225. C. K. Choi *et al.*, Actin and alpha-actinin orchestrate the assembly and maturation of nascent adhesions in a myosin II motor-independent manner. *Nat. Cell Biol.* **10**, 1039-U1036 (2008).
226. Y. S. Chu *et al.*, Force measurements in E-cadherin-mediated cell doublets reveal rapid adhesion strengthened by actin cytoskeleton remodeling through Rac and Cdc42. *J. Cell Biol.* **167**, 1183-1194 (2004).
227. C. Lim, E. Zhou, S. Quek, Mechanical models for living cells—a review. *J. Biomech.* **39**, 195-216 (2006).
228. J. J. Muñoz, S. Albo, Physiology-based model of cell viscoelasticity. *Physical Review E* **88**, 012708 (2013).
229. N. Khalilgharibi *et al.*, Stress relaxation in epithelial monolayers is controlled by the actomyosin cortex. *Nat. Phys.* **15**, 839-847 (2019).
230. J. Hu *et al.*, Size- and speed-dependent mechanical behavior in living mammalian cytoplasm. *Proc. Natl. Acad. Sci. U. S. A.* **114**, 9529-9534 (2017).
231. N. Slomka, C. W. Oomens, A. Gefen, Evaluating the effective shear modulus of the cytoplasm in cultured myoblasts subjected to compression using an inverse finite element method. *Journal of the mechanical behavior of biomedical materials* **4**, 1559-1566 (2011).
232. R. Waugh, M. Tsai, "Shear rate-dependence of leukocyte cytoplasmic viscosity" in Cell Mechanics and Cellular Engineering. (Springer, 1994), pp. 33-44.
233. S. Marion, N. Guillen, J.-C. Bacri, C. Wilhelm, Acto-myosin cytoskeleton dependent viscosity and shear-thinning behavior of the amoeba cytoplasm. *Eur. Biophys. J.* **34**, 262-272 (2005).
234. A. Nikoubashman, M. P. Howard, Equilibrium dynamics and shear rheology of semiflexible polymers in solution. *Macromolecules* **50**, 8279-8289 (2017).
235. P. Panorchan *et al.*, Single-molecule analysis of cadherin-mediated cell-cell adhesion. *J. Cell Sci.* **119**, 66-74 (2006).
236. W. E. Thomas, Understanding the counterintuitive phenomenon of catch bonds. *Current Nanoscience* **3**, 63-77 (2007).
237. J. Friedrichs *et al.*, A practical guide to quantify cell adhesion using single-cell force spectroscopy. *Methods* **60**, 169-178 (2013).
238. S. Vedula *et al.*, Quantifying forces mediated by integral tight junction proteins in cell–cell adhesion. *Experimental mechanics* **49**, 3-9 (2009).
239. H. Tabdili *et al.*, Cadherin-dependent mechanotransduction depends on ligand identity but not affinity. *J. Cell Sci.* **125**, 4362-4371 (2012).
240. C. Franz, P.-H. Puech, Atomic force microscopy: a versatile tool for studying cell morphology, adhesion and mechanics. *Cell. Mol. Bioeng.* **1**, 289-300 (2008).
241. K. E. Cavanaugh, M. F. Staddon, S. Banerjee, M. L. Gardel, Adaptive viscoelasticity of epithelial cell junctions: from models to methods. *Curr. Opin. Genet. Dev.* **63**, 86-94 (2020).
242. L. Casares *et al.*, Hydraulic fracture during epithelial stretching. *Nat. Mater.* **14**, 343-351 (2015).
243. K. V. Iyer, R. Piscitello-Gómez, J. Paijmans, F. Jülicher, S. Eaton, Epithelial viscoelasticity is regulated by mechanosensitive E-cadherin turnover. *Curr. Biol.* **29**, 578-591. e575 (2019).